Parameter Identification of Nonlinear Systems Using Perturbation Methods and Higher-Order Statistics

by

Jimmy Fung

Thesis submitted to the faculty of the

Virginia Polytechnic Institute and State University

in partial fulfillment of the requirements for the degree of

MASTER OF SCIENCE

in

Engineering Mechanics

Approved by

M. R. Hajj, Co-chairman

A. H. Nayfeh, Co-chairman

D. T. Mook

August 3, 1998

Blacksburg, Virginia

Keywords: Nonlinear systems, system identification, parametric identification, higher-order statistics, bispectra, perturbation methods, method of multiple scales.

Parameter Identification of Nonlinear Systems Using Perturbation Methods and Higher-Order Statistics

by

Jimmy Fung

Committee Co-chairmen:

M. R. Hajj and A. H. Nayfeh

Department of Engineering Science and Mechanics

(ABSTRACT)

A parametric identification procedure is proposed that combines the method of multiple scales and higher-order statistics to efficiently and accurately model nonlinear systems. A theoretical background for the method of multiple scales and higher-order statistics is given. Validation of the procedure is performed through applying it to numerical simulations of two nonlinear systems. The results show how the procedure can successfully characterize the system damping and nonlinearities and determine the corresponding parameters. The procedure is then applied to experimental measurements from two structural systems, a cantilevered beam and a three-beam frame. The results show that quadratic damping should be accounted for in both systems. Moreover, for the three-beam frame, the parametric excitation is much more important than the direct excitation. To show the flexibility of the procedure, numerical simulations of ship motion under parametric excitation are used to determine nonlinear parameters govening the relation between pitch, heave, and roll motions. The results show a high level of agreement between the numerical simulation and the mathematical model with the identified parameters.

To my parents

and

my brother

Acknowledgements

My committee has been extremely effective in facilitating my theoretical, analytical, and experimental pursuits at Virginia Tech. First, I would like to thank Dr. Muhammad R. Hajj for his valuable support and guidance in my graduate studies, especially concerning this work and in the experiences I have gained as a research assistant. I would like to thank Dr. Ali H. Nayfeh for being an incredible resource for all aspects of my research and coursework. I also appreciate the time, effort, and advice given by committee member Dr. Dean T. Mook.

I would like to thank those for their assistance concerning my graduate studies, in no particular order. I thank Sean Fahey for helping me in conducting and understanding some of my experimental and theoretical work and for putting up with my inexperience. I am grateful for the long hours I spent at the lab with Shafic Oueini and for all the discussions we have had over coffee. I would like to express my extreme gratitude for Sally Schrader in her assistance with a multitude of tasks and how she somehow manages to always get the job done efficiently and completely.

On a personal note, I thank all of my friends for bringing meaning to my life at Virginia Tech. I am grateful to the many aerospace engineering students who graduated with me and

supported me in my transition to graduate school. I appreciate the kindness of the students at the lab who were quick to welcome me into the research group. Thanks go to Ryan Krauss for his fellowship and advice; Peter Ryan and Troy Jones for helping me relax; and Lanette Roybal, Matt Earl, Ashish Purekar, Jarrod Petersavage, Scott Granger, Dave Reese, and Dave Conkey for helping me define myself.

I thank the Luttrell family for being my family away from home. I appreciate Kay and Jerry Luttrell for their kindness and generosity, and I thank Sarah Luttrell for her clear insight and friendship. Many thanks go to Stephen Irwin for always being there for me. I am most grateful to my parents and my brother Kamy who have always believed in me, supported me, and provided for me. Finally, I am thankful to God and His Grace.

Table of Contents

List of Figures

List of Tables

Chapter 1

Introduction

Accurate modeling of the response of nonlinear systems is important for the reliable prediction and control of that response. In such modeling, one seeks to identify and quantify the relevant physical phenomena that govern the response of a system. Such identification is usually performed in one of two ways: nonparametric or parametric. Nonparametric identification techniques seek to quantify the dynamics of a system without making any assumptions about the dynamics. The identification is then the quantification of the dynamics in some general fashion, such as in a polynomial or Volterra series. Parametric identification techniques, on the other hand, begin with an assumed model of the system dynamics. System identification is then the quantification of the parameters defining the model. Many of these techniques are well documented (Benedittini et al, 1995; Broersen, 1974; Distefano et al, 1975; Masri, 1994; Masri et al, 1979; Udwadia et al, 1981). Many prediction, simulation, and control schemes are designed to observe or modify specific characteristics of a system. Because parametric identification techniques develop models that are based on observed

characteristics of a system, they are directly compatible with these prediction, simulation and control schemes. Thus, in this work, we will focus on a new procedure for parametric identification of damping and nonlinear characteristics of nonlinear systems.

Defining and quantifying a parametric model for nonlinear systems can be a complicated task. Nonlinear behavior in a system is often mistaken for linear behavior. A system may contain several nonlinearities, some of which may not participate in the behavior of interest. Thus, attempting to define a parametric model for only the relevant dynamics of a system is efficient compared to modeling the entire system. Nayfeh (1985) proposed an approach that exploits nonlinear resonances in a system to model its relevant dynamics which, in that case, are the dynamics participating in its nonlinear resonances. A model is assumed based on the possible nonlinearities existing in the system. An approximate solution is then determined for the model using a perturbation technique, such as the method of multiple scales (Nayfeh, 1981; Nayfeh and Mook, 1979). Such a solution models the amplitude and phase modulations of only the modes involved in the resonance of interest. If measured, these modulations can be used to identify the relevant parameters. Moreover, identification of parameters for different resonances may be combined to identify the parameters governing the entire model.

In comparison with amplitude measurements, phase measurements are much more difficult to obtain. Time- and frequency-domain analyses are often employed to quantify the phase characteristics of a system, whereas a number of tools are readily available for the instantaneous quantification of the amplitude characteristics of a system. Nayfeh (1985) proposed modifications to his approach such that phase measurements would not be re-

quired for parameter identification. Hajj et al. (1993) showed how higher-order spectral moments, namely the bispectrum, can be used to obtain phase relations between different frequency components.

The bispectrum has become a popular tool in studying nonlinear systems, and outlines of the uses of higher-order statistics are available (Brillinger, 1994 and 1965). Some examples of its uses are: characterization of sleep states in rats and the onset of seizures in humans, both involving quadratic phase coupling of brain waves, by analyzing electroencephalograms (Ning et al, 1990 and 1991; Shils, 1995); the internal tide off the Southern California coast (Williams, 1985); transition of plane mixing layers (Hajj et al, 1992, 1993, 1997); sheared, thin liquid films (Jurman, 1990); transition of plane wakes (Hajj et al, 1994); confined jets (Henry et al, 1994); transitional flow (Miksad et al, 1982) and (Ritz et al, 1988); turbulence ingestion in propellers (Scharpf, 1993); aeroelastic phenomena (Stearman et al, 1992); orthogonal cutting (Berger et al, 1996); and chaotic systems (Miles et al, 1992; Pezeshki et al, 1990; Pezeshki et al, 1992). Yet, none of these or other applications involves the use of bispectral phase measeurements for use in system parameter identification. We should stress here that higher-order statistics have been employed for system identification where the input is Gaussian (Jin, 1993); the modeling is based on Volterra functions (Collis, 1996; Cho et al, 1994); or the input is not assumed to be known (Giannakis et al, 1989). These system-identification studies, however, are not compatible with the goals of this work because they are based on nonparametric methods. Furthermore, Nayfeh's approach is based on known inputs, which may often be non-Gaussian. There is one study by Hajj, Nayfeh, and Popovic that has used higher-order statistics while adopting Nayfeh's approach to identify

a parametrically excited three-beam frame (Hajj et al, 1995).

It is our intent in this work to develop a parametric identification technique that combines Nayfeh's perturbation-technique approach with the phase detection and measurement capabilities offered by higher-order statistics. This new identification approach will then efficiently provide a model that accurately describes a nonlinear system while lending insight into the dynamics of the system. This technique should then facilitate transition into development of prediction, simulation, and control strategies.

Thesis Outline

This thesis makes a progression from theory to validation and application of the proposed parameter identification technique. In Chapter 2, we discuss the theoretical foundations. A representative single-degree-of-freedom nonlinear system is chosen for the development and use of the technique for the majority of this thesis. A summary is given for Nayfeh's identification approach. A discussion on higher-order spectral moments and their ability to quantify phase information in nonlinear systems is given. The proposed methodology, which combines Nayfeh's approach and higher-order statistics for nonlinear system identification, is then outlined.

Chapter 3 discusses two hypothetical nonlinear systems used to validate the technique. The first system considers a case containing geometric and inertial nonlinearities and linear damping under direct and parametric excitations. The second system considers a similar case with the addition of quadratic damping. The proposed identification technique is ap-

plied to recover the parameters in these systems. New simulations, based on the identified parameters, are then compared to the original simulations for the accuracy and validation of the new technique.

In Chapter 4, the technique is applied to identify the parameters that govern the vibrations in two different structural systems. The first system is a parametrically excited cantilvered beam. The second system is a parametrically excited three-beam frame. For both of these systems, experiments are carried out to observe the excitation and response of the system. Parametric identification is then performed to characterize the damping and identify the parameters in these systems. Numerical simulations, based on the identified parameters, are then compared with the experimental data to measure the accuracy of the identified model in describing the system.

Chapter 5 discusses a modification of the technique and its application to a parametric roll instability of a ship. This instability is described by a multiple-degree-of-freedom model. Again the proposed technique is applied to identify the parameters in this model.

Chapter 2

Theoretical Foundations for Proposed Identification Procedure

In this chapter, the theoretical foundations for the proposed parametric identification technique are given. Our procedure is based on the ideas of exploiting nonlinear resonances (Nayfeh, 1985) and using spectral moments at different orders to obtain amplitude and phase measurements (Hajj et al, 1993, 1997). As we will show in Chapters 3–5, the substitution of these measurements into approximate solutions that exploit the nonlinear resonances will allow us to characterize the governing forces and quanitify their corresponding parameters.

2.1 Nonlinear Systems Under Direct and Parametric Excitation

Nonlinear systems are usually modeled with a set of nonlinear equations that may be algebraic, functional, differential, or integral in nature. Nonlinear system models may also involve combinations of these equations. These models depend on given parameters that, in turn, depend on the physical phenomena under consideration. For instance, in describing free and forced oscillations of single-degree-of-freedom nonlinear systems, two traditional models are usually considered. One model is the Duffing equation (Nayfeh, 1981) and has the form

$$\frac{d^2u}{dt^2} + \delta u + \alpha u^3 = 0 \tag{2.1}$$

where the effects of the restoring forces are modeled with the linear stiffness parameter δ and cubic stiffness parameter α. Another model is Mathieu's equation (Nayfeh, 1981) which has the form

$$\frac{d^2u}{dt^2} + (\delta + 2\epsilon\cos\omega t)u = 0 \tag{2.2}$$

Similar to the Duffing equation, this ordinary-differential equation models harmonically forced oscillations of single-degree-of-freedom systems with a linear restoring force. In this case, the linear stiffness parameter is also δ. The amplitude and frequency of the excitation are represented by 2ϵ and ω, respectively. This excitation is known as a parametric excitation because it appears as a time-varying coefficient of u in the differential equation.

Both the Duffing and Mathieu equations can be expanded to model systems with other

types of excitation, restoring, or nonconservative forces. A more general nonlinear single-degree-of-freedom system is a variant of the Duffing and Mathieu oscillators that includes velocity-dependent damping forces, polynomial and differential-polynomial nonlinearities, and direct and parametric excitations. Such a system is given by

$$\frac{d^2u}{dt^2} + \omega^2 u + 2\mu_1 \frac{du}{dt} + \mu_2 \frac{du}{dt}\left|\frac{du}{dt}\right| + \alpha_2 u^2 + \alpha_3 u^3 + \delta\left(\frac{du}{dt}\right)^2 u = \eta_1 f\cos(\Omega t + \tau_e) + \eta_2 f u \cos(\Omega t + \tau_e) \tag{2.3}$$

In this equation, the linear restoring force is given by $\omega^2 u$, where ω is the linear undamped natural frequency of the system. Quadratic and cubic geometric and inertial restoring forces are modeled by $\alpha_2 u^2$, $\alpha_3 u^3$, and $\delta(du/dt)^2 u$, respectively. These nonlinear restoring forces may model physical phenomena, such as hardening or softening springs and inertial forces. Linear and quadratic damping forces are modeled by $\mu_1 du/dt$ and $\mu_2 du/dt|du/dt|$. The quadratic damping term may model physical phenomena, such as structural or fluid drag in the system. Note that other types of damping forces could have been modeled (Nayfeh and Mook, 1979). The direct and parametric excitations are harmonic and their effects are modeled using the parameters η_1 and η_2, respectively. The forcing parameters f, Ω, and τ_e model the forcing amplitude, frequency, and phase, respectively. While this differential equation does not model all types of quadratic or cubic restoring forces or other types of damping or excitation forces, it sufficiently models systems in many engineering applications. In this chapter, we explain how to obtain an approximate solution of such a system and how its parameters and solution can be obtained from experimental or numerical data.

2.2 Approximate Solutions for Nonlinear Systems With the Method of Multiple Scales

It is usually impossible to obtain an exact solution of a nonlinear system that includes all or even some of the terms of Eq. (3). More often, one has to resort to approximate approaches to predict characteristics, such as stability of the nonlinear system. To do this, a variety of perturbation or dynamical systems methods have been employed. In considering steady-state oscillations of our system, we limit our study to weakly nonlinear systems where the damping, nonlinear restoring, and forcing terms are sufficiently small. This implies that these forces are balanced such that they interact with each other. We then base our solutions on the method of multiple scales. This method is used to study modulated effects to the steady-state of the system rather than global changes in the system.

2.2.1 Scaling and Expansions

To consider the balance between forces in the system, we scale the nonlinearities and excitation sources accordingly. We choose to follow the scaling guidelines outlined by Nayfeh (1981) and Nayfeh and Mook (1979). This results in

$$\frac{d^2u}{dt^2} + \omega^2 u + 2\epsilon^2\mu_1\frac{du}{dt} + \epsilon^2\mu_2\frac{du}{dt}\left|\frac{du}{dt}\right| + \epsilon\alpha_2u^2 + \epsilon^2\alpha_3u^3 + \epsilon^2\delta\left(\frac{du}{dt}\right)^2 u = \epsilon\eta_1 f\cos(\Omega t + \tau_e) + \epsilon^2\eta_2 f u\cos(\Omega t + \tau_e) \quad (2.4)$$

Here, we consider the case $\Omega \approx 2\omega$. The scaling parameter ϵ represents the level to which the nonlinearity has an effect on the system. In this system, we scale the direct excitation

to the same level as the quadratic restoring force. The parametric excitation is scaled to a lower level along with damping, cubic geometric and inertial nonlinearities. In considering the balance among these forces, we scale the quadratic nonlinearities and direct excitation so that they appear at lower order.

An approximate solution for the response of the system, given in Eq. (2.4), can be obtained by using the method of multiple scales (Nayfeh, 1981; Nayfeh and Mook, 1979). To differentiate between slow and fast-varying effects on the system, we use the scaling parameter ϵ and replace the time t with independent variables T_n, such that

$$T_n = \epsilon^n t \qquad\qquad n = 0,\, 1,\, 2,\, \cdots \tag{2.5}$$

In this sense, T_0 represents a fast time scale and T_1, T_2, T_3, $\cdots$ represent slow time scales. Our ordinary-differential equation now becomes a partial-differential equation, with u being a function of the new time scales. The first- and second-derivative operators with respect to t are then given by

$$\frac{d}{dt} = \frac{dT_0}{dt}\frac{\partial}{\partial T_0} + \frac{dT_1}{dt}\frac{\partial}{\partial T_1} + \frac{dT_2}{dt}\frac{\partial}{\partial T_2} + \cdots = D_0 + \epsilon D_1 + \epsilon^2 D_2 + \cdots \tag{2.6}$$

$$\frac{d^2}{dt^2} = (D_0 + \epsilon D_1 + \epsilon^2 D_2 + \cdots)^2 = D_0^2 + \epsilon^2 D_1^2 + 2\epsilon D_0 D_1 + 2\epsilon D_0 D_2 + \cdots \tag{2.7}$$

The expression D_j^i refers to the i-th partial derivative with respect to T_j. Moreover, we expand the generalized coordinate u using the scaling parameter, ϵ, as

$$u(t;\epsilon) = u_0(T_0, T_1, T_2) + \epsilon u_1(T_0, T_1, T_2) + \epsilon^2 u_2(T_0, T_1, T_2) + \cdots \tag{2.8}$$

In this manner, we are assuming a series solution for u of Eq. (2.4) based on functions that have scaled levels of influence on the total response of the system. The primary portion

of the response is found in u_0. The perturbation u_1 serves as a small adjustment to the response, the perturbation u_2 serves as an even smaller adjustment to the response, and so on. Substituting Eqs. (2.6)–(2.8) into Eq. (2.4) and considering terms up to order ϵ^2, we obtain

$$\begin{aligned}(D_0^2 + \epsilon D_1^2 + 2\epsilon D_0 D_1 + 2\epsilon D_0 D_2)(u_0 + \epsilon u_1 + \epsilon^2 u_2) + \omega^2(u_0 + \epsilon u_1 + \epsilon^2 u_2) \\ + 2\epsilon^2 \mu_1 D_0 u_0 + \epsilon^2 \mu_2 D_0 u_0 |D_0 u_0| + \epsilon \alpha_2 (u_0 + \epsilon u_1)^2 + \epsilon^2 \alpha_3 u_0^3 + \epsilon^2 \delta u_0 (D_0 u_0)^2 \\ = \epsilon \eta_1 f \cos(2\omega T_0 + \sigma T_2 + \tau_e) + \epsilon^2 \eta_2 f u_0 \cos(\Omega T_0 + \tau_e) \end{aligned} \tag{2.9}$$

This partial-differential equation can be simplified and separated into coefficients of like powers of ϵ. Again, considering terms up to order ϵ^2, we obtain

$$O(\epsilon^0) : D_0^2 u_0 + \omega^2 u_0 = 0 \tag{2.10}$$

$$O(\epsilon^1) : D_0^2 u_1 + \omega^2 u_1 = -2D_0 D_1 u_0 - \alpha_2 u_0^2 + \eta_1 f \cos(\Omega T_0 + \tau_e) \tag{2.11}$$

$$\begin{aligned} O(\epsilon^2) : D_0^2 u_2 + \omega^2 u_2 = &-D_1^2 u_0 - 2D_0 D_1 u_1 - 2D_0 D_2 u_0 - 2\mu_1 D_0 u_0 \\ &-\mu_2 D_0 u_0 |D_0 u_0| - 2\alpha_2 u_0 u_1 - \alpha_3 u_0^3 - \delta u_0 (D_0 u_0)^2 \\ &+\eta_2 f u_0 \cos(\Omega T_0 + \tau_e) \end{aligned} \tag{2.12}$$

where $O(\epsilon^i)$ denotes the power of ϵ under consideration.

2.2.2 Solvability Conditions Over T_1 and T_2 and Uniform Second-Order Expansion for $u(t)$

The solution of the system of equations given by Eqs. (2.10)–(2.12) is obtained by substituting the solutions of the lower-order equations in ϵ into the higher-order equations in ϵ. First,

the solution for u_0 is obtained from Eq. (2.10) and then substituted into Eq. (2.11). The solution for u_1 is then obtained from Eq. (2.11) and finally substituted into Eq. (2.12). This yields an approximate solution of the system that is accurate to second order.

Following this procedure, we express the solution of Eq. (2.10) in the form

$$\begin{aligned} u_0 &= \frac{1}{2}a(T_1, T_2)e^{i[\beta(T_1,T_2)+\omega T_0]} + \text{cc} \\ &= A(T_1, T_2)e^{i\omega T_0} + \text{cc} \end{aligned} \tag{2.13}$$

where $A = \frac{1}{2}ae^{i\beta}$, A, a, and β are functions of T_1 and T_2, and cc represents the complex conjugate of the preceding terms. In this sense a and β represent the amplitude and phase of the response.

Substituting the solution for u_0 from Eq. (2.13) into each term in Eq. (2.11), we obtain

$$\begin{aligned} -2D_0D_1u_0 &= -2i\omega A'e^{i\omega T_0} + \text{cc} \\ -\alpha_2 u_0^2 &= -\alpha_2 A^2 e^{2i\omega T_0} - \alpha_2 A\overline{A} + \text{cc} \\ \eta_1 f\cos(2\omega T_0 + \sigma T_2 + \tau_e) &= \frac{1}{2}\eta_1 f e^{i(\Omega T_0+\tau_e)} + \text{cc} \end{aligned} \tag{2.14}$$

Then, we rewrite Eq. (2.11) as

$$D_0^2u_1 + \omega^2 u_1 = -2i\omega A'e^{i\omega T_0} - \alpha_2 A^2 e^{2i\omega T_0} - \alpha_2 A\overline{A} + \frac{1}{2}\eta_1 f e^{i(\Omega T_0+\tau_e)} + \text{cc} \tag{2.15}$$

As discussed earlier, we consider the case when the excitation frequency Ω is near twice the natural frequency ω of the system. This relationship is expressed as

$$\Omega = 2\omega + \epsilon^2\sigma \tag{2.16}$$

where σ is a frequency-detuning parameter, which is scaled at ϵ^2 to indicate the extremely small difference between the excitation frequency and twice the natural frequency of the

system. To ensure a uniform expansion for u, we need to prevent the occurence of secular terms, or terms which cause series divergence. In doing so, we arrive at a compatibility or solvability condition to obtain a uniform solution. This condition requires setting the coefficients of $e^{\pm i\omega T_0}$ in Eq. (2.15) equal to zero; that is,

$$-2i\omega A' = 0 \tag{2.17}$$

Note that satisfying Eq. (2.17) automatically satisfies its complex conjugate. It follows from Eq. (2.17) that $\partial A/\partial(T_1) = 0$ or $A = A(T_2)$; that is, a and β are functions of only the fastest scale T_2. From Eqs. (2.15) and (2.17) and ignoring the homogeneous solution, we obtain a particular solution for u_1 as

$$\begin{aligned} u_1 &= \frac{1}{3\omega^2}\alpha_2 A^2 e^{2i\omega T_0} + \frac{\alpha_2}{\omega^2}A\overline{A} - \frac{\eta_1 f}{2[\omega^2 - (2\omega + \epsilon^2\sigma)^2]}e^{i(2\omega T_0 + \sigma T_2 + \tau_e)} + \text{cc} \\ &\approx \frac{1}{3\omega^2}\alpha_2 A^2 e^{2i\omega T_0} - \frac{\alpha_2}{\omega^2}A\overline{A} - \frac{1}{6\omega^2}\eta_1 f e^{i(2\omega T_0 + \sigma T_2 + \tau_e)} + \text{cc} \end{aligned} \tag{2.18}$$

The approximation in Eq. (2.18) is made considering the greater importance of ωT_0 in comparison to σT_2.

Substituting the solutions for u_0 and u_1 into each of the right-hand side terms of Eq. (2.12) yields the following:

$$-D_1^2 u_0 = 0 \tag{2.19}$$

$$-2D_0 D_1 u_1 = 0 \tag{2.20}$$

$$-2D_0 D_2 u_0 = -2i\omega A' e^{i\omega T_0} + \text{cc} \tag{2.21}$$

$$-2\mu_1 D_0 u_0 = -2i\omega\mu_1 A e^{i\omega T_0} + \text{cc} \tag{2.22}$$

$$-\mu_2 D_0 u_0 |D_0 u_0| = -\mu_2 \sum_{n=-\infty}^{\infty} g_n e^{in\omega T_0}$$

$$= -\mu_2 g_1 e^{i\omega T_0} + \text{NST} + \text{cc} \tag{2.23}$$

where

$$g_n = -\frac{1}{2\pi}\int_0^{2\pi}(i\omega A e^{i\omega T_0} - i\omega\overline{A}e^{-i\omega T_0})|i\omega A e^{i\omega T_0}$$
$$-i\omega\overline{A}e^{-i\omega T_0}|e^{-in\omega T_0}d(\omega T_0) \tag{2.24}$$

$$-2\alpha_2 u_0 u_1 = -2\alpha_2(Ae^{i\omega T_0} + \overline{A}e^{-i\omega T_0})[\frac{1}{3\omega^2}\alpha_2 A^2 e^{2i\omega T_0}$$
$$-\frac{\alpha_2}{\omega^2}A\overline{A} - \frac{1}{6\omega^2}\eta_1 f e^{i(2\omega T_0+\sigma T_2+\tau_e)}]$$
$$= [-\frac{2}{3}\frac{\alpha_2^2}{\omega^2}A^2\overline{A} + 4\alpha_2^2 A^2\overline{A} + \frac{1}{3}\eta_1 f\overline{A}e^{i(\sigma T_2+\tau_e}]e^{i\omega T_0}$$
$$+\text{NST} + \text{cc} \tag{2.25}$$

$$-\alpha_3 u_0^3 = -3\alpha_3 A^2\overline{A}e^{i\omega T_0} + \text{NST} + \text{cc} \tag{2.26}$$

$$-\delta u_0(D_0 u_0)^2 = \alpha_4(Ae^{i\omega T_0} + \overline{A}e^{-i\omega T_0})(i\omega A e^{i\omega T_0} - i\omega\overline{A}e^{-i\omega T_0})^2$$
$$= -\delta(-\omega^2 A^2\overline{A} + 2\omega + 0A^2\overline{A})e^{i\omega T_0} + \text{NST} + \text{cc} \tag{2.27}$$

$$\eta_2 f u_0\cos(2\omega T_0 + \sigma T_2 + \tau_e) = \frac{1}{2}\eta_2 f(Ae^{i\omega T_0} + \overline{A}e^{-i\omega T_0})[e^{i(2\omega T_0+\sigma T_2+\tau_e)}$$
$$+e^{-i(2\omega T_0+\sigma T_2+\tau_e)}]$$
$$= \frac{1}{2}\eta_2 f\overline{A}e^{i(\omega T_0+\sigma T_2+\tau_e)} + \text{NST} + \text{cc} \tag{2.28}$$

In the above equations, NST denotes terms that do not produce secular terms. By substitution into Eq. (2.12), we obtain

$$D_0^2 u_2 + \omega_2 u_2 = [-2i\omega A' - 2i\omega\mu_1 A - \mu_2 g_1 + (\frac{10}{3}\alpha_2^2 - 3\alpha_3 - \delta\omega^2)A^2\overline{A}$$
$$+(\frac{1}{3}\eta_1 + \frac{1}{2})f\overline{A}e^{i(\sigma T_2+\tau_e)}]e^{i\omega T_0} + \text{NST} + \text{cc} \tag{2.29}$$

Again, to prevent divergence and obtain a uniform solution, we eliminate the secular terms

by setting the coefficients of $e^{\pm i\omega T_0}$ equal to zero; that is,

$$-2i\omega A' - 2i\omega\mu_1 A - \mu_2 g_1 + (\frac{10}{3}\alpha_2^2 - 3\alpha_3 - \delta\omega^2)A^2\overline{A} + (\frac{1}{3}\eta_1 + \frac{1}{2})f\overline{A}e^{i(\sigma T_2 + \tau_e)} = 0 \tag{2.30}$$

Note that satisfying Eq. (2.30) automatically satisfies its complex conjuate.

By substituting for A and $\overline{A}$ from Eq. (2.13) into Eq. (2.30), we obtain

$$-i\omega(a' + ai\beta') - i\omega\mu_1 a - \frac{4}{3\pi}i\mu_2\omega^2 a^2 + \alpha_e a^3 + \eta_e f a e^{i\gamma} = 0 \tag{2.31}$$

where

$$\alpha_e = \frac{5}{12}\alpha_2^2 - \frac{3}{8}\alpha_3 - \frac{1}{8}\delta\omega^2 \tag{2.32}$$

$$\eta_e = \frac{1}{6}\frac{\alpha_2\eta_1}{\omega^2} + \frac{1}{4}\eta_2 \tag{2.33}$$

$$\gamma = \sigma T_2 + \tau_e - 2\beta \tag{2.34}$$

The parameters α_e and η_e in Eqs. (2.32)–(2.33) represent effective nonlinear restoring and forcing parameters, respectively. Separating Eq. (2.31) into imaginary and real parts and eliminating β using Eq. (2.34), we have

$$-\omega a' - \omega\mu_1 a - \frac{4}{3\pi}\mu_2\omega^2 a^2 + \eta_e f a \sin\gamma = 0 \tag{2.35}$$

$$\frac{1}{2}a\omega(\sigma - \gamma') + \alpha_e a^3 + \eta_e f a\cos\gamma = 0 \tag{2.36}$$

These equations can be rewritten as

$$\omega a' = -\omega\mu_1 a - \frac{4}{3\pi}\mu_2\omega^2 a^2 + \eta_e f a\sin\gamma \tag{2.37}$$

$$\frac{1}{2}\omega a\gamma' = \frac{1}{2}a\omega\sigma + \alpha_e a^3 + \eta_e f a\cos\gamma \tag{2.38}$$

The relationships described in Eqs. (2.37) and (2.38) represent the slow modulation of the amplitude and phase of the response

Combining Eqs. (2.8), (2.13), and (2.18) and substituting the expressions for A and $\overline{A}$ from Eq. (2.13) and β from Eq. (2.34), we arrive at the following approximate solution for $u(t)$:

$$u = \frac{1}{2}ae^{\frac{1}{2}i(\Omega t+\tau_e-\gamma)} + \epsilon[\frac{\alpha_2}{12\omega^2}a^2e^{i(\Omega t+\tau_e-\gamma)} - \frac{\alpha_2}{4\omega^2}a^2 - \frac{\eta_1}{6\omega^2}fe^{i(\Omega t+\tau_e)}] + \text{cc} \tag{2.39}$$

The relationships described in Eqs. (2.37)–(2.39) form a uniform second-order solution of the differential equation for the case $\Omega \approx 2\omega$.

Nayfeh (1985) proposed a series of experiments that exploit nonlinear resonances and approximate solutions for the identification of the damping and nonlinear parameters of nonlinear systems. In that work, values of the excitation and response amplitudes are substituted into Eqs. (2.37)–(2.38) to obtain the parameters. Fahey and Nayfeh (1998) applied that methodology to determine the parameters governing a system that models the nonlinear response of a three-beam frame. In this work we extend the methodology proposed by Nayfeh (1985) and use measured values for the amplitudes as well as the phase quantity γ to determine the parameters. The results will show that, by determining this phase quantity, not only can we estimate the parameters, but we can also characterize them.

2.3 Amplitude and Phase Measurements Using Spectral Moments

One of the most useful tools in time-series analysis has been the power spectrum. In estimating the power spectrum, one considers the time series as a superposition of frequency components. The power spectrum then gives the distribution of power among these components. Such estimates have been the cornerstone in the development and analysis of many physical phenomena. Yet, because the power spectrum suppresses phase relationships between frequency components, it can only be used to investigate linear mechanisms. To obtain information regarding nonlinearities in discrete-time deterministic and stochastic processes, one needs estimates of higher-order spectra (Hajj et al, 1997). One particular higher-order spectral quantity that has become widely used is the bispectrum. The bispectrum has been applied in studying deviations from Gaussianity of a process and quadratic phase coupling (see Chapter 1). In this section, spectral moments are defined and their properties are discussed.

2.3.1 Power Spectra and Linear Coherence

For a continuous process $x(t)$, the Fourier transform $X(f)$ is defined as

$$X(f) = \int_{-\infty}^{\infty} x(t)e^{-2\pi ift}dt \tag{2.40}$$

For the k-th ensemble of a discrete process $x_T(nt_s)$ of length T, where the process takes on values at the time nt_s for the time step t_s, where t_s is the sampling time and $n =$

$0, 1, 2, \ldots, N-1$, the Fourier transform $X_T^{(k)}[l]$ is

$$X_T^{(k)}[l] = \frac{1}{N} \sum_{n=0}^{N-1} x_T^{(k)}(nt_s) e^{-2\pi i l \frac{n}{N}} \tag{2.41}$$

where the frequencies take on values every $l\Delta f = 1/T$ with a frequency step of Δf and $l = 0, 1, 2, \ldots, N-1$. In general, the Fourier transform of a process is a complex-valued function. For a real-valued time series, this function has symmetry over frequency in that

$$X^{*(k)}(l) = X^{(k)}(-l) \tag{2.42}$$

This symmetry relationship allows for the reduction in the domain over which the Fourier transform needs to be calculated.

The power spectral-density function, or power spectrum, is commonly used in the frequency-domain analysis of a random process. For the k-th ensemble of a discrete, stationary, real-valued zero-mean process $x(t_s)$, the power spectral-density function $P_{xx}(l)$ is given by

$$\begin{aligned} \hat{P}_{xx}[l] &= \frac{2}{M} \sum_{k=1}^{M} \left| X_T^{(k)}[l] \right|^2 && l = 1, 2, \ldots, \frac{N}{2} - 1 \\ &= \frac{1}{M} \sum_{k=1}^{M} \left| X_T^{(k)}[l] \right|^2 && l = 0 \quad \text{or} \quad \frac{N}{2} \end{aligned} \tag{2.43}$$

where M is the total number of ensembles. There are two important properties of the power spectrum First, $\hat{P}_{xx}[l]$ is only an estimate of the power spectrum. Second, the value of the power spectrum at a certain frequency is equal to the square of the rms amplitude of the corresponding frequency component in the time-varying process. Note that the factor of two is included because l and the power spectral-density function are defined for positive frequency values only. Figure 2.1 shows a time history for a time series, which consists of

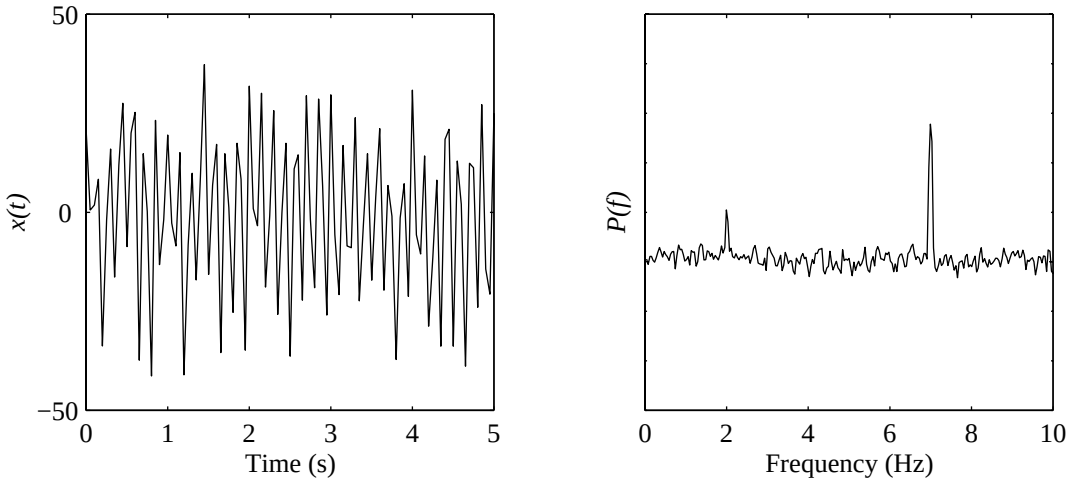

Figure 2.1: Sample time history of $x(t)$ and its corresponding power spectrum.

the frequency components at 2 Hz and 7 Hz, and its corresponding power spectrum. It is clear how the power spectrum is a useful tool for observing the frequency composition of a signal. One thing to keep in mind is that the power spectrum is a real-valued function. Thus, it contains only magnitude information and suppresses all phase information about the frequency components.

Similar to the definition of the power spectrum, one can define the cross-power spectrum between two time series $x(t)$ and $y(t)$ by

$$\begin{aligned} \hat{P}_{yx}^{(k)}[l] &= \frac{2}{M}\sum_{k=1}^{M}\left|X_T^{(k)}[l]Y_T^{*(k)}[l]\right| && l = 1, 2, \ldots, \frac{N}{2} - 1 \\ &= \frac{1}{M}\sum_{k=1}^{M}\left|X_T^{(k)}[l]Y_T^{*(k)}[l]\right| && l = 0 \quad \text{or} \quad \frac{N}{2} \end{aligned} \tag{2.44}$$

Note that the cross-power spectrum is a complex-valued function. The phase of the cross-power spectrum quantifies the phase difference between the same frequency components in $x(t)$ and $y(t)$. If, as shown schematically in Fig. 2.2, the phase of the cross-power spectrum

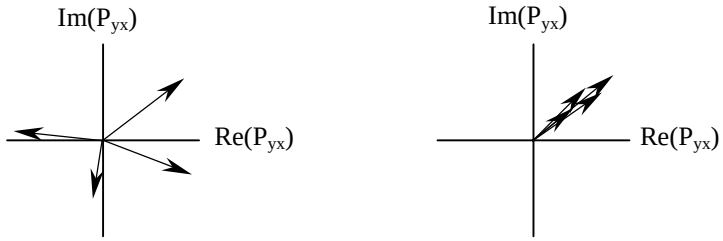

Figure 2.2: Cross-power spectrum between $x(t)$ and $y(t)$ at a certain frequency, measured for four ensembles. Frequency components between $x(t)$ and $y(t)$ are (a) not phase related; (b) phase related.

vector has a small variance over many time records, or ensembles, the magnitude of the cross-power spectrum at that frequency is relatively large and the phase of the cross-power spectrum is a relatively accurate estimate of the phase difference between the appropriate frequency components in $x(t)$ and $y(t)$. On the other hand, if the vector varies randomly over many records, the magnitude of the cross-power spectrum is relatively low and the phase estimate does not carry much meaning.

The linear coherence $\gamma^2_{yx}(l)$ which is defined as

$$\gamma^2_{yx}(l) = \frac{|P_{yx}(l)|^2}{P_{xx}(l)P_{yy}(l)} \tag{2.45}$$

is a normalization of the cross-power spectrum. It can be shown by Schwartz inequality that the linear coherence $\gamma^2_{yx}(l)$ is bounded by zero and one. Thus, if the frequency components of $x(t)$ and $y(t)$ at frequency f are not linearly coupled in phase, the linear coherence will be equal to zero. If the frequency components of $x(t)$ and $y(t)$ at frequency f are linearly coupled, the linear coherence will be equal to one. If the linear coupling between the frequency components of $x(t)$ and $y(t)$ at frequency f is partial, the linear coherence will

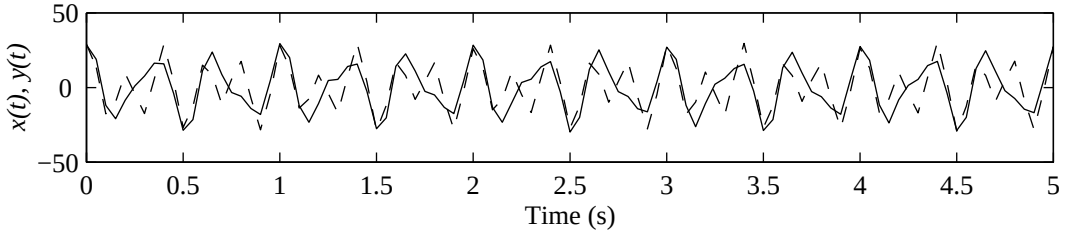

Figure 2.3: Time histories for the signals $x(t)$ (solid) and $y(t)$ (dotted) defined in Eqs. (2.46)–(2.47). Here, $f_a = 3$ Hz and $f_b = 5$ Hz.

have a value between zero and one. To demonstrate this argument, we consider two signals $x(t)$ and $y(t)$, which are constructed from

$$x(t) = a\cos(\omega_a t + \theta_a) + b\cos(\omega_b t + \theta_b) + n_1(t) \tag{2.46}$$

$$y(t) = c\cos(\omega_a t + \theta_c) + d\cos(\omega_b t + \theta_d) + n_2(t) \tag{2.47}$$

where

$$\theta_a, \theta_b, \quad \text{and} \quad \theta_c \qquad \text{random} \tag{2.48}$$

and

$$\theta_d = \theta_b + \alpha \tag{2.49}$$

Low-level Gaussian noise $n_i(t)$ is added to each signal. The phase relationships in Eqs. (2.48)–(2.49) indicate that θ_a and θ_c are chosen from two independent random sets, while θ_b, which is chosen from a random set, always differs from θ_d by α. Figures 2.3–2.5 shows time histories of the two signals, their power spectra, and their linear coherence. The power spectra shown in Fig. 2.4 shows that both signals $x(t)$ and $y(t)$ are composed of two frequency components at frequencies $f_a = \omega_a/2\pi$ and $f_b = \omega_b/2\pi$. However, no information on the phase relationship can be obtained. In contrast, the phase relationships are captured in the linear coherence

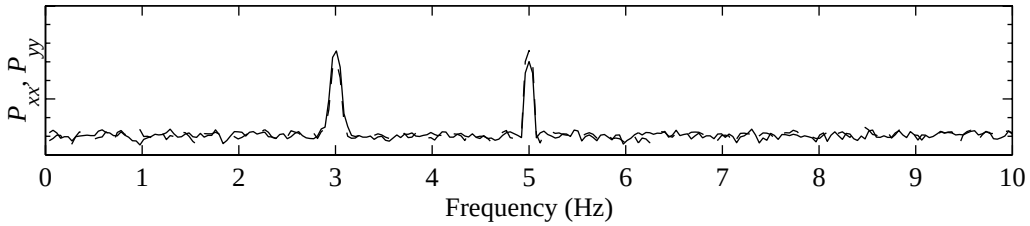

Figure 2.4: Power spectra for the signals $x(t)$ (solid) and $y(t)$ (dotted) defined in Eqs. (2.46)–(2.47). Here, $f_a = 3$ Hz and $f_b = 5$ Hz.

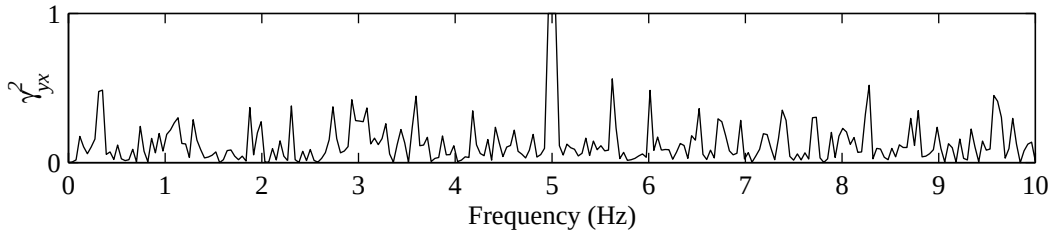

Figure 2.5: Linear coherence for the signals $x(t)$ and $y(t)$ defined in Eqs. (2.46)–(2.47). Here, $f_a = 3$ Hz and $f_b = 5$ Hz.

between the two signals (Fig. 2.5) where the linear coherence is near zero at f_a and near one at f_b. The linear coherence function then confirms and quantifies the linear coupling between the two signals at ω_b.

2.3.2 Higher-Order Spectral Moments

As discussed in the previous section, the power spectrum allows for quantification of the frequency content of a signal, and the linear coherence allows for the detection of linear coupling and quantification of phase differences between the same frequency component in two signals. In order to detect nonlinear coupling and measure the phase relationship among different frequency components, one needs to use higher-order spectral moments, such as the

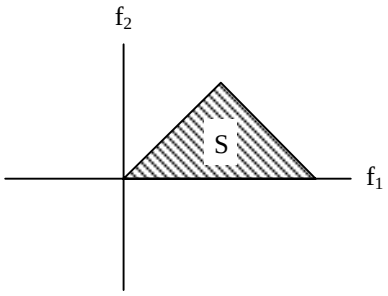

Figure 2.6: Smallest unique domain S of the auto-bispectral-density function.

auto- and cross-bispectrum (Kim and Powers, 1979; Hajj et al, 1997).

For a discrete, stationary, real-valued, zero-mean process $x_T(t_s)$, the auto-bispectral-density function is estimated as

$$\hat{B}_{xxx}[l_1, l_2] = \frac{1}{M} \sum_{k=1}^{M} \left| X_T^{(k)}[l_1 + l_2] X_T^{*(k)}[l_1] X_T^{*(k)}[l_2] \right|^2 \tag{2.50}$$

with $X_T^{(k)}[l]$ defined previously. The bispectrum of a signal is a two-dimensional function of frequency. For real-valued signals, one could use the symmetry relationship from Eq. (2.42), to show that the auto-bispectrum needs to be defined only over a domain such as the one shown in Fig. 2.6. Because this domain only includes positive values of f_i, and because the auto-bispectrum is calculated for frequency components at f_1, f_2, and $f_1 + f_2$, this domain is defined as the sum region of the bispectrum. Because the bispectrum is calculated using three Fourier transforms, the bispectrum will generally be complex-valued.

In averaging over many ensembles, the magnitude of the auto-bispectrum will be determined by the presence of a phase relationship among sets of the frequency components at f_1, f_2, and $f_1 + f_2$. If there is a random phase relationship among these three components, the auto-bispectrum will average to a very small value. Should there be any phase relationship

among these frequency components, the corresponding auto-bispectral value will have a large magnitude. The auto-bispectrum is able to detect nonlinear phase coupling among different frequency components of a signal because of this phase-preserving effect. Furthermore, the auto-bispectrum detects quadratic phase coupling, since this function detects the effects of two components and their quadratic relation to a third component. Similarly to the linear coherence function, the auto-bispectrum can be normalized to quantify the level of quadratic coupling in a signal. The normalized quantity is called the auto-bicoherence and is defined as

$$b^2_{xxx}(l_1, l_2) = \frac{|B_{xxx}(l_1, l_2)|^2}{E[|X(l_1)X(l_2)|^2]E[|X(l_1 + l_2)|^2]} \tag{2.51}$$

where $E[\ldots]$ denotes the expected value. If there is no phase relationship among the frequency components at f_1, f_2, and $f_1 + f_2$, the corresponding value of the auto-bicoherence will be near zero. If there is a phase relationship among the frequency components at f_1, f_2, and $f_1 + f_2$, then the corresponding value of the auto-bicoherence will be near unity. Values of the auto-bicoherence between zero and one indicate partial quadratic coupling.

To demonstrate these relations, we consider a similar example to that of Kim and Powers (1979) and consider a signal $x(t)$ defined by

$$\begin{aligned} x(t) = {} & a\cos(\omega_1 t + \theta_1) + b\cos(\omega_2 t + \theta_2) + c\cos[(\omega_1 + \omega_2)t + \theta_3] \\ & + 2c\cos(\omega_1 t + \theta_1 + \alpha_1)\cos(\omega_2 t + \theta_2 + \alpha_2) + n(t) \end{aligned} \tag{2.52}$$

This signal contains frequency components at $\omega_1 = 2\pi f_1$, $\omega_2 = 2\pi f_2$, $\omega_1 + \omega_2 = 2\pi(f_1 + f_2)$, and $\omega_1 - \omega_2 = 2\pi(f_1 - f_2)$. The sum component has two sources: one is independent (the third term on the right-hand side of Eq. (2.52) and the other results from the fourth term

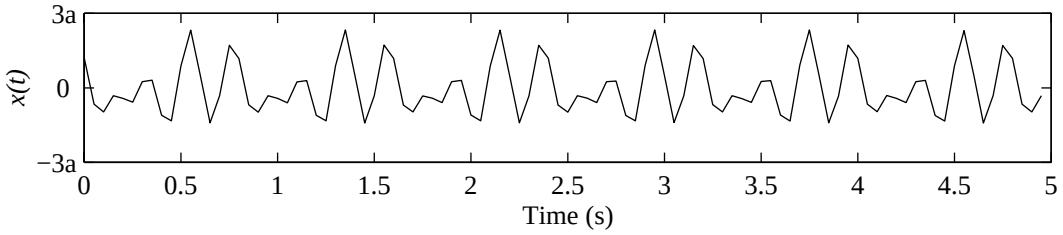

Figure 2.7: Time history of $x(t)$ as defined in Eq. (2.52).

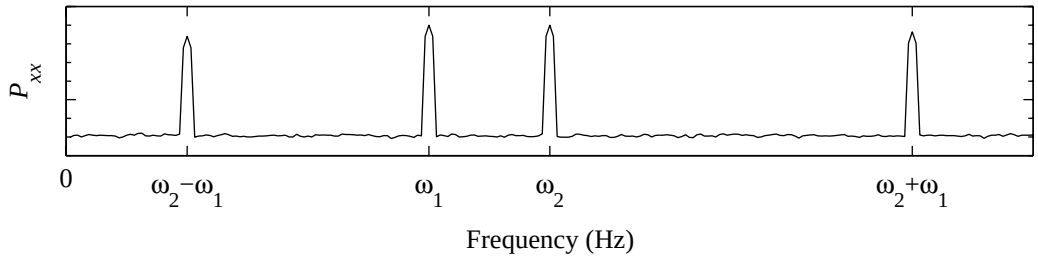

Figure 2.8: Power spectrum of $x(t)$ as defined in Eq. (2.52).

on the right-hand side of Eq. (2.52) . Note also that the contributions of these sources are equal. The difference component results only from the fourth term on the right-hand side of Eq. (2.52) . The computed time history, power spectrum, and auto-bicoherence for $x(t)$ are shown in Figs. 2.7–2.9. As shown in Fig. 2.8, the power spectrum serves as a tool for identifying the frequency content of a signal. However, the power spectrum is not capable of detecting the quadratic nature of the frequency components and their phase coupling with the components of the signal.

The auto-bicoherence of $x(t)$, as shown in Fig. 2.9, contains a high peak of 0.99 at (ω_1, $\omega_2 - \omega_1$). This peak indicates almost total phase coupling among the frequency components at $\omega_2 - \omega_1$, ω_1, and $(\omega_2 - \omega_1) + \omega_1 = \omega_2$. This high level of coupling indicates that the

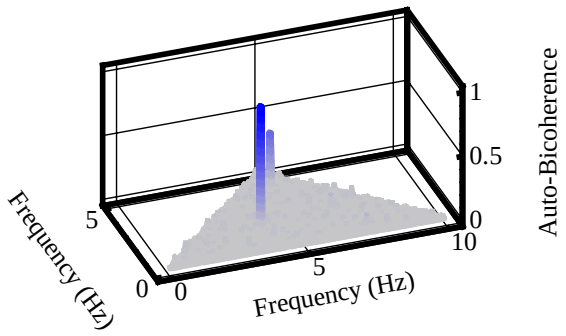

Figure 2.9: Auto-bicoherence of $x(t)$ as defined in Eq. (2.52). Here, $f_1 = 3.75$ Hz and $f_2 = 5$ Hz.

component at $\omega_2 - \omega_1$ is entirely generated from the difference portion of the signal which is the case. Furthermore, the components at ω_1 and ω_2 are related in phase to the difference component at $(\omega_2 - \omega_1)$. From observing Eq. (2.52), this phase relationship should be

$$\theta_2 - \theta_1 - [(\theta_2 + \alpha_2) - (\theta_1 + \alpha_1)] = \alpha_1 - \alpha_2 \tag{2.53}$$

Since the auto-bispectrum preserves phase information in a signal with quadratically phase-coupled components, the phase of the auto-bispectrum at $(\omega_1,\ \omega_2 - \omega_1)$ equals the phase of the component at ω_2 minus the phase of the component at ω_1 minus the phase of the component at $\omega_2 - \omega_1$, which equals $\alpha_1 - \alpha_2$, as predicted in Eq. (2.53).

The auto-bicoherence of $x(t)$, as shown in Fig. 2.9, also contains a peak of 0.47 at $(\omega_2,\ \omega_1)$. This indicates partial coupling among the components at ω_1 and ω_2 and the sum portion of the signal at $\omega_1 + \omega_2$. The value of 0.47, which is near 0.5, indicates an equal contribution from the two sources, which is the case. Any variance away from these ideal peak values is attributed to imperfections in the random number generator used to obtain the phases. The

phase relationship among the components and the sum portion of the signal is

$$[(\theta_2 + \alpha_2) + (\theta_1 + \alpha_1)] - \theta_2 - \theta_1 = \alpha_1 + \alpha_2 \tag{2.54}$$

Because of the independent component at $\omega_1 + \omega_2$, the phase of the corresponding auto-bispectrum will not be equal to the phase predicted by Eq. (2.54).

As demonstrated in this example, the auto-bispectrum and auto-bicoherence functions are useful tools for detecting and quantifying quadratic coupling and corresponding phase relationships in a signal.

As discussed in the previous section, the auto-bispectrum and auto-bicoherence allow for detection of nonlinear coupling and quantification of relations among frequency components in a signal. For systems where multiple signals are considered, these objectives can be achieved by using the cross-spectral moments (Hajj et al, 1997). For two signals $x(t)$ and $y(t)$, their cross-bispectral density function is estimated as

$$\hat{B}_{yxx}[l_1, l_2] = \frac{1}{M} \sum_{k=1}^{M} \left| Y_T^{(k)}[l_1 + l_2] X_T^{*(k)}[l_1] X_T^{*(k)}[l_2] \right|^2 \tag{2.55}$$

with $X_T^{(k)}[l]$ defined previously. The cross-bispectrum provides a measure of the nonlinear relation among frequency components at f_1 and f_2 in $x(t)$ and their sum frequency component $f_1 + f_2$ in $y(t)$. Like the auto-bispectrum, the cross-bispectrum of signals $x(t)$ and $y(t)$ is a two-dimensional function in frequency. For real-valued signals, the symmetry relationships from Eq. (2.42) show that only a part of the two-dimensional frequency domain needs to be considered to determine the cross-bispectrum among all frequencies between two signals (Fig. 2.10). Because this domain includes positive and negative values for f_2, this domain is divided into a sum region S and a difference region D. The sum region contains information

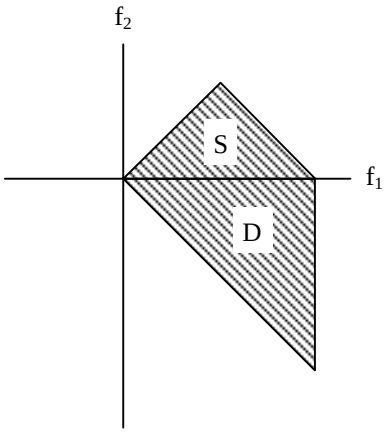

Figure 2.10: Smallest unique domain S and D of the cross-bispectral density function.

about nonlinear coupling among components at f_1 and f_2 in $x(t)$ and their sum $f_1 + f_2$ in $y(t)$. The difference region contains information for phase relationships among components at f_1 and $-f_2$ in $x(t)$ and their difference $f_1 - f_2$ in $y(t)$. Future reference to these frequency relationships will be in the form of f_1, f_2, and $f_1 + f_2$, rather than references to both sum and difference relationships. The characteristics of the cross-bispectrum are otherwise similar to those of the auto-bispectrum.

Because the cross-bispectrum is calculated using three Fourier transforms, the cross-bispectrum will also be, in general, complex-valued. In averaging over many ensembles, the magnitude of the cross-bispectrum will also be determined by the presence of a phase relationship among sets of the frequency components at f_1, f_2, and $f_1 + f_2$. If there is a random phase relationship among the three components, the cross-bispectrum will average to a very small value. Should there be any phase relationship among these frequency components, the corresponding cross-bispectral value will have a large magnitude. The cross-bispectrum is

then able to detect nonlinear phase coupling among different frequency components in two signals because of its phase-preserving effect. Similarly to the auto-bicoherence function, one can define a normalized cross-bispectrum to quantify the level of quadratic coupling in two signals. This normalized value is called the cross-bicoherence and is defined as

$$b^2_{yxx}(f_1, f_2) = \frac{|B_{yxx}(f_1, f_2)|^2}{E[|X(f_1)X(f_2)|^2]E[|Y(f_1 + f_2)|^2]} \tag{2.56}$$

If there is no phase relationship among frequency components at f_1, f_2 in $x(t)$ and the frequency component at $f_1 + f_2$ in $y(t)$, the corresponding value of the cross-bicoherence will be near zero. If there is a phase relationship among these frequency components, the corresponding value of the cross-bicoherence will be near unity. Values of cross-bicoherence between zero and one indicate partial quadratic coupling.

To demonstrate this, we consider two signals $x(t)$ and $y(t)$ given by

$$\begin{aligned} x(t) &= a\cos(2\pi\omega_1 t + \theta_1) + c\cos[2\pi(\omega_1 + \omega_2)t + \theta_3] \\ &\quad + 2c\cos(2\pi\omega_1 t + \theta_1 + \alpha_1)\cos(2\pi\omega_2 t + \theta_2 + \alpha_2) + n_x(t) \end{aligned} \tag{2.57}$$

$$y(t) = b\cos(2\pi\omega_2 t + \theta_2) + n_y(t) \tag{2.58}$$

The sum component in $x(t)$ has two sources: one is independent (the second term on the right-hand side of Eq. (2.57) and the other results from the third term on the right-hand side of Eq. (2.57). Note also that the contributions of these sources are equal. The difference component in $x(t)$ results only from the third term on the right-hand side of Eq. (2.57). The computed time histories, power spectra, linear coherence, auto-bicoherence, and cross-bicoherence for $x(t)$ and $y(t)$ are shown in Figs. 2.11–2.16. As shown in Fig. 2.12, the power

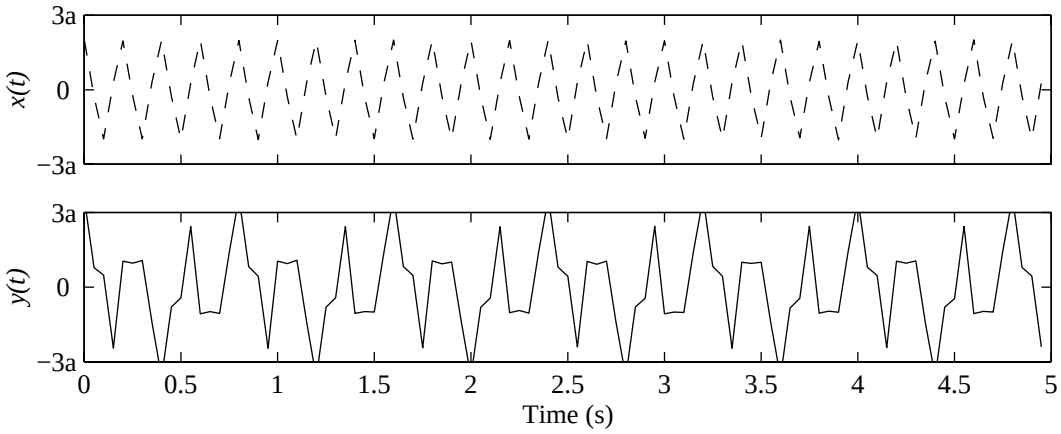

Figure 2.11: Time histories of $x(t)$ and $y(t)$ as defined in Eqs. (2.58)–(2.57).

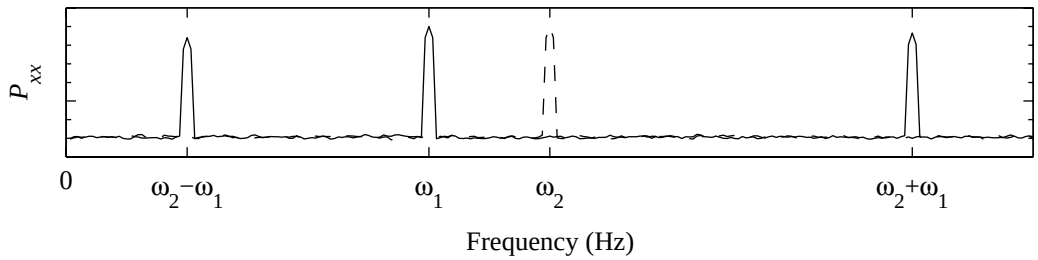

Figure 2.12: Power spectra of $x(t)$ and $y(t)$ as defined in Eqs. (2.58)–(2.57).

spectrum serves as a tool for identifying the frequency content of a signal. However, the power spectrum is not capable of detecting the quadratic nature of the frequency components and their phase couplings.

As shown in Fig. 2.13, the linear coherence does not detect any linear coupling between $x(t)$ and $y(t)$, which is expected. Using only the power spectra and linear coherence, one cannot determine if the two signals are independent or correlated. As shown in Figs. 2.14–2.15, the auto-bicoherence for either $x(t)$ or $y(t)$ indicates that there is no quadratic coupling among frequency components in either signal. However, the cross-bicoherence between $x(t)$

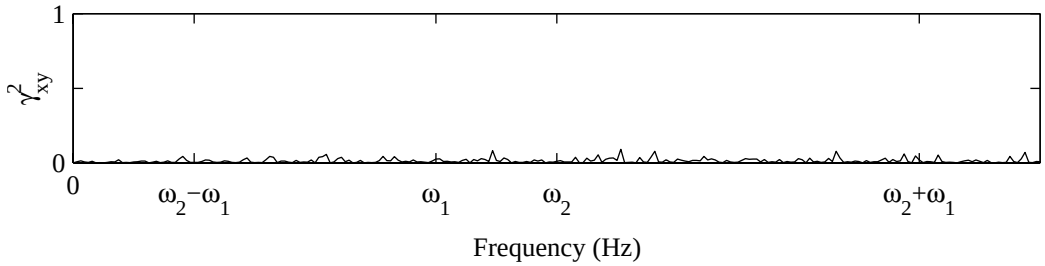

Figure 2.13: Linear coherence between $x(t)$ and $y(t)$ as defined in Eqs. (2.58)–(2.57).

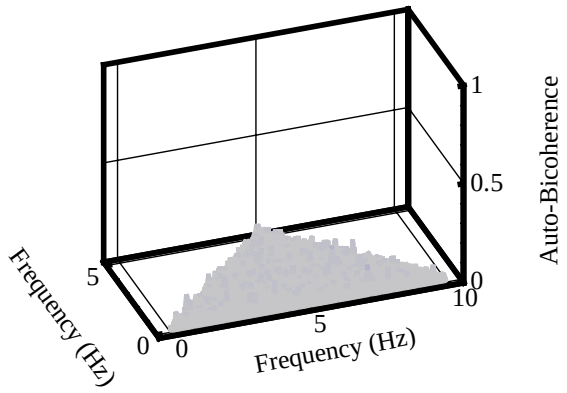

Figure 2.14: Auto-bicoherence of $x(t)$ as defined in Eq. (2.58). Here, $\omega_1 = 3.75$ Hz and $\omega_2 = 5$ Hz.

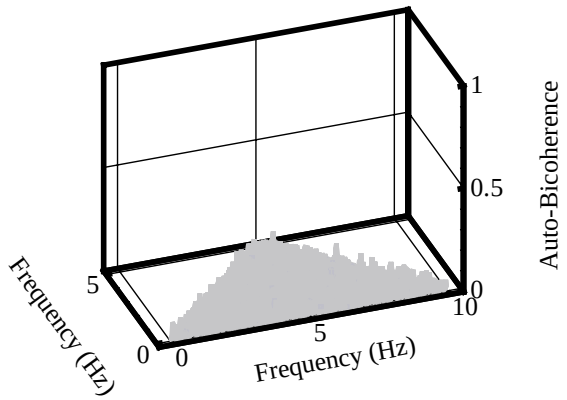

Figure 2.15: Auto-bicoherence of $y(t)$ as defined in Eq. (2.57). Here, $\omega_1 = 3.75$ Hz and $\omega_2 = 5$ Hz.

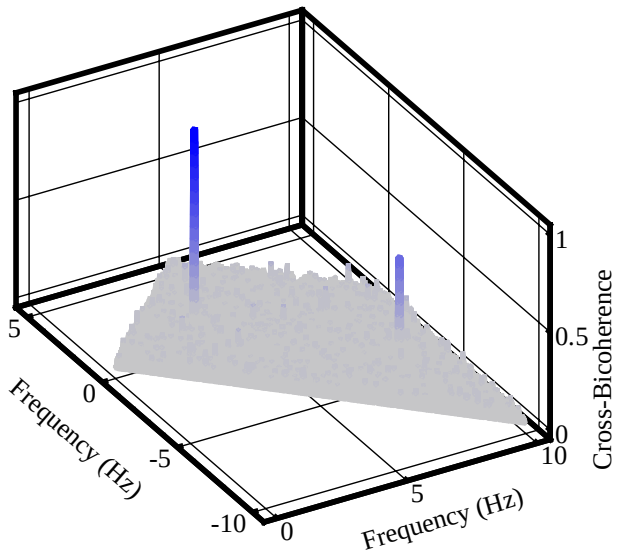

Figure 2.16: Cross-bicoherence between $x(t)$ and $y(t)$ as defined in Eqs. (2.58)–(2.57). Here, $\omega_1 = 3.75$ Hz and $\omega_2 = 5$ Hz.

and $y(t)$, shown in Fig. 2.16, contains a high peak of 0.99 at $(\omega_1, \omega_2 - \omega_1)$. This indicates almost total phase coupling among frequency components at ω_1 and $\omega_2 - \omega_1$ in $x(t)$ and a frequency component at $(\omega_2 - \omega_1) + \omega_1 = \omega_2$ in $y(t)$. Based on Eq. (2.58), the component at $\omega_2 - \omega_1$ in $x(t)$ is entirely generated as a difference component. Furthermore, the component at ω_1 in $x(t)$ and the component at ω_2 in $y(t)$ are related in phase to this difference component. This models a situation where components in a multiple-degree-of-freedom system combine in a quadratic fashion. This also models an input-output situation where a component of excitation $y(t)$ interacts with a component of response $x(t)$ to quadratically form new response components. From observing Eqs. (2.58)–(2.57), the phase relationship among ω_1, ω_2, and $\omega_2 - \omega_1$ should be

$$\theta_2 - \theta_1 - [(\theta_2 + \alpha_2) - (\theta_1 + \alpha_1)] = \alpha_1 - \alpha_2 \tag{2.59}$$

Since the cross-bispectrum preserves phase information between two quadratically coupled signals, the phase of the cross-bispectrum at $(\omega_1, \omega_2 - \omega_1)$ equals the phase of the component in $y(t)$ at ω_2 minus the phases of the components in $x(t)$ at ω_1 and at $\omega_2 - \omega_1$, which equals $\alpha_1 - \alpha_2$, as predicted in Eq. (2.59).

The cross-bicoherence between $x(t)$ and $y(t)$ also contains a peak of 0.47 at (ω_2, ω_1). This indicates partial coupling among the components at ω_1 in $x(t)$ and at ω_2 in $y(t)$ and the sum component in $x(t)$ at $\omega_1 + \omega_2$. The reason for this partial coupling is the independent component $c\cos[2\pi(\omega_1 + \omega_2)t + \theta_3]$ in $x(t)$, which has no phase relation to the other components. Because this independent component is equal in magnitude to the sum component, which does share a phase relationship with the other linear components, the corresponding cross-bicoherence peaks at almost 0.5. The small variance away from these ideal peak values is attributed to imperfections in the random number generator used to compute $x(t)$ and $y(t)$. The phase relationship among the components in $x(t)$ at ω_1 and in $y(t)$ at ω_2 and the sum component in $x(t)$ is

$$[(\theta_2 + \alpha_2) + (\theta_1 + \alpha_1)] - \theta_2 - \theta_1 = \alpha_1 + \alpha_2 \tag{2.60}$$

Because of the independent component in $x(t)$ at $\omega_1 + \omega_2$, the phase of the corresponding cross-bispectrum will not be equal to the phase predicted by Eq. (2.60).

As demonstrated in this example, the cross-bispectrum and cross-bicoherence functions are useful tools for detecting and quantifying quadratic coupling and corresponding phase relationships among frequency components in two signals. Note that it is impossible to reconstruct these phase relationships with the power spectra, which does not preserve phase

information, or the cross-power spectrum or linear coherence, which only detect linear phase coupling among components at the same frequency. Only the auto- and cross-bispectrum allow for the detection and quantification of phase coupling among frequency components of signals.

2.4 Proposed Nonlinear System Identification Methodology

We have been considering a parametric resonance of a nonlinear system that models the interaction between direct and parametric harmonic excitation with linear and nonlinear restoring, inertial, and damping forces. For the purposes of prediction and control of this system, an accurate model must be developed that fully quantifies the system dynamics. Accurate modeling requires estimates of the damping parameters μ_i, the linear natural frequency ω, the nonlinear geometric restoring force parameters α_i, the inertial nonlinearity parameter δ, and the excitation parameters η_i. Application of the method of multiple scales in Section 2.2 yields a uniform second-order exansion for the solution $u(t)$ of the system and its corresponding amplitude and phase modulation equations. From these equations, nonlinear phenomena such as static and dynamics bifurcations can be determined for the system. In these equations, the governing parameters are similar to the parameters found in the original differential equation except that both the excitation and the geometric/inertial nonlinearity parameters have been combined into effective excitation and nonlinearity pa-

rameters. This is possible because the resulting system dynamics are affected in the same way from either individual types of excitation or individual types of nonlinear restoring forces. In Section 2.3 we showed how the system response amplitudes and phases can be measured using higher-order spectral moments. Thus, based on the approximate solution and the spectral analysis measurements, one should be able to perform system identification. In the rest of this chapter, we combine these analyses to provide a methodology for the parameter identification.

2.4.1 Linear System Identification

For the purpose of system identification, information concerning the excitation and response measurements or simulations are assumed to be given. We propose a semi-inverse method for identification of the system parameters. Because many linear identification techniques are well estabilished and commonly available, they will be employed to identify as many of the linear system parameters as possible prior to nonlinear system identification.

The linear parameters in the system defined in Eq. (2.4) are the natural frequency ω and damping parameter μ_1. Both of these can be identified through obsevations of the free response of the system. A typical free-response time history is shown in Fig. 2.17. The free response of a system is dominated by the linear parameters of the system. In considering weak nonlinearities, the dominance of the linear restoring and damping forces allows for independent identification of the linear system parameters. Because the free response is a damped free response, the level of exponential decay, or the logarithmic decrement, provides

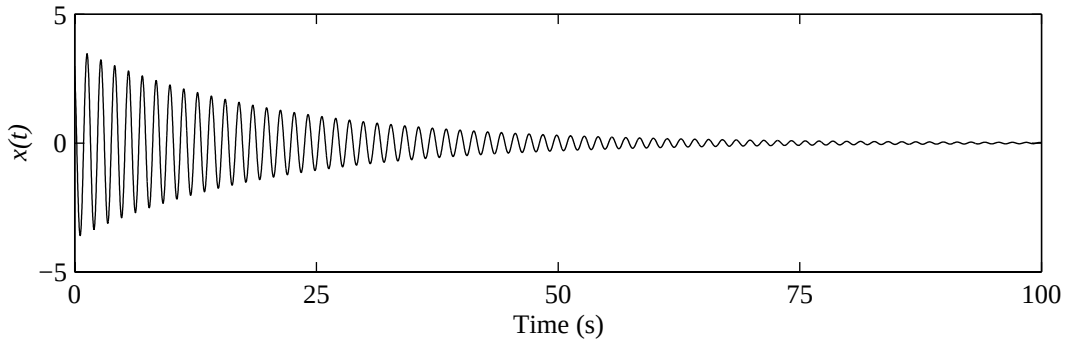

Figure 2.17: Typical time history for a free-response signal $x(t)$.

an estimate of the linear damping. For linearly damped oscillatory systems, the relationships among the natural frequency ω, damped frequency ω_d, linear damping parameter μ_1, and damping ratio ζ are given by

$$\mu_1 = \zeta\omega \tag{2.61}$$

$$\omega_d = \omega\sqrt{1-\zeta^2} \tag{2.62}$$

Combining these equations yields the following relationship among the natural frequency, the damped frequency, and the damping parameter:

$$\omega = \sqrt{\omega_d^2 + \mu_1^2} \tag{2.63}$$

From observations of many free responses over longer periods of time, the natural frequency and linear damping of a system can be accurately determined. For all of the following systems to be identified in this work, linear system identification is assumed to be performed using the techniques discussed in this section, unless otherwise stated.

2.4.2 Nonlinear Phase Relationship

For the system defined in Eq. (2.4), we recall that the phase relationship from Eq. (2.34) between the excitation phase τ_e and the response phase β is given by

$$\gamma = \epsilon^2 \sigma t + \tau_e - 2\beta \tag{2.64}$$

The phase quantity γ represents a phase difference between the phase of the excitation at the excitation frequency Ω and twice the phase of the response at half the excitation frequency, or $\Omega/2$. Note that the system response is synchronized to half the excitation frequency instead of its linear frequency ω. The nonlinearity adjusts the frequency of the steady-state response to one-half that of the excitation.

Note that simply taking the Fourier transforms of the two signals and adding the phases corresponding to the appropriate frequency components will not provide γ. The relationship expressed by γ describes a phase difference that exists over time; because the Fourier transforms of the two signals represent averages over time, combining them in this post-processing manner loses this relationship. One must compute this nonlinear phase quantity for each ensemble and then take the average over all of the ensembles. We can represent Eq. (2.64) in the form

$$\gamma = \tau_e(\Omega) - 2\tau_r(\frac{1}{2}\Omega) \tag{2.65}$$

which is the phase of the cross-bispectrum between the excitation and response signals at ($\Omega/2$,$\Omega/2$). Using the notation from Section 2.3.2, we can express this phase relationship as

$$\gamma = \angle B_{err}(\frac{1}{2}\Omega, \frac{1}{2}\Omega) \tag{2.66}$$

where e stands for excitation and r stands for response. In this sense, γ measures the phase coupling between the excitation and the resulting response at half the excitation frequency. This phase relationship can also be expressed as

$$\gamma = [\tau_e(\Omega) - \tau_r(\Omega)] + [\tau_r(\Omega) - 2\tau_r(\frac{1}{2}\Omega)] \tag{2.67}$$

Using the notation from Sections 2.3.1–2.3.2, we can express the relationship in Eq. (2.67) as

$$\gamma = \angle P_{er}(\Omega) + \angle B_{rrr}(\frac{1}{2}\Omega, \frac{1}{2}\Omega) \tag{2.68}$$

In this way, γ is the sum of the phase of the cross-power spectrum at Ω, $\angle P_{er}(\Omega)$, and the phase of the response auto-bispectrum at $(\Omega/2,\Omega/2)$, $\angle B_{rrr}(\Omega/2, \Omega/2)$. While this involves lower-order tools such as the cross-power spectrum, this relationship can only be useful if there is a frequency component in the response at the excitation frequency Ω. If there is no significant component at Ω, then the magnitudes of the cross-power spectrum and auto-bispectrum will be too small for accurate estimates of these phases.

2.4.3 Nonlinear System Identification

In considering the steady-state oscillations of the system, the amplitude and phase cease to vary with time, and the amplitude and phase modulation equations become

$$-\omega\mu_1 a - \frac{4}{3\pi}\mu_2\omega^2 a^2 + \eta_e f a \sin\gamma = 0 \tag{2.69}$$

$$\frac{1}{2}a\omega\sigma + \alpha_e a^3 + \eta_e f a \cos\gamma = 0 \tag{2.70}$$

Rearranging these equations, one obtains

$$a = \frac{\eta_e}{\frac{4}{3\pi}\mu_2\omega^2} f \sin\gamma - \frac{\mu_1}{\frac{4}{3\pi}\mu_2\omega} \tag{2.71}$$

$$a^2 = -\frac{\eta_e}{\alpha_e} f \cos\gamma - \frac{1}{2}\frac{\omega\sigma}{\alpha_e} \tag{2.72}$$

Equations (2.71)–(2.72) are linear relationships between a and $f\sin\gamma$ and a^2 and $f\cos\gamma$. This suggests that identification of the nonlinear system parameters could be performed by observing these linear relationships in the system. This identification is to be performed assuming that measurements are taken for the excitation magnitude f and frequency Ω and response amplitude a. This nonlinear identification also assumes that the damping parameter μ_1 has been identified through linear identification techniques. Furthermore, γ must be calculated to build these relationships between a and $f\sin\gamma$ and a^2 and $f\cos\gamma$.

As discussed in Section 2.4.2, γ can be calculated using higher-order spectra. The response amplitude a can then be plotted versus $f\sin\gamma$ to obtain η_e and μ_2. The response amplitude squared a^2 can be plotted versus $f\cos\gamma$ to obtain α_e and σ. Linear curve fits for these experimentally generated plots can then be compared with Eqs. (2.71) and (2.72) to identify α_e, η_e, μ_2, and ω. The natural frequency ω can be identified here as well as in the linear system identification because nonlinear systems are usually highly sensitive to the detuning σ. Errors in the calculations will be minimized using as few parameters as possible during the nonlinear system identification, and the easiest parameter to identify with confidence is the linear damping μ_1.

Figures 2.18 and 2.19 show typical experimentally-obtained plots of a vs $f\sin\gamma$ and a^2 vs $f\cos\gamma$. The curve fits shown in Figs. 2.18 and 2.19 are in the form

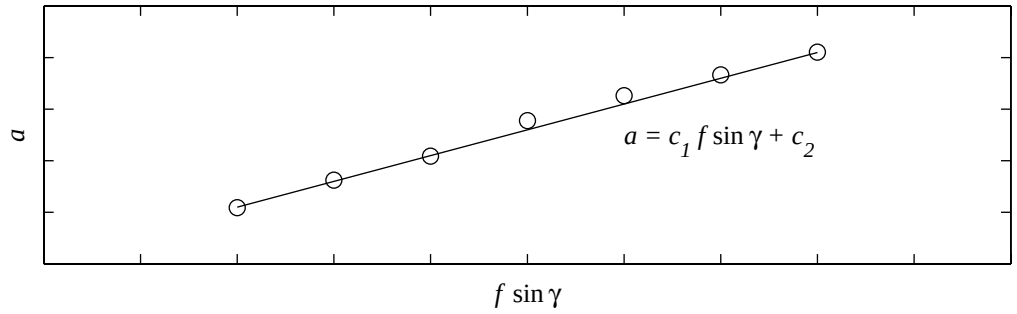

Figure 2.18: A typical plot of a vs $f \sin\gamma$ for a system with all of the nonlinearities considered in Section 2.2.1. The linear curve fit shown is in the form $a = c_1 f \sin\gamma + c_2$.

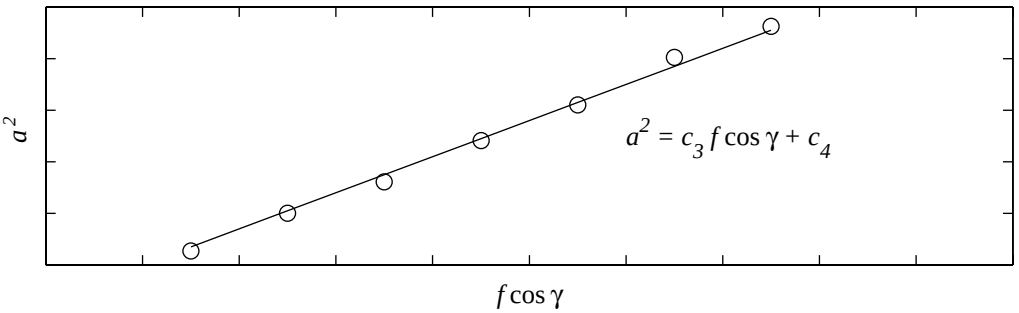

Figure 2.19: A typical plot of a^2 vs $f \cos\gamma$ for a system with all of the nonlinearities considered in Section 2.2.1. The linear curve fit shown is in the form $a^2 = c_3 f \cos\gamma + c_4$.

$$a = c_1 f \sin\gamma + c_2 \tag{2.73}$$

$$a^2 = c_3 f \cos\gamma + c_4 \tag{2.74}$$

Comparing the curve fits in Eqs. (2.73) and (2.74) with the steady-state modulation equations (2.71) and (2.72), we obtain the following solution for the parameters:

$$\eta_e = \frac{c_1\mu_1}{2c_2^2 c_3}(\Omega c_2 c_3 - 2c_1 c_4 \mu_1) \tag{2.75}$$

$$\alpha_e = -\frac{c_1\mu_1}{2c_2^2 c_3^2}(\Omega c_2 c_3 - 2c_1 c_4 \mu_1) \tag{2.76}$$

$$\mu_2 = \frac{3\pi c_3 \mu_1}{2\Omega c_2 c_3 - 4c_1 c_4 \mu_1} \tag{2.77}$$

$$\omega = \frac{\Omega}{2} - \frac{c_1 c_4 \mu_1}{c_2 c_3} \tag{2.78}$$

From these linear curve fits, direct nonlinear system identification can be performed.

While this methodology has been presented for cases with quadratic damping and nonlinear restoring forces, it can be extended to identify systems with other types of damping and nonlinear restoring forces. For example, consider our nonlinear system with only linear damping. In this case, the steady-state amplitude equation becomes

$$f \sin\gamma = \frac{\omega\mu_1}{\eta_e} \tag{2.79}$$

which suggests a constant value for $f \sin\gamma$. Solving Eqs. (2.74) and (2.79) yields the parameters

$$\eta_e = \frac{\mu_1}{2c_3 c_5^2}(\Omega c_3 c_5 - 2c_4 \mu_1) \tag{2.80}$$

$$\alpha_e = -\frac{\mu_1}{2c_3^2 c_5^2}(\Omega c_3 c_5 - 2c_4 \mu_1) \tag{2.81}$$

$$\omega = \frac{\Omega}{2} - \frac{c_4 \mu_1}{c_3 c_5} \tag{2.82}$$

As another example, consider our nonlinear system with linear and quadratic damping but without nonlinear restoring forces. The steady-state phase equation then becomes

$$f\cos\gamma = -\frac{\omega\sigma}{2\eta_e} \tag{2.83}$$

which suggests a constant value for $f\cos\gamma$. Solving Eqs. (2.73) and (2.83) yields the parameters

$$\eta_e = \frac{c_1\mu_1}{2c_2^2}(\Omega c_2 + 2c_1c_6\mu_1) \tag{2.84}$$

$$\mu_2 = \frac{3\pi\mu_1}{2\Omega c_2 + 4c_1c_6\mu_1} \tag{2.85}$$

$$\omega = \frac{\Omega}{2} + \frac{c_1c_6\mu_1}{c_2} \tag{2.86}$$

The nonlinearities modeled by Eq. (2.4) consist of quadratic damping and quadratic and cubic restoring forces. The nonlinear identification process described in this section involves fitting variations of a vs $f\sin\gamma$ and a^2 vs $f\cos\gamma$ with only polynomials. Other types of damping or nonlinear restoring forces can be modeled and identified in a manner similar to that described in this section, especially if their effects on the steady-state amplitude and phase are polynomial in nature. In these cases, the variations of a vs $f\sin\gamma$ and a^2 vs $f\cos\gamma$ can also be described using polynomials.

2.4.4 Methodology Summary

Combining the method of multiple scales and higher-order spectral analysis techniques, we presented a methodology for linear and nonlinear system identification of systems modeled by Eq. (2.4). This methodology is outlined as follows:

Step 1: *Measure the excitation magnitude and frequency and the response amplitude over a range of observed steady-state oscillations.*

Step 2: *Identify the linear damping parameter μ_1 using conventional linear system identification techniques.*

Step 3: *Calculate the nonlinear phase difference γ using the bispectrum.*

Step 4: *Plot the experimentally measured a vs $f \sin\gamma$ and characterize the damping in the system.*

Step 5: *Plot the experimentally measured a^2 vs $f \cos\gamma$ and characterize the restoring forces in the system.*

Step 6: *Using the method of multiple scales, determine the steady-state amplitude and phase equations for the nonlinear model.*

Step 7: *Based on the assumed types of damping and nonlinear restoring forces, perform nonlinear system identification.*

Note that all of the relevant steady-state system dynamics are quantified in Eqs. (2.71) and (2.72). To determine the relationships between the excitation amplitude or frequency and the steady-state response amplitude, one can eliminate γ in these equations and obtain a single equation that can be used to solve for a from selected combinations of f and σ. Some system identification techniques have been developed that perform this elimination of γ (Fahey et al, 1998; Nayfeh, 1985). These techniques exploit jump phenomena or system bifurcations to capture and identify the various nonlinear parameters. However, the advantage of preserving γ in the identification process is that it provides the types of damping and

nonlinear restoring forces involved in the system. Furthermore, provided that measurements of γ are available, the system identification methodology outlined above makes use of algebraic relationships in the steady-state modulation equations, which are highly inexpensive to generate in terms of the number of computations.

Chapter 3

Numerical Simulations

In this chapter, numerical simulations are carried out to show the effectiveness of the methodology proposed in Chapter 2 for nonlinear system identification. These numerical simulations are carried out for two different types of damping. These cases are modeled only with cubic nonlinearities and parametric excitation because the general effect of geometric nonlinearities and excitation can be combined into effective nonlinearity and excitation parameters, as described in Chapter 2.

Table 3.1: Parameters used to simulate the system modeled in Eq. (3.1) with linear damping, cubic geometric nonlinearities, and parametric excitation.

Parameter	Selected Value
ω	5.5 Hz
α_3	333.33
η_2	60
μ_1	0.3

3.1 Case 1: Case of Linear Damping

3.1.1 Parameter Selection and Numerical Simulations

In this case, we consider a system with linear damping only, cubic geometric nonlinearities, and parametric excitation. This system is given by

$$\frac{d^2u}{dt^2} + \omega^2 u + 2\epsilon^2\mu_1\frac{du}{dt} + \epsilon^2\alpha_3 u^3 = \epsilon^2\eta_2 f u\cos(\Omega t + \tau_e) \tag{3.1}$$

where values for the system parameters are listed in Table 3.1. Solutions to Eq. (3.1) were obtained using the method of multiple scales. Time histories for the solution to Eq. (3.1) were obtained using a Runge-Kutta 4th-order integration routine with a time step of 0.000985 seconds. The simulation length is 500 seconds. In the numerical integration, the scaling parameter ϵ is set equal to unity, and all of the other parameters are set equal to zero. To induce a principal parametric resonance, we chose values for the excitation frequency near twice the natural frequency ω of the system. The excitation phase τ_e is set equal to zero. For certain ranges in the excitation frequency and amplitude, a principal parametric response

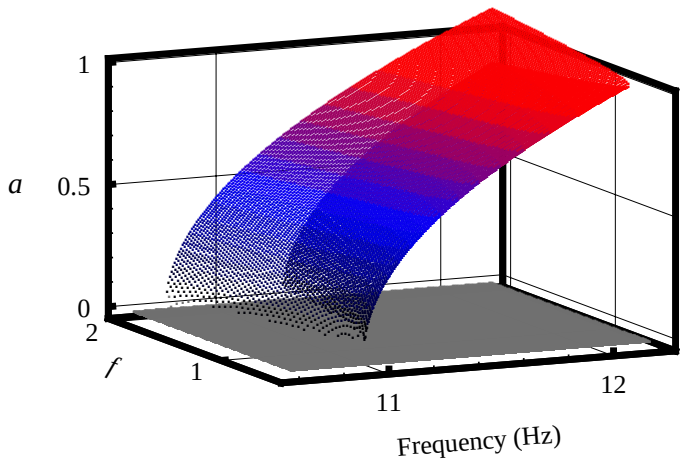

Figure 3.1: Variation of the response amplitude with the excitation amplitude and frequency for the system modeled in Eq. (3.1) with the parameters defined in Table 3.1.

was observed, meaning that nontrivial steady-state oscillations at a frequency close to the natural frequency ω were observed.

A plot of the response amplitude as a function of the excitation amplitude and frequency is shown in Fig. 3.1. These amplitudes were determined using the method of multiple scales. The excitation frequency ranges from 10.6 to 12.196 Hz and the excitation amplitude ranges from 0.5 to 2.0 units. The resulting response amplitudes were observed to be between 0 and 1.12 units. For the identification, we set the excitation frequency at $\Omega = 11.1$ Hz and the excitation amplitude from 1.1 to 2. The force-response curve for this data is shown in Fig. 3.2 and representative time histories of the excitation and response are shown in Fig. 3.3.

3.1.2 Parameter Identification using Simulated Data

Parameter identification is performed using only the data runs corresponding to the force-response curve shown in Fig. 3.2. The identification is performed according to the following

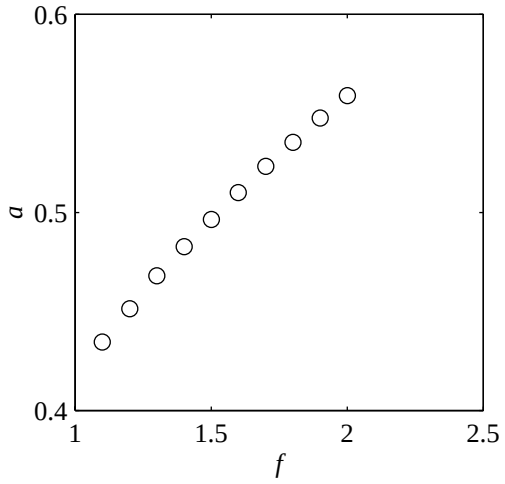

Figure 3.2: The force-response curve of the system modeled in Eq. (3.1) with the parameters defined in Table 3.1.

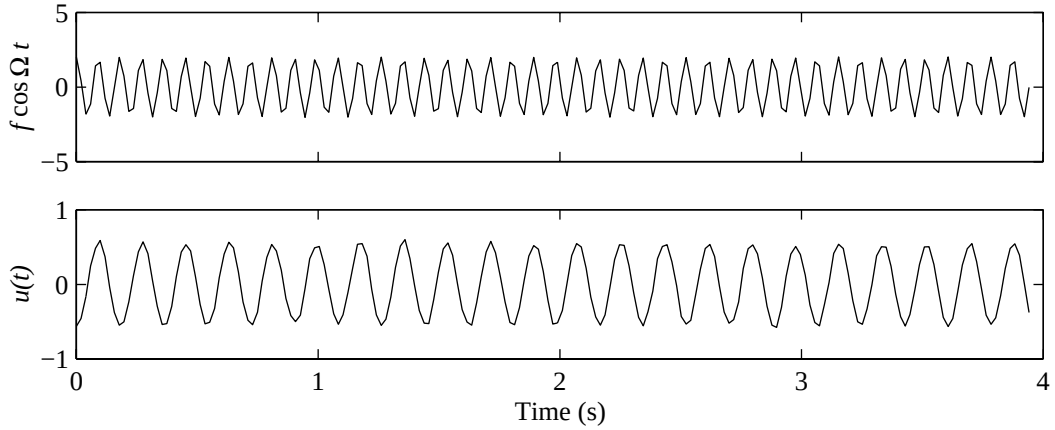

Figure 3.3: Representative time histories for the system modeled in Eq. (3.1) with the parameters defined in Table 3.1.

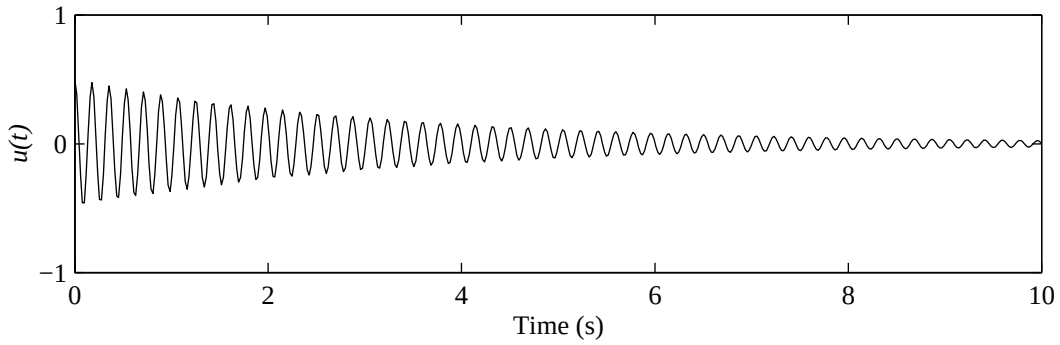

Figure 3.4: A representative free response for the system modeled in Eq. (3.1) with the parameters defined in Table 3.1.

steps. First, identification of the linear parameters is performed. Second, bispectrum estimates are used to quantify the nonlinear phase relationships. Third, phase measurements are substituted into the approximate solution for identification of the nonlinear parameters. Finally, the resulting identified parameters are compared with the original system parameters in Table 3.1.

Linear System Identification

The linear damping parameter μ_1 is identified from the free response of the system. The other system parameters are identified by exploiting nonlinear resonances as discussed in the previous chapter. Setting the excitation amplitude equal to zero, we calculated the free response shown in Fig. 3.4. Based on the log-decrement methodology, the linear damping parameter μ_1 is estimated to be 0.3 Hz. This estimate is in agreement with the value given in Table 3.1.

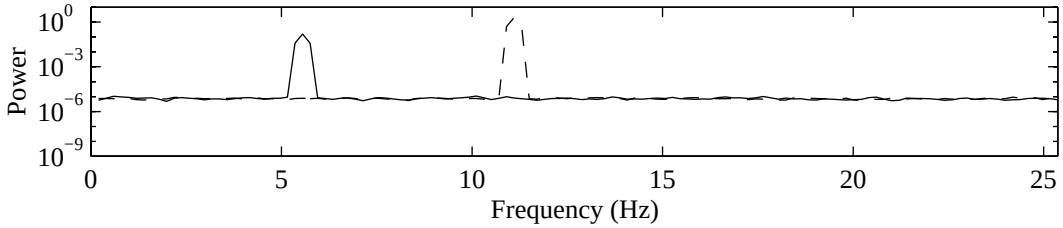

Figure 3.5: Representative power spectra of the excitation (dotted) and response (solid) for the system modeled in Eq. (3.1) with the parameters defined in Table 3.1.

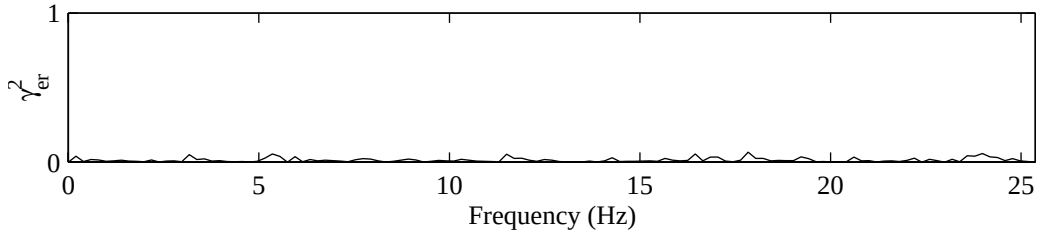

Figure 3.6: A representative linear coherence for the system modeled in Eq. (3.1) with the parameters defined in Table 3.1.

Frequency-Domain Analysis and Nonlinear Phase Relationships

The first step in our analysis is to obtain an estimate of the power spectra, which is shown in Fig. 3.5. This figure shows that the excitation consists of a single component at 11.1 Hz and that the response consists of a single component at 5.55 Hz. The analysis was performed by averaging 64 records, each consisting of 256 samples. Because the excitation- and response-frequency components are different, the linear coherence between the two, as shown in Fig. 3.6, is near zero over all frequencies. This indicates that there is no linear relationship between the excitation and response. This points to a nonlinear mechanism for the energy transfer from the excitation to the response of the system. Moreover, because the excitation is composed of a single-linear-frequency component, the excitation auto-bicoherence should

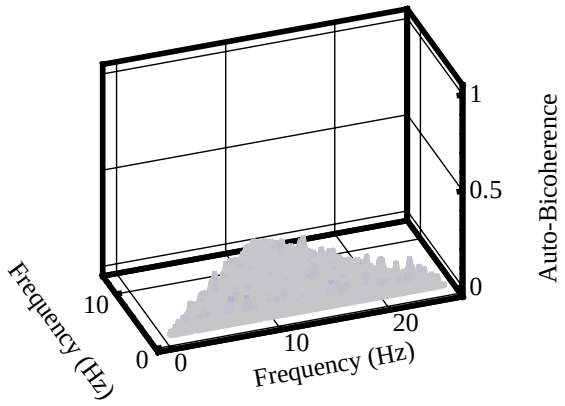

Figure 3.7: A representative auto-bicoherence of the response for the system modeled in Eq. (3.1) with the parameters defined in Table 3.1.

also be zero over the entire two-dimensional frequency domain. Because the response is also composed of a single-frequency component (the parametric response), the response auto-bicoherence, as shown in Fig. 3.7, is also zero over the entire two-dimensional frequency domain. To detect any quadratic phase coupling between the excitation and response, we calculated the cross-bicoherence. As shown in Fig. 3.8, a high peak in the cross-bicoherence is detected at (5.55 Hz, 5.55 Hz) which indicates coupling between the excitation at 11.1 Hz and the response at 5.55 Hz. The results of the frequency-domain analysis for all of the runs shown in Fig. 3.2 are summarized in Table 3.2. This table includes estimates of the excitation amplitude, the response amplitude, the cross-bicoherence at (5.55 Hz, 5.55 Hz), and the phase of the cross-bispectrum at (5.55 Hz, 5.55 Hz). The high values of the cross-bicoherence indicate that the variance of the measured phase $\angle B_{err}(\frac{1}{2}\Omega, \frac{1}{2}\Omega)$ is very small and could thus be used as a good estimate of γ as defined in Eq. (2.66).

Table 3.2: Frequency-domain analysis summary for the system modeled in Eq. (3.1) with the parameters defined in Table 3.1.

f	a	$b^2_{err}(\frac{1}{2}\Omega, \frac{1}{2}\Omega)$	$\angle B_{err}(\frac{1}{2}\Omega, \frac{1}{2}\Omega)$
			deg
1.1	0.4346	0.999	41.1
1.2	0.4514	0.999	37.2
1.3	0.4681	0.999	34.2
1.4	0.4827	0.999	31.8
1.5	0.4965	0.999	29.6
1.6	0.5100	0.999	27.7
1.7	0.5233	0.999	26.1
1.8	0.5354	0.999	24.7
1.9	0.5477	0.999	23.3
2.0	0.5590	0.999	22.2

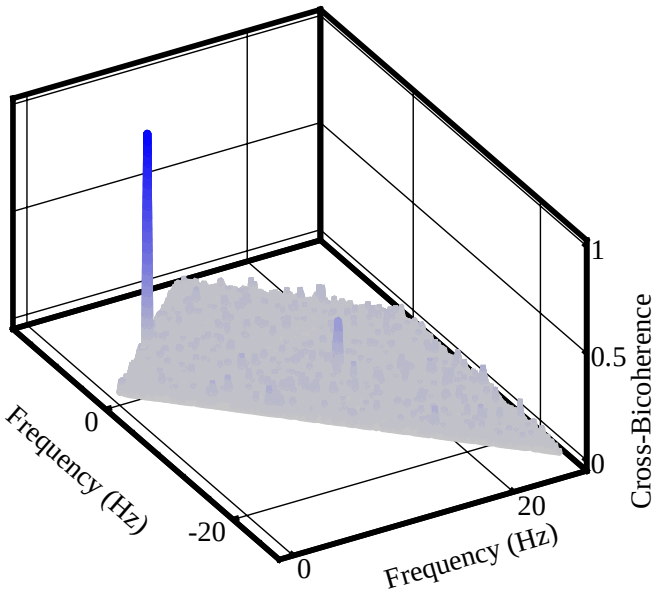

Figure 3.8: A representative cross-bicoherence for the system modeled in Eq. (3.1) with the parameters defined in Table 3.1.

Damping and Nonlinear Parameter Identification

To characterize and identify the damping and nonlinear parameters, we examined the order of the polynomial relationships between a and $f\sin\gamma$ and a^2 and $f\cos\gamma$. Using the values of f, a, and γ from Table 3.2, we plot in Figs. 3.9 and 3.10 a vs $f\sin\gamma$ and a^2 vs $f\cos\gamma$.

The results show that $f\sin\gamma$ is not dependent on a and that $f\cos\gamma$ varies linearly with a^2. The constant value observed for $f\sin\gamma$ indicates the presence of only linear damping, as discussed in Section 2.4.3. Furthermore, the linear relationship observed in the variation of a^2 with $f\cos\gamma$ indicates the presence of nonlinear restoring forces, which is also discussed in Section 2.4.3. Computing a linear curve fit for each of these relationships yields

$$f\sin\gamma = 0.7410 \tag{3.2}$$

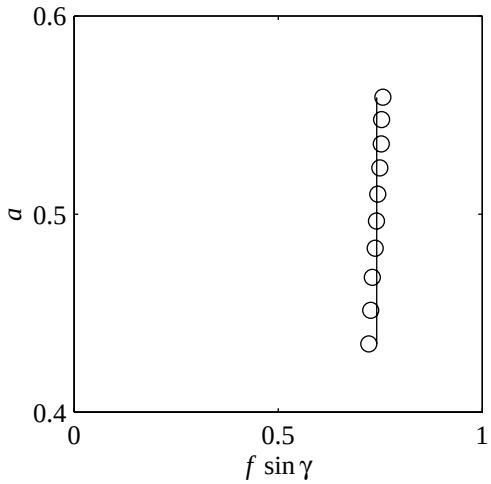

Figure 3.9: A plot of a versus $f \sin\gamma$ for the system modeled in Eq. (3.1) with the parameters defined in Table 3.1.

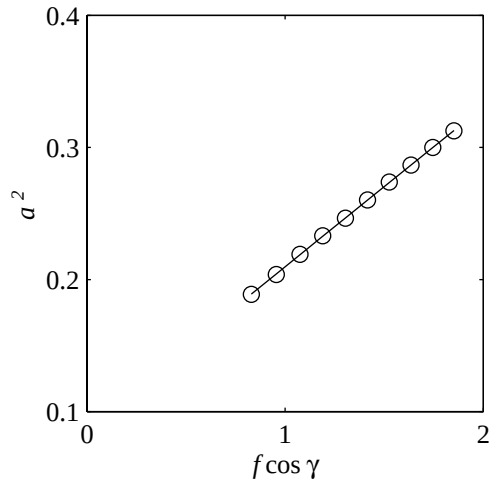

Figure 3.10: A plot of a^2 versus $f \cos\gamma$ for the system modeled in Eq. (3.1) with the parameters defined in Table 3.1.

Table 3.3: Identified parameters for the system modeled in Eq. (3.1) with linear damping only, cubic geometric nonlinearities, and parametric excitation.

Parameter	Identified Value	Actual Value	Percent Error
ω	5.5029 Hz	5.5	0.0535
α_3	308	333	-7.58
η_2	56	60	-6.68
μ_1	0.3	0.3	0.0

and

$$a^2 = 0.1212 f \cos\gamma + 0.0885 \tag{3.3}$$

Comparing these linear curve fits with the steady-state equations listed in Eqs. (2.72)–(2.79), and solving for the parameters using Eqs. (2.80)–(2.82), we identified and quantified the nonlinear parameters. As shown in Table 3.3, the identified nonlinear parameters are within seven percent of the actual values.

We should note here that the estimates of these parameters can vary significantly with small variations of γ. For instance, a two-degree change in the measurement of γ could correspond to a five percent change in the computed values of α_3 and η_2. Errors in the measurement of γ may arise from the simulated system being slightly away from steady state, using a finite-time step in the simulations, using a finite-record length in the frequency-domain analysis, or averaging a finite number of samples. These errors may be reduced through longer simulations with a smaller time step and longer records with more samples considered during the frequency-domain analysis.

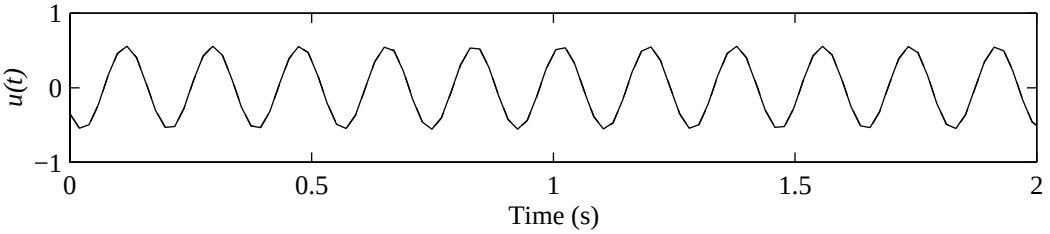

Figure 3.11: Representative comparison between time histories computed using the acual (solid) and identified (dashed) parameters for the system modeled in Eq. (3.1) with all of the defined nonlinearities.

Comparison between Actual and Identified Parameters

To determine the accuracy of the model with the identified parameters, we performed simulations with the newly identified parameters and made comparisons with the actual simulated time histories. This comparison is shown in Fig. 3.11. The results show that the estimated parameters can very satisfactorily predict the response of a parametrically excited system with only linear damping and nonlinear restoring forces.

3.2 Case 2: Case of Linear and Quadratic Damping

3.2.1 Parameter Selection and Numerical Simulations

To check the power of the proposed methodology in characterizing damping, we considered a nonlinear system with linear and quadratic parameters μ_1 and μ_2, respectively. This system is given by

$$\frac{d^2u}{dt^2} + \omega^2 u + 2\epsilon^2\mu_1\frac{du}{dt} + \epsilon^2\mu_2\frac{du}{dt}\left|\frac{du}{dt}\right| + \epsilon^2\alpha_3 u^3 = \epsilon^2\eta_2 f u\cos(\Omega t + \tau_e) \tag{3.4}$$

Table 3.4: Parameter used to simulate the system modeled in Eq. (3.4) with all of the defined nonlinearities.

Parameter	Selected Value
ω	5.5 Hz
α_3	333.33
η_2	60
μ_1	0.3
μ_2	0.04

where values for the system parameters are given in Table 3.4. Solutions to Eq. (3.4) were obtained using the method of multiple scales. Time histories for the solution of Eq. (3.4) were obtained using a Runge-Kutta 4th-order integration routine with a time step of 0.000985 seconds. The simulation length is 500 seconds. In the numerical simulation, the scaling parameter ϵ is set equal to unity. To induce a principal parametric resonance, we chose values for the excitation frequency near twice the natural frequency ω of the system. For certain ranges in excitation frequency and amplitude, a principal parametric response was observed, meaning that nontrivial steady-state oscillations at a frequency close to the natural frequency ω were observed.

A plot of the response amplitude as a function of the excitation amplitude and frequency is shown in Fig. 3.12. These amplitudes were determined using the method of multiple scales. This plot covers a range of excitation frequencies from 10.6 to 12.196 Hz and a range of excitation amplitudes from 0.5 to 2.0 units. The resulting response amplitudes were observed to be between 0 and 0.96 units. The simulated set of experimental data to

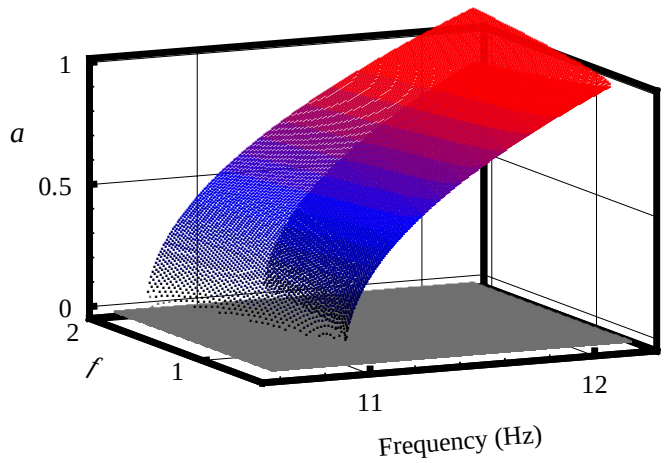

Figure 3.12: The response amplitude as a function of the excitation amplitude and frequency for the system modeled in Eq. (3.4) with the parameters defined in Table 3.4.

be used for parametric identification is chosen from the domain of excitation amplitude and frequency shown in Fig.3.12. The excitation frequency is set at $\Omega = 11.1$ Hz, the excitation phase is set at $\tau_e = 0$ rad, and the excitation amplitude is varied from 1.1 to 2 units. A corresponding force-response curve is shown in Fig. 3.13 and representative time histories of the excitation and response are shown in Fig. 3.14.

3.2.2 Parameter Identification using Simulated Data

The linear damping parameter μ_1 is identified from the free response of the system. Setting the excitation amplitude equal to zero, we calculated the free response of the system shown in Fig. 3.15. Measuring the exponential decay of this free response yields a rate given by $e^{-0.3t}$, which gives a linear damping parameter of $\mu_1 = 0.3$ Hz, which is in agreement with the value of μ_1 listed in Table 3.4.

A frequency-domain analysis, similar to that discussed in Section 3.1.2, is performed by

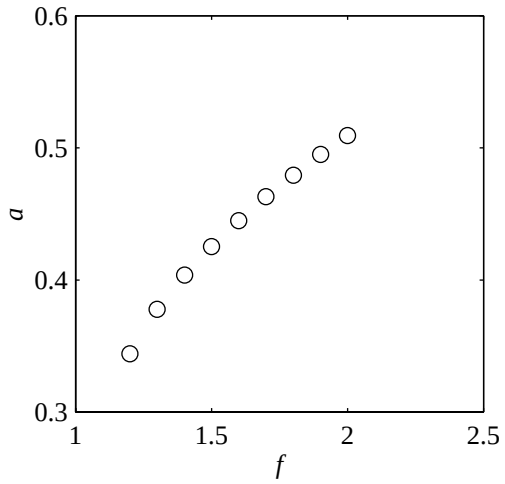

Figure 3.13: The force-response curve for the system modeled in Eq. (3.4) with the parameters whose parameters are defined in Table 3.4.

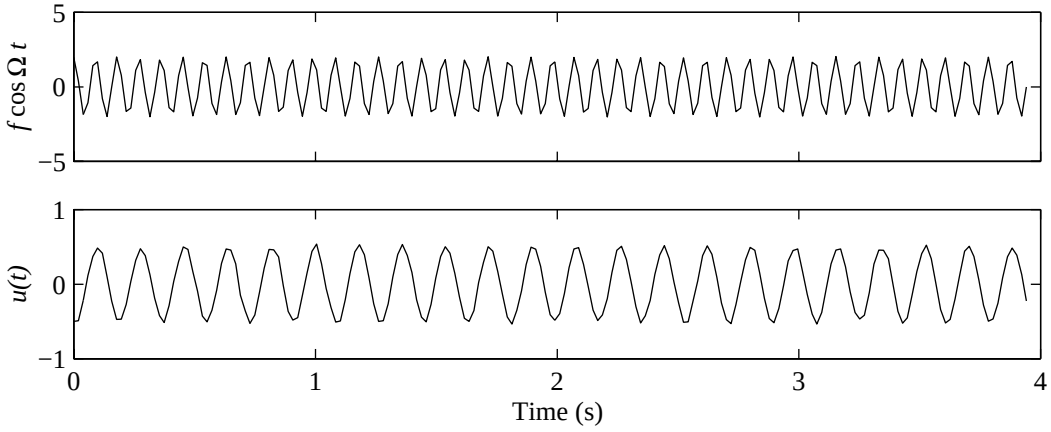

Figure 3.14: Representative time histories for the system modeled in Eq. (3.4) with the parameters defined in Table 3.4.

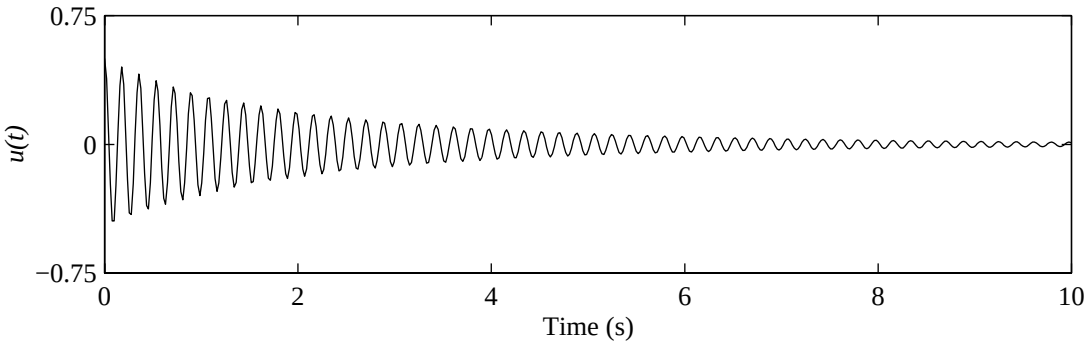

Figure 3.15: A representative free response for the system modeled in Eq. (3.4) with the parameters defined in Table 3.4.

averaging 64 samples of length 256. The results of the frequency-domain analysis, which includes the excitation and response amplitudes, cross-bicoherence, and phase of the cross-bispectrum at (5.55 Hz, 5.55 Hz) are shown in Table 3.5. The phase quantity $\angle B_{err}(\frac{1}{2}\Omega, \frac{1}{2}\Omega)$ is equivalent to the nonlinear phase difference γ as defined in Eq. (2.66); it is calculated at each excitation/response level. As discussed above, the damping and nonlinear characteristics are determined from the order of the polynomial relationships between a and $f\sin\gamma$ and a^2 and $f\cos\gamma$. Plots of a versus $f\sin\gamma$ and a^2 versus $f\cos\gamma$ are computed and shown in Figs. 3.16–3.17. The results clearly show linear relationships between a and $f\sin\gamma$ and a^2 and $f\cos\gamma$. The linear relationship observed between a and $f\sin\gamma$ indicates the presence of both linear and quadratic damping, as discussed in Section 2.4.3. Furthermore, the linear relationship observed in a^2 and $f\cos\gamma$ indicates the presence of nonlinear restoring forces, which is also discussed in Section 2.4.3.

Computing a linear curve fit for each of these relationships yields

$$a = 0.6304 f\sin\gamma - 0.39858 \tag{3.5}$$

Table 3.5: Frequency-domain analysis summary for the system modeled in Eq. (3.4) with the parameters defined in Table 3.4.

f	a	$b^2_{err}(\frac{1}{2}\Omega, \frac{1}{2}\Omega)$	$\angle B_{err}(\frac{1}{2}\Omega, \frac{1}{2}\Omega)$
			deg
1.1	0.2933	0.999	92
1.2	0.3441	0.999	79
1.3	0.3778	0.999	71
1.4	0.4036	0.999	65
1.5	0.4253	0.999	61
1.6	0.4450	0.999	57
1.7	0.4632	0.999	53
1.8	0.4794	0.999	51
1.9	0.4951	0.999	48
2.0	0.5093	0.999	47

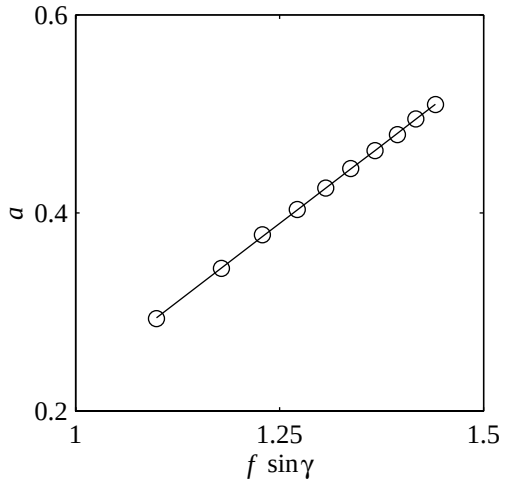

Figure 3.16: Plot of a versus $f \sin\gamma$ for the system modeled in Eq. (3.4) with the parameters defined in Table 3.4.

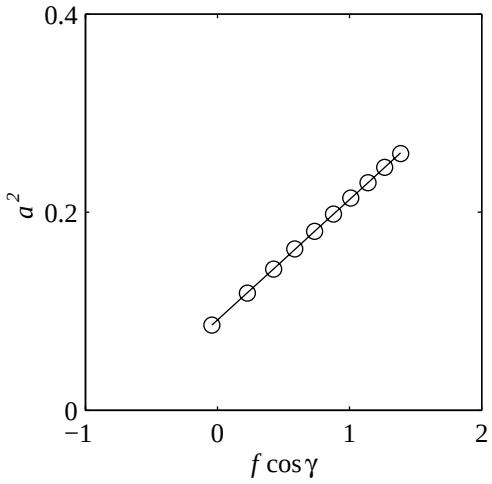

Figure 3.17: Plot of a^2 versus $f\cos\gamma$ for the system modeled in Eq. (3.4) with the parameters defined in Table 3.4.

and

$$a^2 = 0.1217 f\cos\gamma + 0.0911 \tag{3.6}$$

Comparing these curve fits with the steady-state equations listed in Eqs. (2.71) and (2.72) and solving for the parameters using Eqs. (2.75)–(2.78), we obtained the nonlinear parameters. A summary of these parameters is given in Table 3.6. The identified nonlinear parameters are within 8 and 30% of the actual values. We should note that a two-degree change in the measurement of γ roughly corresponds to a 5% change in the computed values for α_3 and η_2 and a 30% change in the computed value for μ_2. Certainly, the effects of this error on the simulation are determed by the relative importance of the linear and quadratic damping.

Again, errors in the estimates of γ may arise from the simulations being slightly away from steady state, using a finite-time step in the simulations, using a finite FFT length in the frequency-domain analysis, or averaging a finite number of samples. These errors may

Table 3.6: Identified parameters for the system modeled in Eq. (3.4) with all of the defined nonlinearities.

Parameter	Identified Value	Actual Value	Percent Error
ω	5.4935	5.5	-0.12
α_3	358	333	7.57
η_2	65	60	8.33
μ_1	0.3	0.3	0.0
μ_2	0.0513	0.04	28.3

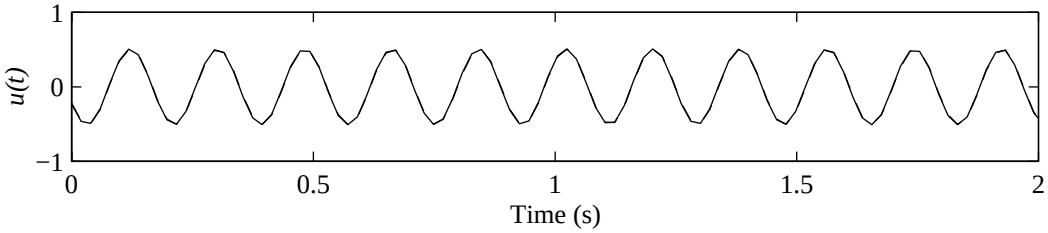

Figure 3.18: Representative comparison between time histories computed using the actual (solid) and identified (dashed) parameters for the system modeled in Eq. (3.4) with all of the defined nonlinearities.

be reduced through longer simulations with a smaller time step and longer FFT lengths with more samples considered during the frequency-domain analysis. To determine the goodness of the identified parameters, we performed simulations with these parameters. The new simulation time histories are compared with the actual simulation time histories in Fig. 3.18. The results show that the proposed methodology, despite the relatively large error in μ_2, is very successful in identifying the parameters for a parametrically excited system with linear and quadratic damping and nonlinear restoring forces. The relative insensitivity to μ_2 is most likely because $\mu_2 du/dt|du/dt|$ is much smaller than $\mu_1 du/dt$. This difference in

magnitude is due to the magnitude of du/dt being smaller than one and the value of μ_2 being smaller than the value of μ_1. In such a case, these identified parameters are sufficient for modeling, prediction, or control of this system around the range of the excitation frequency and amplitude considered during the identification.

Chapter 4

Identification of Nonlinear Structural Systems

In this chapter, system identification is performed for two mechanical systems. The first is a parametrically excited cantilevered beam. The second is a parametrically excited three-beam frame. Experiments are carried out to observe nontrivial steady-steady oscillations. Identification, based on the methodology outlined in Section 2.4.4 and tested in Chapter 3, is performed for each system using the experimental observations. Time-history comparisons are made between the experiment and analysis to validate the methodology and quantify the accuracy of the identified parameters.

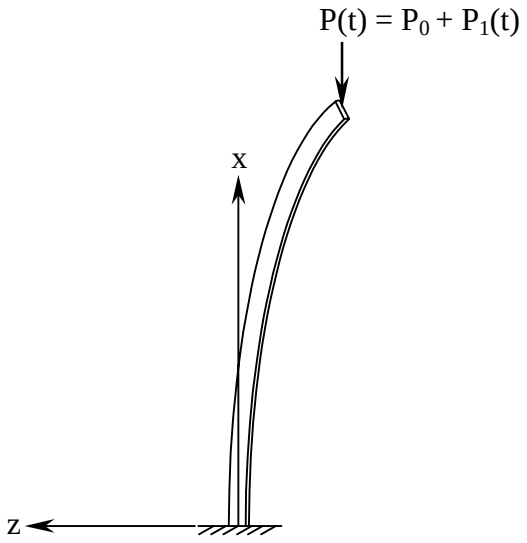

Figure 4.1: A fixed-free beam under axial load.

4.1 Experiment 1: Parametrically Excited Cantilevered Beam

4.1.1 Analytical Model

In this experiment, we consider a cantilevered beam of length l under an axial load $P(t)$, as shown in Fig. 4.1. For this axial load, the base axial load is P_0 and the time-varying axial load is $P_1(t)$. Following Nayfeh and Mook (1979), we model the response of the beam with the differential equation

$$\rho A \frac{\partial^2 w}{\partial t^2} + P(t) \frac{\partial^2 w}{\partial x^2} + EI \frac{\partial^4 w}{\partial x^4} = 0 \tag{4.1}$$

where w is the transverse displacement, ρ is the beam density, A is the cross-sectional area, E is Young's modulus, and I is the area moment of inertia about the z-axis. A series solution

to this differential equation is given by

$$w(x,t) = \sum_m u_m(t)\phi_m(x) \tag{4.2}$$

where ϕ_m are the eigenfunctions of

$$\phi^{iv} + p_0\phi'' - k_m^4\phi = 0 \tag{4.3}$$

where

$$p_0 = \frac{P_0}{EI} \tag{4.4}$$

$$k_m^4 = \frac{\rho A\omega_m^4}{EI} \tag{4.5}$$

with ω_m being the eigenvalue of the m-th mode of the beam. The appropriate boundary conditions for the setup shown in Fig. 4.1 are

$$\phi = \phi' = 0 \qquad \text{at} \qquad x = 0 \tag{4.6}$$

$$\phi'' = \phi''' = 0 \qquad \text{at} \qquad x = l \tag{4.7}$$

These boundary conditions correspond to a zero deflection and slope at the fixed end and zero moment and shear at the free end.

Substitution of this series solution into Eq. (4.1) yields

$$\sum_m (\ddot{u}_m + \omega_m^2 u_m)\phi_m + \frac{P_1(t)}{\rho A} u_m \phi_m'' = 0 \tag{4.8}$$

Exploiting the orthogonality properties of the ϕ_m, multiplying by ϕ_n, and integrating the results from $x = 0$ to $x = l$ yields

$$\ddot{u}_n + \omega_n^2 u_n + \frac{P_1(t)}{\rho A}\sum_m f_{nm}u_m = 0 \qquad \text{for n = 1, 2, 3, ..., N-2, N-1, N} \tag{4.9}$$

where

$$f_{nm} = \frac{\int_0^l \phi_n \phi_m'' dx}{\int_0^l \phi_n^2 dx} \tag{4.10}$$

When the excitation consists of a single frequency and does not activate any combination resonance, the modes will be uncoupled. For the first mode, we let $n = 1$ and $m = 1$, assume that $P_0 = 0$, drop the subscripts, and obtain

$$\ddot{u} + \omega^2 u + \frac{P(t)}{\rho A} \frac{\int_0^l \phi \phi'' dx}{\int_0^l \phi^2 dx} = 0 \tag{4.11}$$

If $P(t)$ is restricted to be harmonic of the form $P(t) = f\cos(\Omega t + \tau_f)$, where f, Ω, and τ_f are the excitation amplitude, frequency, and phase, respectively, Eq. (4.11) yields

$$\ddot{u} + \omega^2 u = \eta f u \cos(\Omega t + \tau_f) \tag{4.12}$$

where

$$\eta = -\frac{1}{\rho A} \frac{\int_0^l \phi \phi'' dx}{\int_0^l \phi^2 dx} \tag{4.13}$$

and η can be considered to be a forcing parameter for the beam. Equation (4.12) has the same form as the Mathieu equation considered in Section 2.1. Because of this similarity, we will model the more general problem of the parametrically forced fixed-free, or cantilevered, beam by

$$\begin{aligned} \frac{d^2u}{dt^2} + \omega^2 u + 2\mu_1 \frac{du}{dt} + \mu_2 \frac{du}{dt}\left|\frac{du}{dt}\right| \; + \; + \alpha_3 u^3 + \delta \left(\frac{du}{dt}\right)^2 u \\ = \eta f u \cos(\Omega t + \tau_e) \end{aligned} \tag{4.14}$$

Equation (4.14) accounts for linear and quadratic damping, geometric and inertial nonlinearities, and parametric excitation, all of which are frequently encountered in real systems

involving beams: the damping terms model viscous and form drag; the geometric nonlinearity terms model nonlinear stiffness; and the parametric excitation term models loads similar to $P(t)$, as shown in Fig. 4.1.

4.1.2 Experimental Setup and Results

A detailed description of the experimental setup is given by Oueini et al (1998). The assembly consists of a steel beam attached to a steel mounting plate. The width and thickness of the beam are 1.905 and 0.0825 cm, respectively. The length of the beam is 20.8 cm as measured between the top of the beam and the top of the mounting plate. The first natural frequency of the beam is 10.8 Hz, as measured from its free response. The excitation source is a modal shaker attached to the base of the mounting plate. The excitation is measured using an accelerometer mounted to the mounting plate. The response is measured using a single strain gage mounted approximately 2.54 cm above the mounting plate.

To exploit the principal parametric resonance in the beam, we set the frequency of the excitation at 21.7 Hz, which is near twice the first natural frequency of the beam. The amplitude of the acceleration of the excitation is varied between 1.46 and 2.04 V, where 1 Volt corresponds to approximately 9.81 m/s^2 of acceleration. The corresponding steady-state response amplitudes are 0.116 and 0.297 V, respectively. For the discussion of this experiment, the units for all of the parameters and measurements are considered to be normalized with Volts. In Fig. 4.2, we show the response amplitude as a function of the excitation amplitude. In Figs. 4.3 and 4.4, we show time histories of the extreme excitation

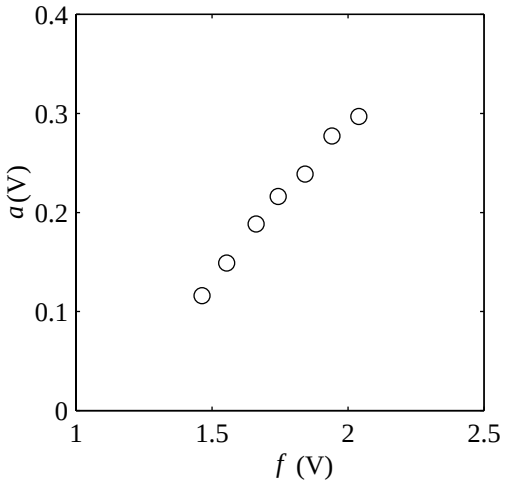

Figure 4.2: A force-response curve for the cantilevered beam experiment.

and response observed during the experiment.

4.1.3 Linear System Identification and Frequency-Domain Analysis

As described in Section 2.4.1, a free response of the beam was observed to identify the linear damping. The exponential decay measured from this free response yielded a value of $\mu_1 = 0.0703$ Hz.

For the following frequency-domain analysis, all of the spectral estimates are computed using 256 samples per segment. Segment averaging is employed to reduce the variance of these moments, and a Hanning window is used to reduce leakage. The time lag induced by the data acquisition system is removed when appropriate. In Fig. 4.5–4.6, we show plots of the power spectra of the extreme excitation and response measured during the experiment.

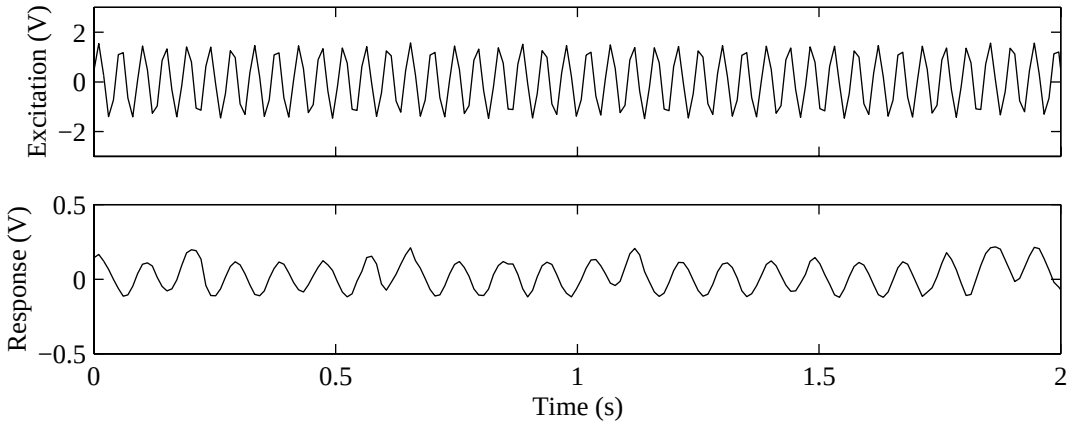

Figure 4.3: Time histories of the minimum excitation and response measured during the cantilevered beam experiment.

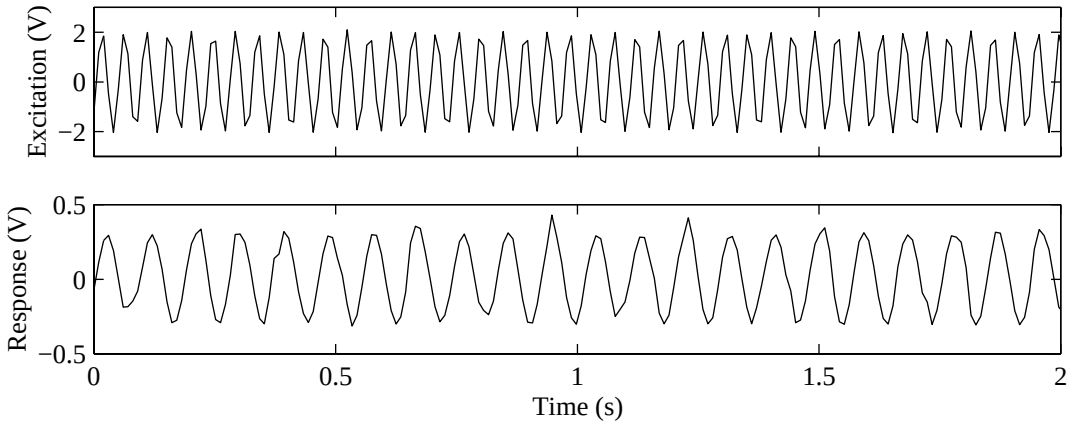

Figure 4.4: Time histories of the maximum excitation and response measured during the cantilevered beam experiments.

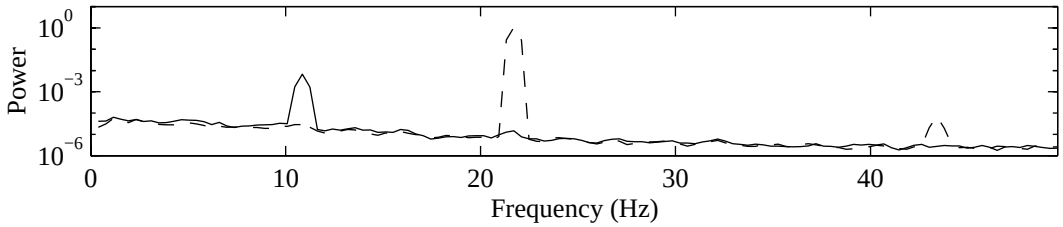

Figure 4.5: Power spectra of the minimum excitation (dashed) and response (solid) measured during the cantilevered beam experiment.

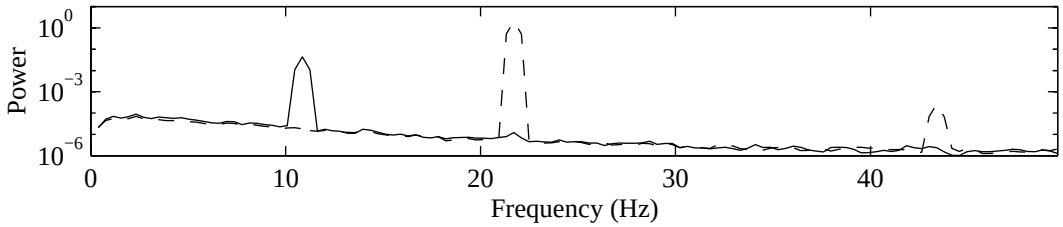

Figure 4.6: Power spectra of the maximum excitation (dashed) and response (solid) measured during the cantilevered beam experiment.

These spectra indicate a signal to noise ratio of at least 50 dB. The main frequency component in the excitation is observed to be at 21.7 Hz. Harmonics of the excitation signal are also present. The main frequency component in the response is observed to be at 10.85 Hz. Its harmonics are also present.

In Figs. 4.7 and 4.8, we show plots of the linear coherence between the extreme excitation and response observed during the experiment. The low level of linear coherence at 10.85 Hz indicates that the response at 10.85 Hz is not linearly related to an excitation component at 10.85 Hz. While nonzero, the peak at 21.7 Hz is not significantly high enough to indicate a direct interaction mechanism between the excitation and response at the excitation frequency. The response at 21.7 Hz is also extremely small, removing any significance of

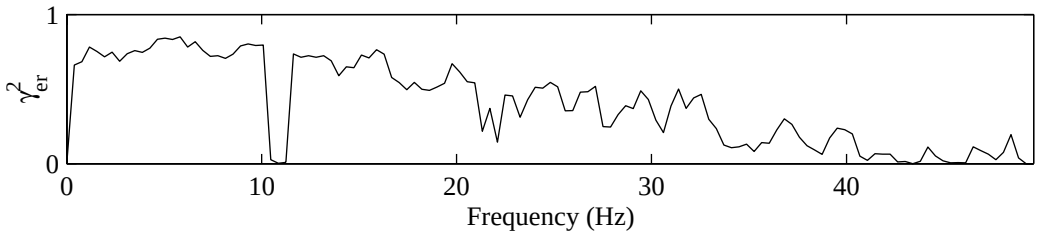

Figure 4.7: Linear coherence for the minimum excitation and response measured during the cantilevered beam experiment.

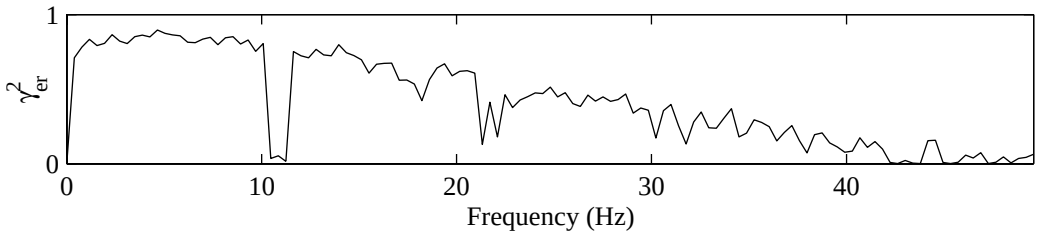

Figure 4.8: Linear coherence for the maximum excitation and response measured during the cantilevered beam experiment.

the linear coherence at that frequency. The other nonzero values of the linear coherence are also insignificant because there are no excitation or response components of importance at frequencies other than 10.85 or 21.7 Hz. In addition, errors in the linear coherence may arise from considering a finite number of segments.

In Figs. 4.9 and 4.10, we show plots of the cross-bicoherence between the extreme excitation and response observed during the experiment. High cross-bicoherence is measured between components with frequencies at (10.85 Hz, 10.85 Hz). This implies coupling between the frequency component of the excitation (21.7 Hz) with the frequency component of the response (10.85 Hz). Because high peaks are found in the cross-bicoherence between the excitation and response, the phase of the cross-bispectrum can be used as an estimate of the

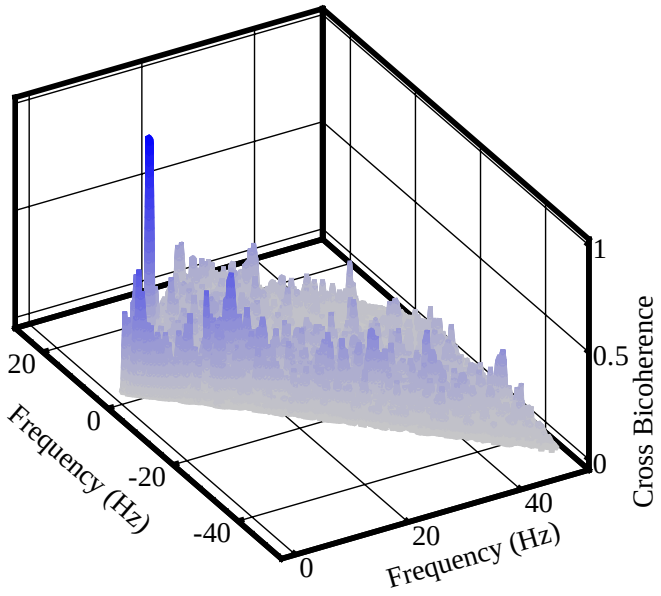

Figure 4.9: Cross-bicoherence between the minimum excitation and response measured during the cantilevered beam experiment.

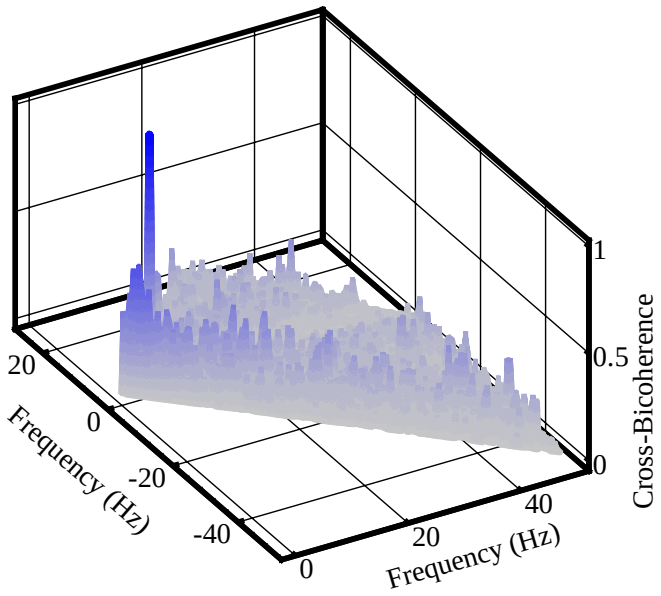

Figure 4.10: Cross-bicoherence between the maximum excitation and response measured during the cantilevered beam experiment.

Table 4.1: Summary of the frequency-domain analysis for the cantilevered beam experiment: $f_1 = \frac{1}{2}\Omega$ and $f_2 = \Omega$.

F	a_{f_1}	$\gamma^2_{xy}(f_1)$	$\gamma^2_{xy}(f_2)$	$b^2_{xxx}(f_1, f_1)$	$b^2_{yxx}(f_1, f_1)$	γ
V	V					deg
1.46	0.116	0.0036	0.371	0.331	0.978	99.8
1.55	0.149	0.0223	0.118	0.113	0.989	105.8
1.66	0.188	0.0030	0.454	0.447	0.995	109.9
1.74	0.216	0.0002	0.548	0.543	0.997	113.1
1.84	0.239	0.0107	0.350	0.353	0.996	115.5
1.94	0.277	0.0082	0.281	0.283	0.997	117.9
2.04	0.297	0.0529	0.413	0.416	0.996	120.6

nonlinear phase quantity γ. A summary of the results of the frequency-domain analysis is given in Table 4.1.3.

4.1.4 Nonlinear System Identification

Having measured f, a, and γ from time- and frequency-domain analyses, we proceed to nonlinear system identification based on the methodology outlined in Section 2.4.3. As shown in the previous chapter, the polynomial relationships between a and $f \sin\gamma$ and between a^2 and $f \cos\gamma$ will determine the types of damping and nonlinearities found in the system. These polynomial relationships also allow for direct nonlinear system parameter identification. Plots of a versus $f \sin\gamma$ and a^2 versus $f \cos\gamma$ are shown in Figs. 4.11–4.12. The results show that the relationship between a and $f \sin\gamma$ is linear. According to Section 2.4.3,

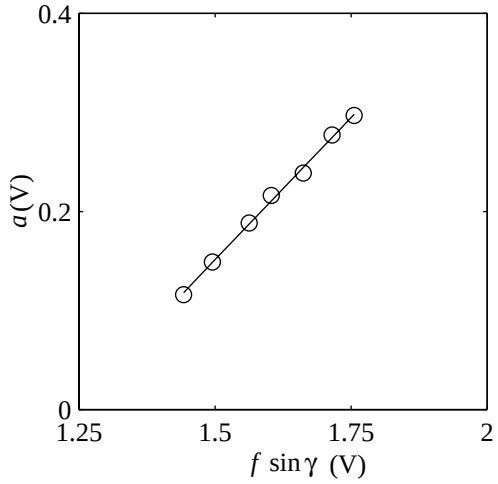

Figure 4.11: A plot of a versus $f \sin\gamma$ for the cantilevered beam experiment.

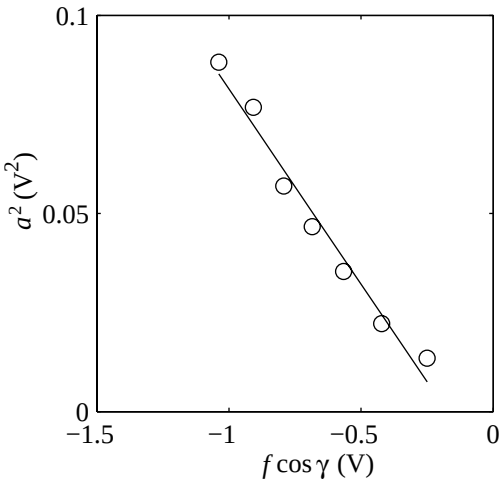

Figure 4.12: A plot of a^2 versus $f \cos\gamma$ for the cantilevered beam experiment.

Table 4.2: Identified parameters for the cantilevered beam experiment.

Parameter	Identified Value
ω	10.8151 Hz
α_e	-246
η_e	24.3
μ_1	0.0703
μ_2	0.0216

this linear relationship indicates the existence of both linear and quadratic damping; that is, linear damping alone is not enough to model the damping behavior of the beam. Moreover, the relationship between a^2 and $f\cos\gamma$ is also linear. According to Section 2.4.3, this linear relationship indicates the existence of geometric and inertial nonlinearities. Using a least-square curve fit, we obtain

$$a = 2598 f \sin\gamma - 665 \tag{4.15}$$

$$a^2 = 152950 f \cos\gamma - 7540 \tag{4.16}$$

These linear relationships are consistent with the steady-state amplitude and phase equations found in Eqs. (2.71) and (2.72). Using the coefficients obtained from these linear relationships, we performed nonlinear parameter identification according to Eqs. (2.75)–(2.78). A summary of the identified parameters is given in Table 4.2.

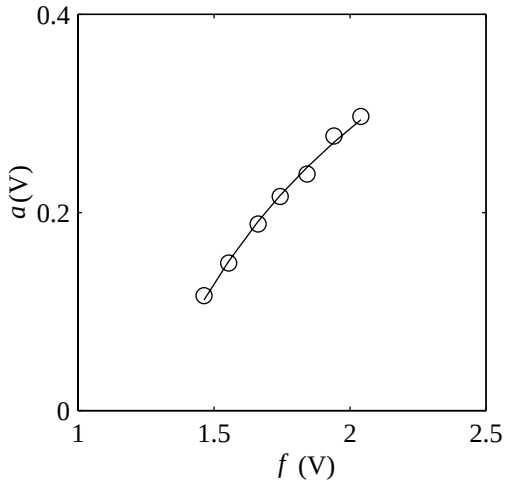

Figure 4.13: A comparison of the force response obtained experimentally (circles) and analytically (solid line) for the cantilevered beam.

4.1.5 Validation

To validate these parameters, we integrated Eq. (2.4) to numerically simulate the response due to excitation levels comparable to those used in the experiment. The integration time step was set at 0.000504 s. As a qualitative measure of the agreement between the mathematical model and the experimental observations, in Fig. 4.13 we compare the force-response curve predicted by the model to that observed during the experiment. In Figs. 4.14 and 4.15 we show a comparison of the extreme steady-state responses. The simulated steady-state responses and their corresponding errors from the experimental responses are given in Table 4.3. The mean error (absolute value) between experiment and response is 1.87%.

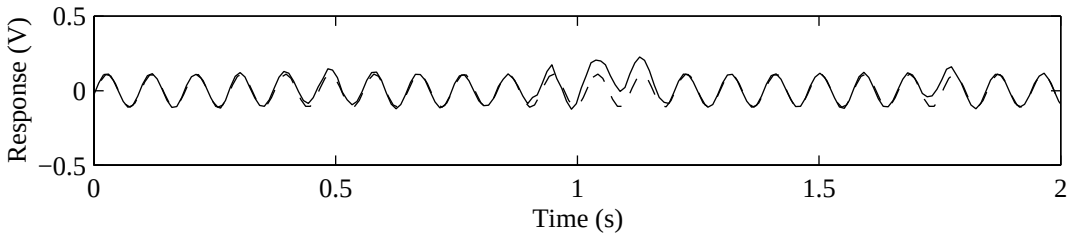

Figure 4.14: Comparison of the steady-state minimum response time-histories obtained experimentally (solid) and analytically (dashed) for the cantilevered beam.

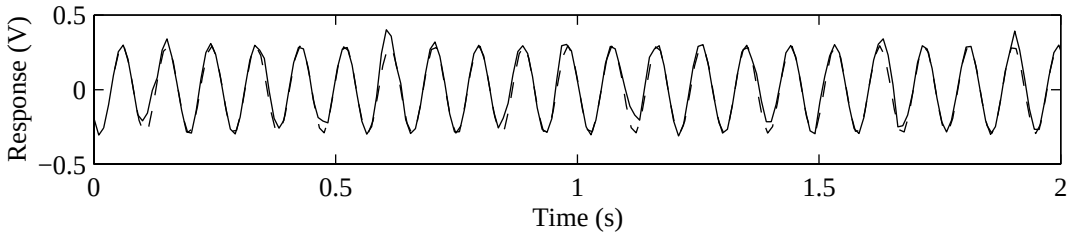

Figure 4.15: Comparison of the steady-state maximum response time-histories obtained experimentally (solid) and analytically (dashed) for the cantilevered beam.

Table 4.3: Experimental (exp) and simulation (sim) steady-state response amplitudes for the cantilevered beam.

F	a_{exp}	a_{sim}	$\lvert\%$ Error$\rvert$
V	V	V	
1.46	0.116	0.112	3.69
1.55	0.149	0.151	1.12
1.66	0.188	0.191	1.43
1.74	0.216	0.217	0.52
1.84	0.239	0.246	2.90
1.94	0.277	0.271	2.27
2.04	0.297	0.294	1.15

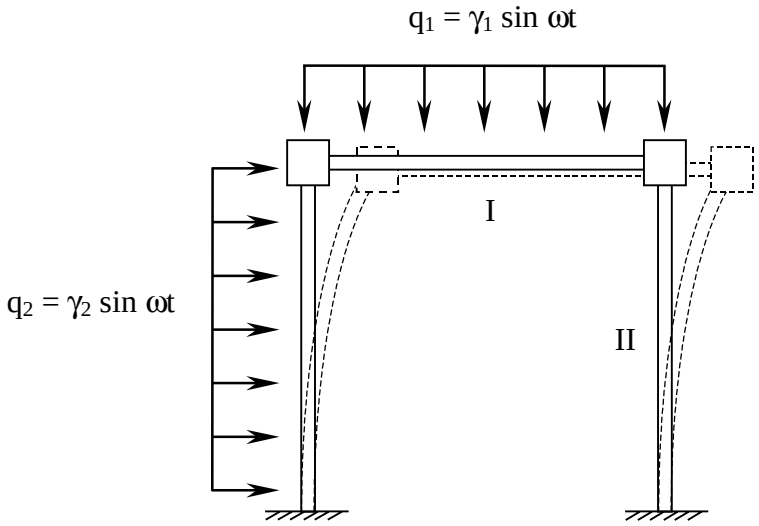

Figure 4.16: A three-beam frame under transverse loading.

4.2 Experiment 2: Parametrically Excited Three-Beam Frame

4.2.1 Analytical Model

A system of beams under a time-varying load presents an increased complexity of the dynamics in comparison to the single fixed-free beam studied in the previous section. In this part of our work, we consider a three-beam frame as shown in Fig. 4.16.

We will restrict our work to asymmetric responses resulting from parametric resonances. In particular, we consider asymmetric responses where the excitation is only applied transversely to the horizontal element I. The model to be used for the frame is based on the single-degree-of-freedom Duffing system of Eq. (2.3), which accounts for viscous and quadratic damping, geometric and inertial nonlinearities, and a parametric excitation.

Differences between the beam and frame geometries are reflected in their dynamics. One difference between the frame and the cantilevered beam is that quadratic nonlinearities, due to the unique geometry of the frame, influence the frame dynamics. Another difference is that because this system is more complex than the cantilevered beam, there is an increased potential for nonideal influences, such as a small direct excitation

4.2.2 Experimental Setup and Results

A detailed description of the experimental setup is given by Fahey and Nayfeh (1998). The frame consists of three steel beams attached to a base and two corner masses. The beams are made of steel and the masses and base are made of aluminum. The width and thickness of the beams are 1.905 and 0.0825 cm, respectively. The top beam is 24.1 cm long as measured between the corner masses. The side beams are 25.4 cm long as measured between the base and corner masses. Each corner mass is 0.131 kg. The first natural frequency of the frame is 3.595 Hz, as measured from its free response. The excitation source is a 250-lb shaker attached to the base of the frame. The excitation is measured using an accelerometer mounted to the base. The response is measured using a single strain gage mounted approximately 3.81 cm above the base on the outer side of one of the vertical beams.

Fahey and Nayfeh gave a detailed description of the response of the frame. For our identification procedure, we consider only the case where the excitation frequency is set at 7.16 Hz and its amplitude is varied between 0.43 and 1.08 m/s^2. The corresponding

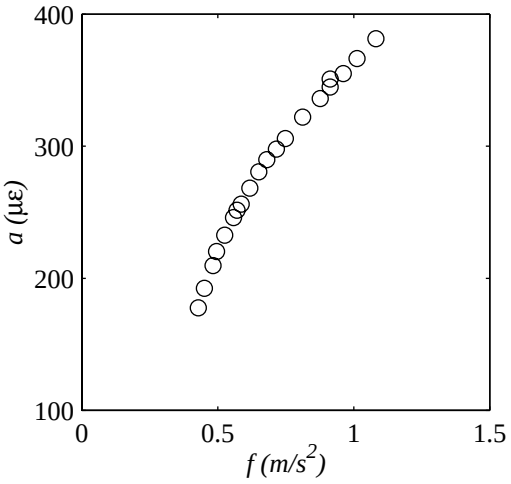

Figure 4.17: A force-response curve for the frame experiment.

steady-state response amplitudes are 177 and 380 $\mu\varepsilon$, respectively. In Fig. 4.17, we show the response amplitude as a function of the excitation amplitude. In Figs. 4.18 and 4.19, we show time histories of the extreme excitations and responses observed during these experiments.

4.2.3 Linear System Identification and Frequency-Domain Analysis

As described in Section 2.4.1, the exponential decay of a free response of the frame is used to identify its linear damping. The result is $\mu_1 = 0.0036$ Hz.

For the frequency-domain analysis, all of the spectral estimates are computed using 512 samples per segment. Segment averaging is employed to reduce the variance of these moments, and a Hanning window is used to reduce leakage. The time lag induced by the data acquisition system is removed when appropriate. In Fig. 4.20 and 4.21, we show the

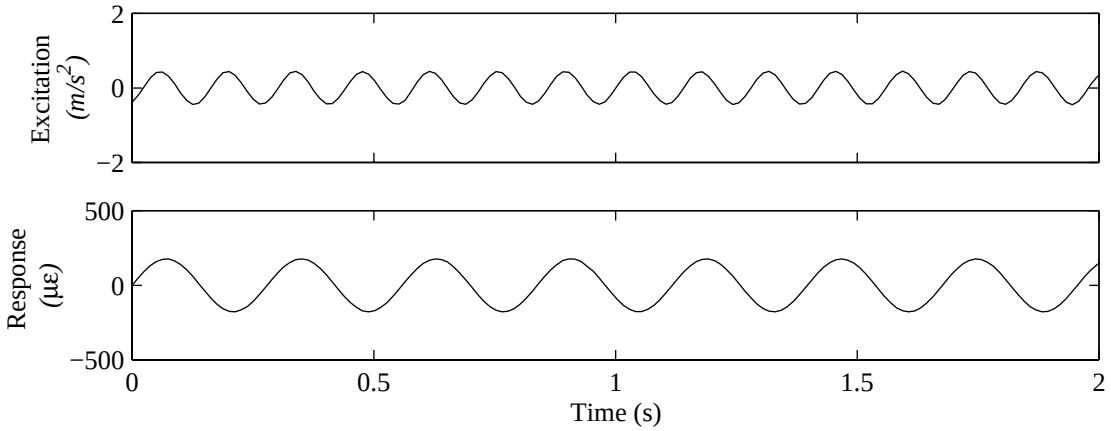

Figure 4.18: Time histories of the minimum excitation and response measured during the frame experiment.

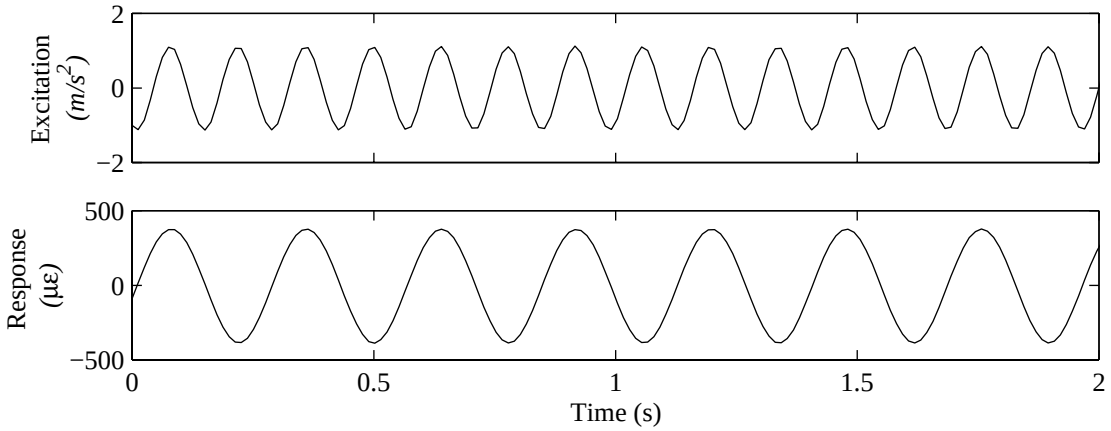

Figure 4.19: Time histories of the maximum excitation and response measured during the frame experiment.

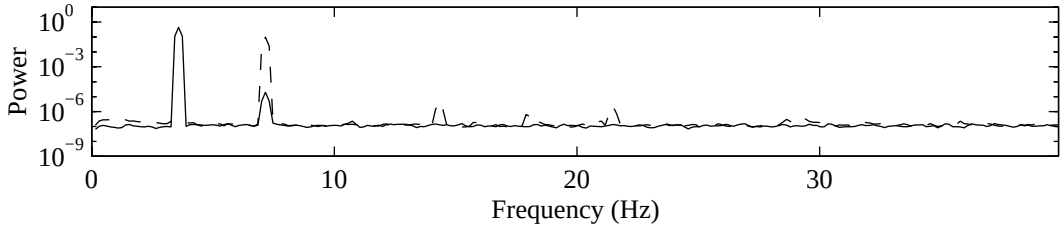

Figure 4.20: The power spectra for the minimum excitation (dashed) and response (solid) measured during the frame experiment.

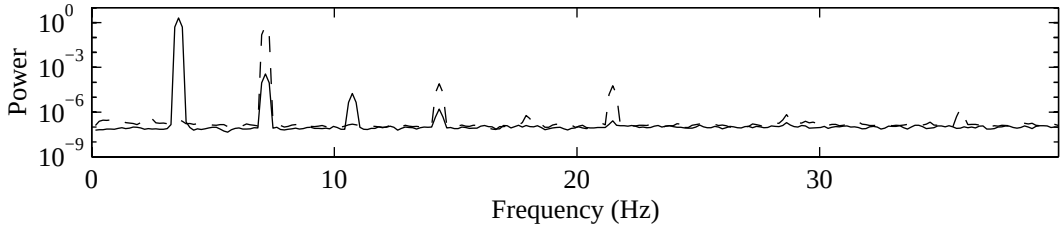

Figure 4.21: The power spectra for the maximum excitation (dashed) and response (solid) measured during the frame experiment.

power spectra of the extreme excitations and responses measured during the experiment. The spectra indicate a signal to noise ratio of at least 50 dB. In both cases, the main frequency component in the excitation is at 7.16 Hz. Harmonics of the excitation signal are also present. Also in both cases, the main frequency component in the response is observed to be at 3.58 Hz. Its harmonics are also present.

The linear coherence between the extreme excitations and responses is shown in Fig. 4.22 and 4.23. The high linear coherence at 7.16 Hz indicates a direct interaction mechanism between the excitation and response at the excitation frequency. The lower level of linear coherence at 3.58 Hz indicates that the response at 3.58 Hz is not linearly related to the frequency component in the excitation at 3.58 Hz.

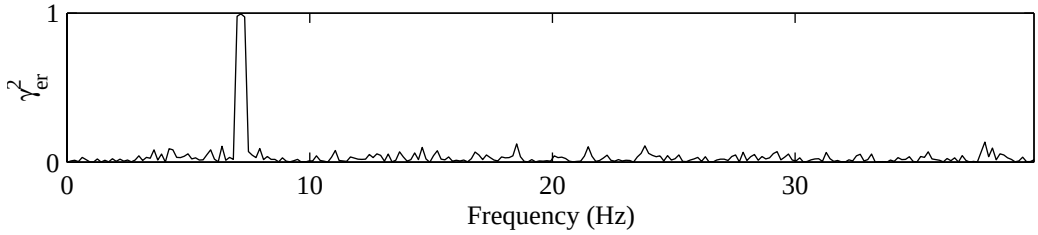

Figure 4.22: The linear coherence for the minimum excitation and response measured during the frame experiment.

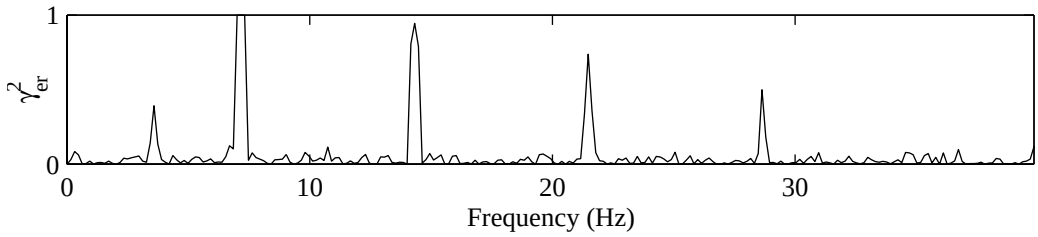

Figure 4.23: The linear coherence for the maximum excitation and response measured during the frame experiment.

The auto-bicoherence for the extreme responses is shown in Figs. 4.24 and 4.25. The high bicoherence measured between components with frequencies at $f_i = f_j = 3.58$ Hz indicates coupling in the response between the 3.58 Hz component and the $f_i + f_j = 7.16$ Hz component. Note also the other peaks in the auto-bicoherence spectrum, especially in the maximum response case, which indicate phase coherence and coupling amongst the harmonics.

The possible phase coupling between the response harmonics and the low linear coherence at 3.58 Hz indicates that the excitation and response are nonlinearly related. This also shows that nonlinear phase relations between the excitation and response may be detected

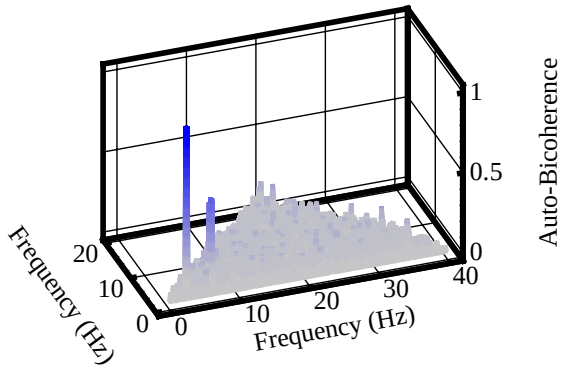

Figure 4.24: The auto-bicoherence for the minimum response measured during the frame experiment.

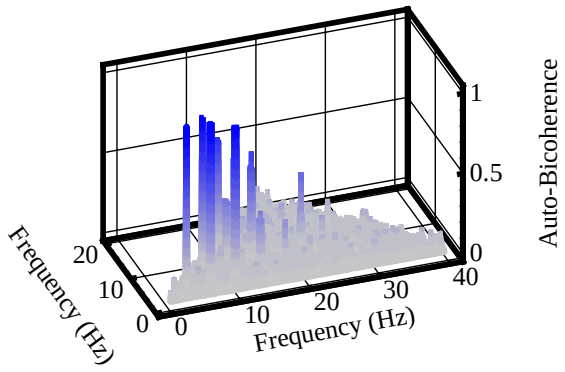

Figure 4.25: The auto-bicoherence for the maximum response measured during the frame experiment.

by computing their cross-bispectrum. This phase relation, which would be of the form

$$\gamma = \tau_e(\Omega) - 2\tau_r(\frac{1}{2}\Omega) \tag{4.17}$$

as previously defined in Eq. (2.65), would then be calculated from the cross-bispectrum according to

$$\gamma = \angle B_{err}(\frac{1}{2}\Omega, \frac{1}{2}\Omega) \tag{4.18}$$

as previously defined in Eq. (2.66). This phase relation can also be written in the form

$$\gamma = [\tau_e(\Omega) - \tau_r(\Omega)] + [\tau_r(\Omega) - 2\tau_r(\frac{1}{2}\Omega)] \tag{4.19}$$

as previously defined in Eq. (2.67). Furthermore, this phase quantity can be calculated with the cross-power spectrum and the response auto-bispectrum according to

$$\gamma = \angle P_{er}(\Omega) + \angle B_{rrr}(\frac{1}{2}\Omega, \frac{1}{2}\Omega) \tag{4.20}$$

as previously defined in Eq. (2.68). Note that the phase quantity γ is the same whether computed from either Eq. (4.18) or Eq. (4.20). For this reason, we will avoid computing the cross-bispectrum and instead use the existing data provided by the cross-power spectrum and the response auto-bispectrum and compute γ according to Eq. (4.20). A summary of the frequency-domain analysis is listed in Table 4.4.

4.2.4 Nonlinear System Identification

Following the methodology outlined in Section 2.4.3, the polynomial relationships between a and $f\sin\gamma$ and between a^2 and $f\cos\gamma$ are used to determine the types of nonlinearities

Table 4.4: Summary of the frequency-domain analysis for the frame experiment: $f_1 = \frac{1}{2}\Omega$ and $f_2 = \Omega$.

f	a_{f_1}	a_{f_2}	$\gamma^2_{xy}(f_1)$	$\gamma^2_{xy}(f_2)$	$b^2(f_1, f_1)$	γ
m/s^2	$\mu\varepsilon$					deg
0.432	178	1.17	0.083	0.994	0.994	48.2
0.453	192	1.30	0.135	0.996	0.996	45.7
0.486	210	1.43	0.086	0.996	0.996	44.3
0.500	220	1.58	0.230	0.997	0.997	43.3
0.530	233	1.71	0.262	0.997	0.997	41.0
0.562	246	1.86	0.192	0.995	0.994	40.1
0.576	252	1.95	0.402	0.998	0.998	37.6
0.591	256	2.04	0.278	0.998	0.998	37.2
0.623	268	2.19	0.331	0.998	0.998	35.4
0.656	281	2.40	0.451	0.998	0.998	33.9
0.687	290	2.58	0.395	0.998	0.998	32.6
0.722	298	2.79	0.416	0.998	0.998	30.9
0.755	306	2.96	0.520	0.999	0.999	29.7
0.819	322	3.36	0.479	0.999	0.999	27.5
0.884	336	3.76	0.444	0.998	0.999	26.2
0.920	351	4.13	0.400	0.992	0.998	25.6
0.920	345	4.02	0.449	0.999	0.999	24.9
0.970	355	4.32	0.414	0.999	0.999	23.5
1.020	366	4.64	0.516	0.999	0.999	22.6
1.089	381	5.10	0.392	0.999	0.999	21.4

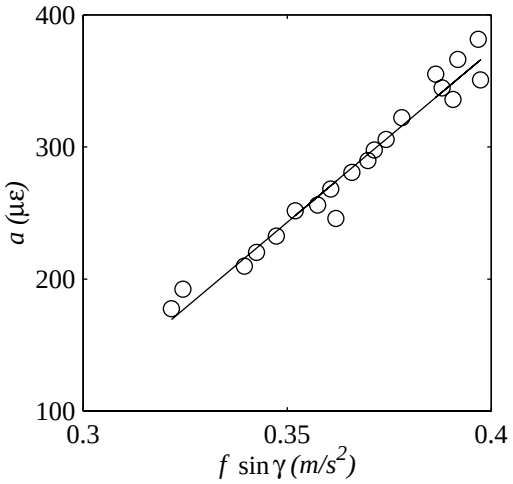

Figure 4.26: A plot of a versus $f \sin\gamma$ for the frame experiment.

found in the system. These polynomial relationships also allow for direct nonlinear parameter identification. Plots of a versus $f \sin\gamma$ and a^2 versus $f \cos\gamma$ are shown in Figs. 4.26 and 4.27.

It is obvious that the relation between a and $f \sin\gamma$ is linear. According to Section 2.4.3, this linear relationship indicates the existence of both linear and quadratic damping. The relation between a^2 and $f \cos\gamma$ is also linear, which indicates the existence of geometric or inertial nonlinearities. Using a least-square curve fit, we find that

$$a = 2598 f \sin\gamma - 665 \tag{4.21}$$

$$a^2 = 152950 f \cos\gamma - 7540 \tag{4.22}$$

These linear relationships are consistent with the steady-state amplitude and phase relationships found in Eqs. (2.71) and (2.72). Nonlinear parameter identification is then performed according to Eqs. (2.75)–(2.78), which yields

$$\alpha_e = 1.30 \times 10^{-05}\ \mu\varepsilon^{-2}\, s^2 \tag{4.23}$$

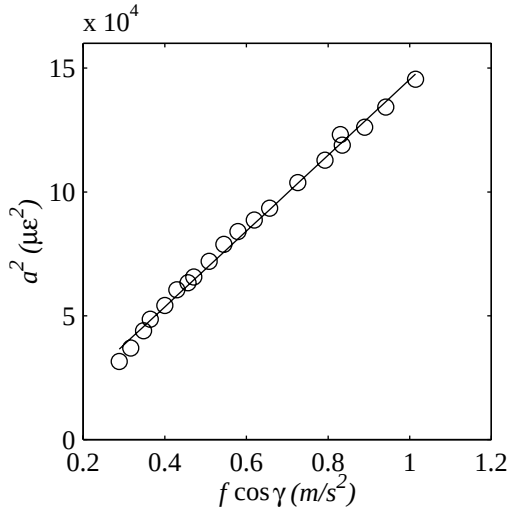

Figure 4.27: A plot of a^2 versus $f\cos\gamma$ for the frame experiment.

$$\eta_e = 1.99 \ \text{m}^{-1} \tag{4.24}$$

$$\mu_2 = 3.36 \times 10^{-06} \ \mu\varepsilon^{-1} \tag{4.25}$$

$$\omega = 3.5807 \,\text{Hz} \tag{4.26}$$

Because of the frequency component in the response at the excitation frequency, the effective geometric nonlinearity and effective forcing parameters can be broken down into their individual nonlinearity and forcing parameters. To this end, we observe that the approximate solution given in Eq. (2.39) can be separated into frequency components: a mean component given by

$$u_a = -\frac{\epsilon\alpha_2}{2\omega^2}a^2 \tag{4.27}$$

a response at the frequency $\frac{1}{2}\Omega = 3.58$ Hz given by

$$u_b e^{i(\frac{1}{2}\Omega t+\tau_b)} = \frac{1}{2}ae^{\frac{1}{2}i(\Omega t+\tau_e-\gamma)} \tag{4.28}$$

and a response at the frequency $\Omega = 7.16$ Hz given by

$$u_c e^{i(\Omega t+\tau_c)} = \frac{\epsilon\alpha_2}{12\omega_0^2} a^2 e^{i(\Omega t+\tau_e-\gamma)} - \frac{\epsilon\eta_1}{6\omega_0^2} F e^{i(\Omega t+\tau_e)} \tag{4.29}$$

In these expressions, u_a is the amplitude of the d. c. component in the response, and u_b and u_c represent the response amplitudes at the frequencies $\frac{1}{2}\Omega$ and Ω Hz, respectively, and τ_b and τ_c are the corresponding phases at $\frac{1}{2}\Omega$ and Ω Hz, respectively. Equation (4.29) can then be used to determine α_2 and η_1. Dividing Eq. (4.29) by $e^{i\Omega t}$ yields

$$u_c e^{i\tau_c} = \frac{\epsilon\alpha_2}{12\omega_0^2} a^2 e^{i(\tau_e-\gamma)} - \frac{\epsilon\eta_1}{6\omega_0^2} F e^{i(\tau_e)} \tag{4.30}$$

which can be simplified into

$$u_c e^{i(\tau_c-\tau_e)} = \frac{\epsilon\alpha_2}{12\omega_0^2} a^2 e^{-i\gamma} - \frac{\epsilon\eta_1}{6\omega_0^2} F \tag{4.31}$$

which, in turn, can be separated into real and imaginary components as

$$u_c \cos(\tau_e - \tau_c) = \frac{\epsilon\alpha_2}{12\omega_0^2} a^2 \cos\gamma - \frac{\epsilon\eta_1}{6\omega_0^2} F \tag{4.32}$$

$$u_c \sin(\tau_e - \tau_c) = \frac{\epsilon\alpha_2}{12\omega_0^2} a^2 \sin\gamma \tag{4.33}$$

We note that u_c is the Fourier amplitude of the response at the excitation frequency. Also, $\tau_e - \tau_c$ is the phase of the cross-power spectrum at the excitation frequency. Therefore, Eqs. (4.32) and (4.33) can be used to compute α_2 and η_1 at each response amplitude and its corresponding excitation. These parameters are then given by

$$\alpha_2 = 12\omega_0^2 \frac{u_c}{a^2} \frac{\sin(\tau_e - \tau_c)}{\sin\gamma} \tag{4.34}$$

$$\eta_1 = \frac{6\omega_0^2}{F}\left[\frac{\alpha_2 a^2 \cos\gamma}{12\omega_0^2} - u_c \cos(\tau_e - \tau_c)\right] \tag{4.35}$$

Equations (2.32) and (2.33) can then be used to solve for $\frac{3}{8}\alpha_3 + \frac{1}{8}\delta\omega_0^2$ and η_2. The result is

$$\eta_2 = 4(\eta_e - \frac{\alpha_2\eta_1}{6\omega_0^2}) \tag{4.36}$$

$$\frac{3}{8}\alpha_3 + \frac{1}{8}\delta\omega_0^2 = \alpha_e + \frac{5}{12\omega_0^2}\alpha_2^2 \tag{4.37}$$

Table 4.5 contains a summary of these results and their averages. The relative differences between η_1 and η_2 reflect the dominance of the parametric mechanism over the direct mechanism. The large variation in η_1 indicate that the model is insensitive to this parameter. Recall that this parameter governs the direct interaction mechanism between the excitation and the response. Since the primary component of the response is at half the excitation frequency, as observed in Figs. 4.20 and 4.21 and Table 4.4, the parametric interaction mechanism dominates the dynamics. So the variation in η_1 may be attributed to the relative insignificance of the direct interaction mechanism in comparison with the parametric interaction mechanism. This shows that the parametric identification proceduce can also be used to characterize the dominant nonlinear mechanisms in a system.

4.2.5 Validation

To validate the identified parameters, we used them and integrated Eq. (2.4) numerically to determine the response due to excitation levels comparable to those used in the experiment. The integration time step was set at 0.627 ms. As a qualitative measure of the agreement between the mathematical model and the experimental observations, in Fig. 4.28 we compare the force-response curve predicted by the model simulations to that observed during the experiment. In Figs. 4.29 and 4.30 we show a comparison of the extreme steady-state

Table 4.5: Identified forcing and nonlinear parameters for the frame experiment.

F	$\tau_e - \tau_c$	η_1	η_2	α_2	$\frac{3}{8}\alpha_3 + \frac{1}{8}\delta\omega_0^2$
m/s^2	deg	$\mu\varepsilon\, m^{-1}$	m^{-1}	$\mu\varepsilon^{-1} s^{-2}$	$\mu\varepsilon^{-2} s^{-2}$
0.432	208	3811	8.65	-0.142	0.0000296
0.453	207	3808	8.63	-0.138	0.0000286
0.486	209	3350	8.54	-0.137	0.0000285
0.500	209	3539	8.58	-0.139	0.0000288
0.530	208	3338	8.54	-0.138	0.0000286
0.562	208	3138	8.51	-0.138	0.0000287
0.576	207	2975	8.49	-0.141	0.0000293
0.591	207	3121	8.52	-0.141	0.0000294
0.623	207	2846	8.47	-0.143	0.0000298
0.656	206	2611	8.44	-0.148	0.0000309
0.687	206	2420	8.42	-0.152	0.0000320
0.722	205	2191	8.40	-0.160	0.0000340
0.755	205	1964	8.36	-0.164	0.0000351
0.819	204	1579	8.30	-0.174	0.0000379
0.884	204	1212	8.23	-0.185	0.0000412
0.920	204	881	8.16	-0.192	0.0000433
0.920	203	907	8.17	-0.192	0.0000434
0.970	203	524	8.08	-0.201	0.0000461
1.020	202	363	8.04	-0.205	0.0000475
1.089	201	14	7.94	-0.213	0.0000502
avg		2230	8.37	-0.162	0.0000351

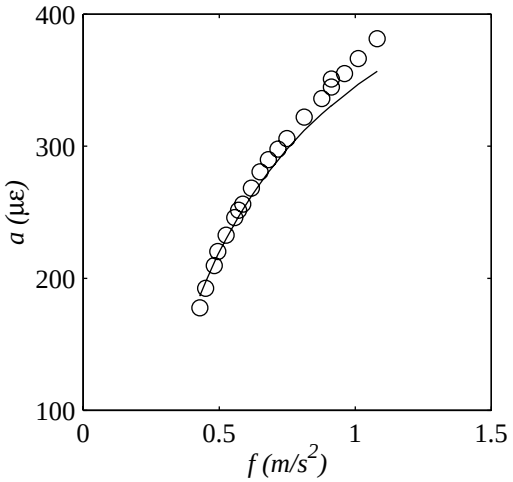

Figure 4.28: A comparison of the force response obtained experimentally (circles) and analytically (solid line) for the frame.

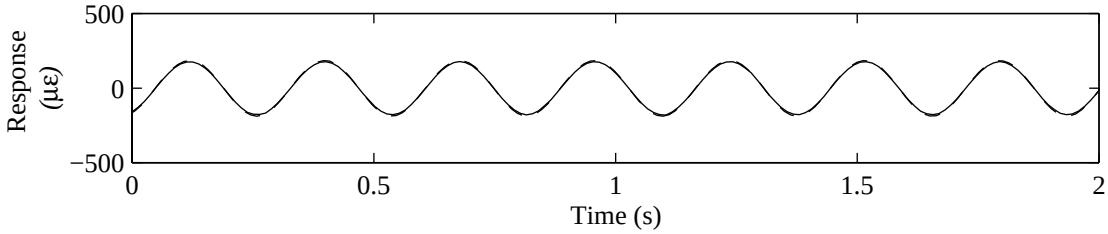

Figure 4.29: A comparison of the steady-state minimum response time-histories obtained experimentally (solid) and analytically (dashed) for the frame.

responses. The experimentally obtained amplitudes for a range of excitations, the simulated steady-state amplitudes, and the corresponding errors are given in Table 4.6. The mean error (absolute) between experiment and response is 3.17%.

Table 4.6: Experimental (exp) and simulation (sim) steady-state response amplitudes for the frame.

F	a_{exp}	a_{sim}	|% Error|
m/s^2	$\mu\varepsilon$	$\mu\varepsilon$	
0.432	178	187	5.04
0.453	192	197	2.61
0.486	210	212	1.18
0.500	220	218	1.01
0.530	233	230	1.14
0.562	246	242	1.73
0.576	252	247	1.97
0.591	256	252	1.68
0.623	268	262	2.32
0.656	281	272	3.21
0.687	290	280	3.27
0.722	298	289	2.82
0.755	306	298	2.62
0.819	322	312	3.14
0.884	336	324	3.45
0.920	351	331	5.69
0.920	345	331	4.12
0.970	355	339	4.66
1.020	366	347	5.30
1.089	381	357	6.49

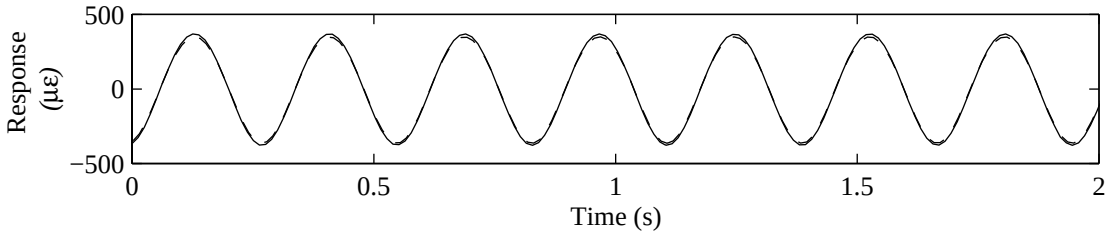

Figure 4.30: A comparison of steady-state maximum response time-histories between experiment (solid) and analysis (dashed) for the cantilevered frame.

Chapter 5

Identification of Ship Roll Instabilities

It has been well documented that nonlinear resonance conditions between heave, pitch, and roll motions could lead to large roll responses in a ship (Nayfeh, 1988; Oh et al, 1993). These roll motions can impede onboard operations and even cause capsizing. To reduce or prevent the effects of these motions, one needs prediction and control schemes. Such schemes can only be effective if the relevant mechanisms are correctly modeled. Because these mechanisms are primarily nonlinear, such models need to accurately describe the nonlinear resonances between the heave, pitch, and roll motions. Consequently, any system identification process must be able to quantify such resonances.

In this work, we outline a methodology for the identification of a roll instability in a series S60-70 ship. The roll instability is modeled with a three-degree-of-freedom system, which introduces complexities not encountered in studying the single-degree-of-freedom mechanical systems studied in Chapter 4. The added complexity results in modifications to our identification process. However, the method of multiple scales and bispectral analysis

are still combined for identification, which is taken from linear to nonlinear parameter estimation, as performed in previous chapters. In Section 5.1 we discuss how roll instabilities can result from either autoparametric resonances or parametric resonances. We present the governing equation for the parametric mechanism and an approximate solution based on the method of multiple scales. In Section 5.2, we discuss the numerical simulations conducted, using the LAMP (Large Amplitude Motions Program) software developed by the Scientific Applications International Corporation (SAIC, 1997), to study the parametric mechanism. In Section 5.3, we identify the linear parameters governing this system. In Section 5.4, we adopt a slightly modified version of the methodology presented in Chapter 2 for identification of the nonlinear parameters. Finally, we compare simulations computed using the identified parameters with the results computed using LAMP.

5.1 Two Mechanisms for Roll Instabilities

Nayfeh et al (1973), Mook et al (1974), Nayfeh (1988), and Oh et al (1993) used the method of multiple scales to determine the steady-state responses and stability of ships under different wave excitations and heave, pitch, and roll coupling conditions. The results of these studies show that there are many resonance conditions under which the roll response can grow to significantly large amplitudes. These roll instabilities can be produced by different mechanisms. In one mechanism, considered by Nayfeh et al (1973) and Mook et al (1974), the encounter wave frequency is near the pitch natural frequency. The pitch natural frequency, in turn, is near twice the roll natural frequency. Under these conditions, there is an

autoparametric resonance between the two modes. In the second mechanism, considered by Oh et al (1993), three degrees of freedom were taken into consideration. In this case, the encounter wave frequency is near twice the roll natural frequency, but the heave and pitch natural frequencies are away from twice the roll natural frequency. Under these conditions, there is no autoparametric resonance between the heave, pitch, and roll modes. Instead, the heave and pitch motions, excited linearly at the encounter wave frequency, produce a princpal parametric resonance in the roll. However, the roll motion does not influence either the heave or pitch motions. We should note here that the parametric resonance might be more relevant to practical situations. In this work, we study the parametric mechanism only.

The equations of motion governing the parametric resonance mechanism (Oh, 1993) are

$$\ddot{z} + 2\mu_z \dot{z} + \omega_z^2 = Z(t) \tag{5.1}$$

$$\ddot{\theta} + 2\mu_\theta \dot{\theta} + \omega_\theta^2 = \Theta(t) \tag{5.2}$$

$$\ddot{\phi} + 2\mu_\phi \dot{\phi} + \omega_\phi^2 = \frac{1}{2}(K_{\phi z}\phi z + K_{\phi\theta}\phi\theta + K_{\dot{\phi}\dot{z}}\dot{\phi}\dot{z} + K_{\dot{\phi}\dot{\theta}}\dot{\phi}\dot{\theta}) + \Phi(t) \tag{5.3}$$

where z, θ, and ϕ are, respectively, the heave, pitch, and roll coordinates; the μ_i are the linear damping parameters; the ω_i are the natural frequencies; the K_i are quadratic coupling coeffients; and Z, Θ, and Φ are the respective influence of the encounter wave on the three modes. For head seas, which is the case considered here, $\Phi(t)$ is zero. For harmonic wave excitations, the heave and pitch modes are linearly excited by the wave, and their respective motions are given by

$$z = a_z \cos(\Omega_t + \tau_z) \tag{5.4}$$

$$\theta = a_\theta \cos(\Omega_t + \tau_\theta) \tag{5.5}$$

Substituting Eqs. (5.4) and (5.5) into Eq. (5.3) yields the roll equation of motion

$$\begin{aligned}\ddot{\phi} + \omega_\phi^2 \phi = &-2\mu_\phi \dot{\phi} + [\frac{1}{2} a_z K_{\phi z} \cos(\Omega t + \tau_z) + + \frac{1}{2} a_\theta K_{\phi\theta} \cos(\Omega t + \tau_\phi)]\phi \\ &-[\frac{1}{2}\Omega a_z K_{\dot{\phi}\dot{z}} \sin(\Omega t + \tau_z) + \frac{1}{2}\Omega a_\theta K_{\dot{\phi}\dot{\theta}} \sin(\Omega t + \tau_\phi)]\dot{\phi}\end{aligned} \tag{5.6}$$

where a_z and a_θ are the heave and pitch response amplitudes, respectively; τ_z and τ_θ are the respective phase lags between either the heave or pitch motion and the wave excitation; and Ω is the wave encounter frequency. The coefficients of the nonlinear terms can be derived from the moments produced by static coupling and kinematic coupling between the heave or pitch motion and the roll motion given on the right-hand side of Eq. (5.3).

Oh et al (1993) used the method of multiple scales (Nayfeh, 1981; Nayfeh and Mook, 1979) to obtain an approximate first-order closed-form solution for Eq. (5.6). This solution is given by

$$\phi(t) = a_\phi \cos(\omega_\phi + \beta) + (\text{higher order terms}) \tag{5.7}$$

where the amplitude a_ϕ and phase β of the roll response are given by

$$\dot{a_\phi} = -\mu_\phi a_\phi - \frac{|c_z| a_\phi}{2\omega_\phi} \sin\gamma_z - \frac{|c_\theta| a_\phi}{2\omega_\phi} \sin\gamma_\theta \tag{5.8}$$

$$\dot{\gamma_z} + \dot{\gamma_\theta} = \sigma - \frac{|c_z|}{\omega_\phi} \cos\gamma_z - \frac{|c_\theta|}{\omega_\phi} \cos\gamma_\theta \tag{5.9}$$

and

$$\Omega = 2\omega_\phi + \sigma \tag{5.10}$$

$$c_z = -a_z \frac{1}{4}(K_{\phi z} - \omega_\phi \Omega K_{\dot{\phi}\dot{z}}) e^{i\tau_z}$$

$$= |c_z| e^{i\tau_z} \tag{5.11}$$

$$c_\theta = -a_\theta \frac{1}{4}(K_{\phi\theta} - \omega_\phi \Omega K_{\dot{\phi}\dot{\theta}}) e^{i\tau_\theta}$$

$$= |c_\theta| e^{i\tau_\theta} \tag{5.12}$$

$$\gamma_z = \sigma t + \tau_z - 2\beta \tag{5.13}$$

$$\gamma_\theta = \sigma t + \tau_\theta - 2\beta \tag{5.14}$$

Equation (5.10) is the resonance condition whereby the encounter frequency is approximately twice the roll natural frequency and σ is a frequency detuning parameter. The phase quantities γ_z and γ_θ in Eqs. (5.8) and (5.9) represent, respectively, the difference between the phase of the heave and pitch and twice the phase of the roll response, as given in Eqs. (5.13) and (5.14). Furthermore, the parameters modeling the coupling between the heave and pitch motions and the roll motion can be combined into effective parameters c_z and c_θ, which can be expressed in terms of the amplitudes $|c_z|$ and $|c_\theta|$ and phases τ_z and τ_θ, as in Eqs. (5.11) and (5.12). The approximate solution for ϕ can then be expressed as

$$\phi(t) \approx a_\phi \cos[\frac{1}{2}[\Omega t - \frac{1}{2}(\gamma_z + \gamma_\theta - \tau_z - \tau_\theta)]] \tag{5.15}$$

and the steady-state response is obtained by setting $\dot{a_\phi}$ and $\dot{\gamma}$ equal to zero.

5.2 Numerical Simulations

Numerical simulations were conducted using LAMP. This code simulates the full nonlinear response of a ship under a multitude of various sea conditions. A detailed description of this code is given by SAIC (1997). A dynamic supervisor, developed at Virginia Tech, is

incorporated into the code to allow for large-time steps and prevent numerical divergence of the simulation. The model used in these simulations is an S60-70 series ship, and only head seas were considered. Unless otherwise stated, all of the values reported here are nondimensional. The length scale L is the length of the ship, and the time scale is $\sqrt{L/g}$, where g is the gravitational acceleration. The simulation time step was fixed at 0.08.

5.3 Identification of Linear Parameters

To determine the damping and the natural frequency of the ship roll response, we used LAMP to simulate the roll free response. During this simulation, the ship floated in a wave-free environment with no forward velocity. The ship was initially deflected in roll to 0.1 degrees. Figure 5.1 shows a representative free response of the ship in roll. The roll damped frequency

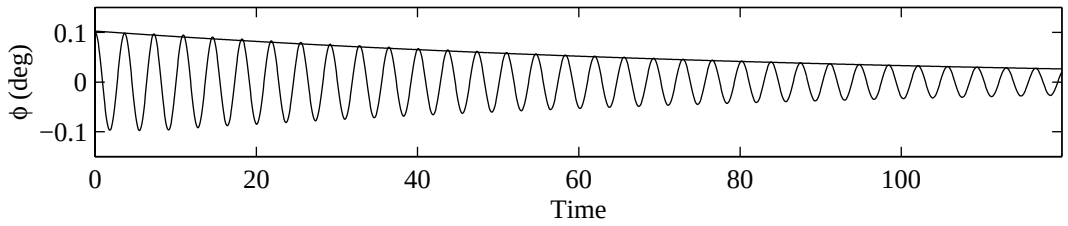

Figure 5.1: Time history of the roll free response of the ship simulation. Above the free-response curve is a curve defining the envelope of the response.

$\omega_{\phi d}$ was determined to be 0.2742 from measuring zero-crossings of the free response. The linear damping coefficient μ_ϕ was determined from the log decrement to be equal to 0.011. Given that the roll damped frequency $\omega_{\phi d}$, the roll natural frequency ω_ϕ and the roll damping ratio ζ_ϕ are related by $\omega_{\phi d} = \omega_\phi \sqrt{1 - \zeta_\phi^2}$, the roll damping ratio is found to be $\zeta_\phi \approx 0.042$

and the roll natural frequency is $\omega_\phi \approx 0.2744$.

Because the pitch and heave modes are linearly coupled, we identified their linear parameters from frequency-response functions. To this end, we conducted LAMP simulations at different wave excitation frequencies. Frequency responses were then determined for the ship in heave and pitch. During this series of simulations, the ship traveled with a forward velocity of 0.2 in head-sea waves having an amplitude of 0.0005 with varying encounter frequency. Figure 5.2 shows representative steady-state time-histories of the forced response of the ship in heave and pitch.

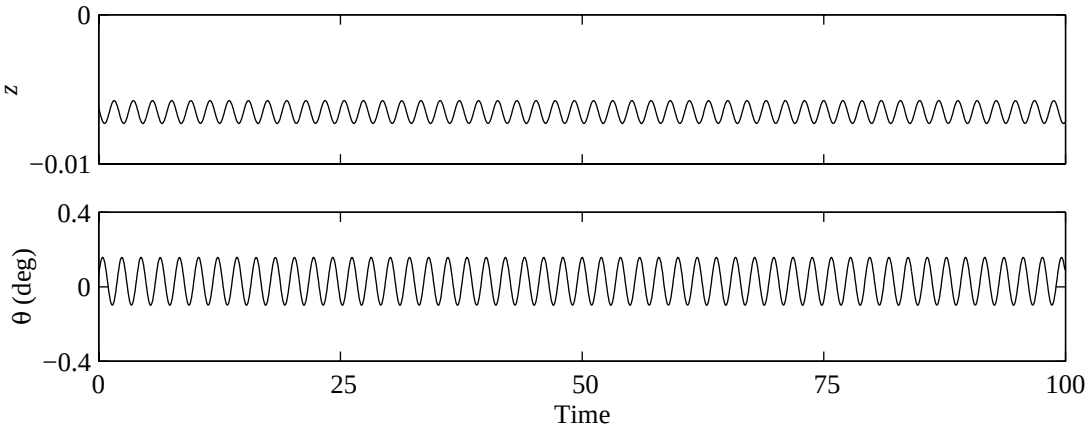

Figure 5.2: Representative forced response of the ship in heave and pitch. Wave amplitude is 0.0005; wave frequency is 0.5066.

Figure 5.3 shows the steady-state heave and pitch responses as a function of the wave excitation frequency. The peak in the heave response occurs at the heave resonant frequency; the peaks in the pitch response occur at the heave and pitch resonant frequencies. The two peaks that appear in the pitch response might be a product of coupling between the heave and pitch responses. For linear systems, the resonant frequency ω_r and peak M_r are given

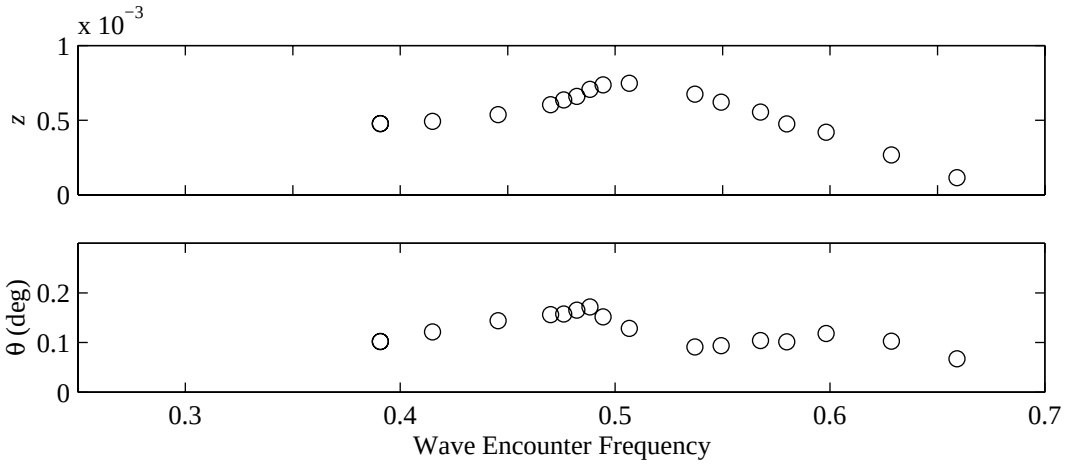

Figure 5.3: Steady-state heave and pitch responses vs wave encounter frequency. Wave amplitude is fixed at 0.0005.

by

$$\omega_r = \omega_n \sqrt{1 - 2\zeta^2} \tag{5.16}$$

$$M_r = \frac{1}{2\zeta\sqrt{1-\zeta^2}} \tag{5.17}$$

where ω_n and ζ are the natural frequency and damping ratio, respectively. The resonant peak M_r is the ratio of the maximum response to the excitation amplitude. In the simulations presented in Figs. 5.2 and 5.3, the excitation amplitude is 0.0005. Using the maximum response, we determined the heave and pitch resonant frequencies ω_{zr} and $\omega_{\theta r}$ from measuring the zero crossings of the forced response presented in Fig. 5.2. The results are $\omega_{zr} \approx 0.5066$ and $\omega_{\theta r} \approx 0.5981$. Using Eqs. (5.16) and (5.17), we found that the heave and pitch linear natural frequencies and damping ratios are $\omega_z \approx 0.5873$, $\omega_\theta \approx 0.6397$, $\zeta_z \approx 0.3577$, and $\zeta_\theta \approx 0.2506$. Using these values, we found that the heave and pitch linear damping coefficients are $\mu_z \approx 0.2101$ and $\mu_\theta \approx 0.1603$. A summary of these parameters is presented in Table 5.1.

Table 5.1: Identified linear parameters for the ship simulation. All of the parameters are presented in nondimensional units.

ω_{zr}	0.5066
$\omega_{\theta r}$	0.5981
$\omega_{\phi d}$	0.2742
ζ_z	0.3577
ζ_θ	0.2506
ζ_ϕ	0.0420
ω_z	0.5873
ω_θ	0.6397
ω_ϕ	0.2744
μ_z	0.2101
μ_θ	0.1603
μ_ϕ	0.0110

5.4 Identification of Nonlinear Parameters

In the parametric excitation considered here, the wave-encounter frequency is approximately equal to twice the roll natural frequency; yet the pitch and heave natural frequencies are not near twice the roll natural frequency. In order to study the model given by Eqs. (5.4)–(5.6), we conducted a series of simulations where the wave frequency is set at 0.5493. Figure 5.4 shows time histories corresponding to three wave excitations and their corresponding steady-state pitch and roll responses. The simulations were computed over 20,000 time steps; only

a small portion is shown in Fig. 5.4 for clarity. The wave excitation amplitude was varied between 0.25% and 0.35% of the ship length. The peak-to-peak steady-state nondimensional heave amplitude is approximately 0.007. The peak-to-peak steady-state pitch amplitude is approximately 1.3 degrees. The peak-to-peak steady-state roll amplitude is approximately 26 degrees. Note the relative difference between the large roll response and small pitch and heave responses.

Identification of the linear parameters for the system described in Section 5.3 allows for the identification of the nonlinear parameters c_z and c_θ as described in Eqs. (5.11) and (5.12). In considering the steady-state response, we set the amplitude and phase variations given by $\dot{a}_\phi$, $\dot{\gamma}_z$, and $\dot{\gamma}_\theta$ in Eqs. (5.8)–(5.9) equal to zero and obtain

$$0 = -\mu_\phi - \frac{|c_z|}{2\omega_\phi}\sin\gamma_z - \frac{|c_\theta|}{2\omega_\phi}\sin\gamma_\theta \tag{5.18}$$

$$0 = \sigma - \frac{|c_z|}{\omega_\phi}\cos\gamma_z - \frac{|c_\theta|}{\omega_\phi}\cos\gamma_\theta \tag{5.19}$$

For steady-state oscillations, all of the terms in Eqs. (5.18) and (5.19) are constant. Given for c_z and c_θ, these equations constitute a system of two equations with two unknowns $|c_z|$ and $|c_\theta|$. Solving them for the unknowns yields

$$|c_z| = \frac{2\sigma\omega_\phi}{\cos\gamma_z - \sin\gamma_z} \tag{5.20}$$

$$|c_\theta| = \frac{2\sigma\sin\gamma_z\omega_\phi}{-\cos\gamma_z\sin\gamma_\theta + \sin\gamma_z\sin\gamma_\theta} \tag{5.21}$$

The parameters ω_ϕ, μ_ϕ, and σ were determined in Section 5.3. The nonlinear phase quantities γ_z and γ_θ, as defined in Eqs. (5.13)–(5.14), are phase quantities which can be quantified using the cross-bispectra between the heave or pitch response and the roll response. These phase

Table 5.2: Nonlinear phase quantities computed from simulations of the ship roll instability. These quantities are computed according to Eqs.(5.22)–(5.23).

Wave Amplitude	γ_z (deg)	γ_θ (deg)
0.0025	34.8	294.3
0.0030	31.5	290.9
0.0035	29.3	288.4

Table 5.3: Nonlinear parameters identified for the ship roll instability. These quantities are computed according to Eqs.(5.20) and (5.21).

$\|c_z\|$	0.0476
$\|c_\theta\|$	0.0726

quantities are given by

$$\gamma_z = \angle B_{z\phi\phi}(\frac{\Omega}{2}, \frac{\Omega}{2}) \tag{5.22}$$

$$\gamma_\theta = \angle B_{\theta\phi\phi}(\frac{\Omega}{2}, \frac{\Omega}{2}) \tag{5.23}$$

Representative cross-bicoherence, computed from the three sets of LAMP simulations for the parametric response, are shown in Figs. 5.5 and 5.6, and the phase quantities γ_z and γ_θ are given in Table 5.2. The large levels of cross-bicoherence shown in Figs. 5.5 and 5.6 indicate high confidence in the values of γ_z and γ_θ.

Having computed these nonlinear phase quantities, we obtained the nonlinear parameters $|c_z|$ and $|c_\theta|$ using Eqs. (5.20) and (5.21) and their values are listed in Table 5.3.

5.5 Validation

To validate the parameters given in Table 5.3, we integrated Eq. (5.6) numerically to detemine the response to excitation levels comparable to those used in the LAMP simulation. Because the nonlinear parameters $|c_z|$ and $|c_\theta|$ represent combinations of nonlinear parameters, as described in Eqs. (5.11) and (5.12), the integrations are performed assuming zero values for either $K_{\phi z}$ or $K_{\dot{\phi}\dot{z}}$ and either $K_{\phi\theta}$ or $K_{\dot{\phi}\dot{\theta}}$. The integration time step was set at 0.08 s. The numerical simulations were found to be highly sensitive to the wave-encounter frequency. The roll response vanished with just a 0.015 Hz change in the wave-encounter frequency. It is noted that this change falls below the frequency resolution used in the frequency-domain analysis. The wave-encounter frequency was then adjusted by approximately 0.015 Hz to produce a nontrivial roll response for two of the three excitation levels. A nontrivial roll response could not be duplicated for the wave amplitude of 0.0025. As a qualitative measure of the agreement between the mathematical model and the simulations, in Fig. 5.7 we compare the response time histories predicted by the model to the simulations. This comparison shows a high accuracy of the identified parameters.

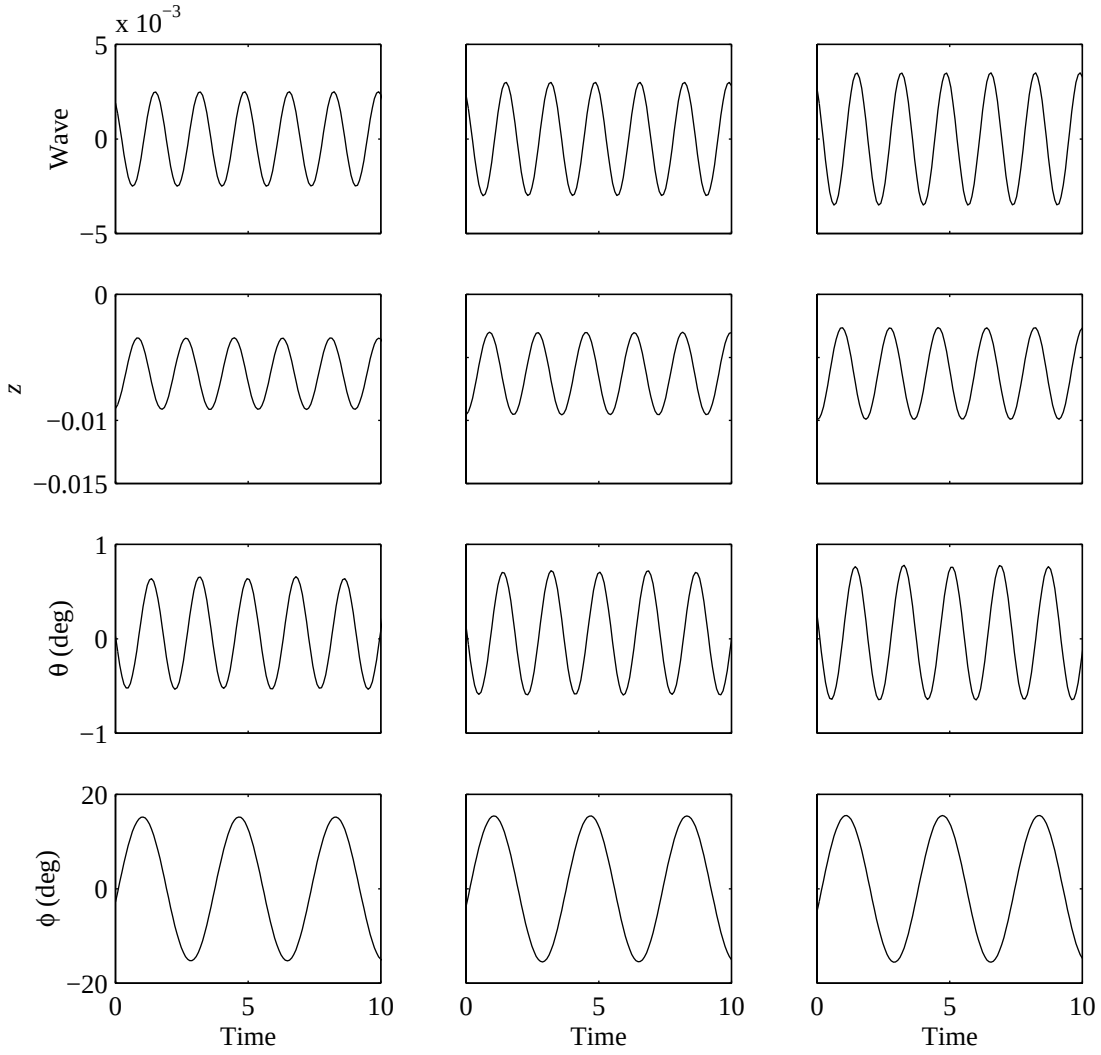

Figure 5.4: Numerical simulation time histories of the steady-state excitation wave, pitch response, and roll response at wave amplitudes of a) 0.25%, b) 0.30%, and c) 0.35% of the ship length. Time is measured in nondimensional units.

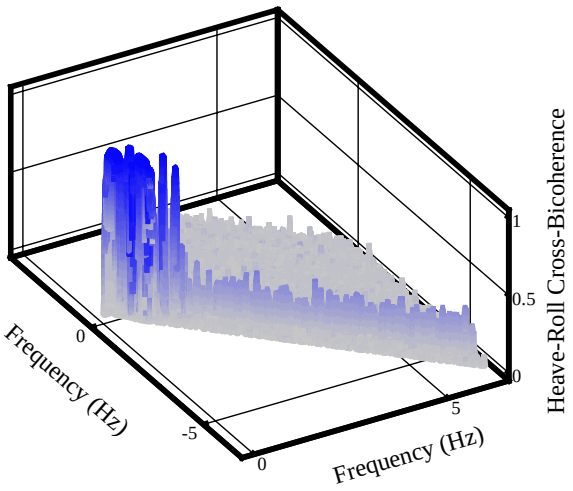

Figure 5.5: A representative heave-roll cross-bicoherence for the ship roll instability.

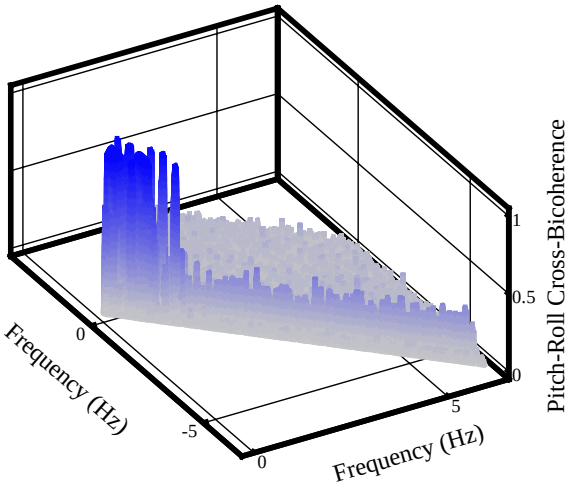

Figure 5.6: A representative pitch-roll cross-bicoherence for the ship roll instability.

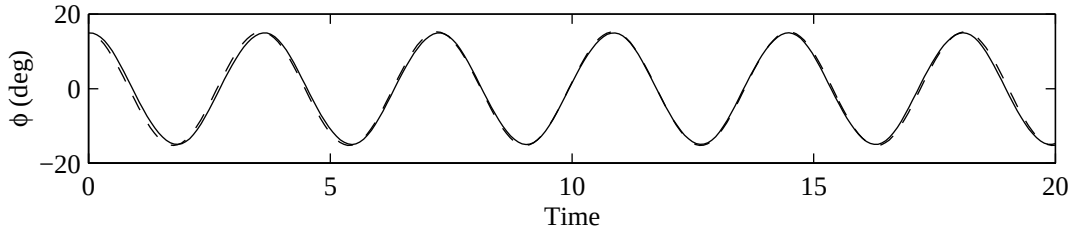

Figure 5.7: A comparison of steady-state time-histories: simulation (solid) and analysis (dashed). Here, the wave amplitude is 0.0035.

Chapter 6

Conclusions

A parametric identification procedure that is based on the method of multiple scales and amplitude and phase measurements from higher-order spectral moments for nonlinear systems is outlined. This procedure allows for the characterization as well as the identification of the relevant parameters governing the response of a nonlinear system in an accurate and efficient manner. This procedure can be used to provide a modeling scheme compatible with prediction, simulation, and control. To validate the procedure, we carried out numerical simulations for two nonlinear systems. In each case, identification of the relevant parameters governing the response was performed. Using the identified parameters, we computed time histories and compared them to the original time histories. These comparisons show the accuracy of the procedure in modeling the systems.

For the purposes of prediction and control, modeling was performed for two structural systems: a cantilevered beam and a three-beam frame. Experiments whereby resonance conditions were present were conducted. Nonlinear system identification was performed on

the experimental data. Using the identified parameters for each systemi, we were able to successfully model the response of each system.

To consider other applications of the identification procedure, we considered a multiple-degree-of-freedom system. Modeling was performed for a numerically simulated roll instability via a parametric mechanism where the ship heave, pitch, and roll motions are coupled. Numerical simulations were conducted using LAMP. Again, the identification procedure produced parameters which successfully modeled the response.

The results from the numerical validation, the experiments for the structural systems, and the LAMP simulations of the ship response show that, with the procedure presented here, one can

- characterize the damping;
- characterize the relative effect of parametric and direct excitations;
- quantify all of the relevant parameters;
- model multiple-degree-of-freedom systems.

The results from this work show that the procedure can be readily applied for nonlinear system parameter identification. Future work with this procedure would involve investigations of other single- and multiple-degree-of-freedom systems. These investigations would use other types of resonances and a combination of the method of multiple scales and higher-order statistics while preserving the methodology of the procedure outlined in this work.

References

[1] F. Benedettini, D. Capecchi, and F. Vestroni. "Identification of hysteretic oscillators under earthquake loading by nonparametric models." *Journal of Engineering Mechanics*, Vol. 121, pp. 606–612, 1995.

[2] B. S. Berger, I. Minis, K. Deng, Y. S. Chen, A. Chavali, and M. Rokni. "Phase coupling in orthogonal cutting." *Journal of Sound and Vibration*, Vol. 191, pp. 976–985, 1996.

[3] D. R. Brillinger. "An introduction to polyspectra." *Ann. Math. Statist.*, Vol. 36, pp. 1351–1374, 1965.

[4] D. R. Brillinger. "Some basic aspects and uses of higher-order spectra." *Signal Processing*, Vol. 36, pp. 239–249, 1994.

[5] P. M. T. Broersen. "Estimation of parameters of non-linear dynamical systems." *International Journal of Non-Linear Mechanics*, Vol. 9, pp. 355–361, 1974.

[6] Y. S. Cho and E. J. Powers. "Quadratic system identification using higher order spectra of i.i.d. systems." *IEEE Transactions on Signal Processing*, Vol. 42, pp. 1268–1271, 1994.

[7] W. B. Collis. *Higher Order Spectra and Their Application to Nonlinear Mechanical Systems.* PhD thesis, University of Southampton, 1996.

[8] N. Distefano and A. Rath. "System identification in nonlinear structural seismic dynamics." *Computer Methods in Applied Mechanics and Engineering*, Vol. 5, pp. 353–372, 1975.

[9] S. O. Fahey and A. H. Nayfeh. "Experimental nonlinear identification of a single structural mode." Proceedings of the 16th IMAC, Santa Barbara, CA, Feb. 2–5 1998.

[10] L. Fiedler. "An experimental and theoretical investigation into the influence of hysteretic damping on the dynamic behavior of a three-beam structure." Master thesis, Virginia Polytechnic Institute and State University, 1996.

[11] G. B. Giannakis and J. M. Mendel. "Identification of nonminimum phase systems using higher order statistics." *IEEE Transactions on Acoustics, Speech, and Signal Processing*, Vol. 37, pp. 360–376, 1989.

[12] M. R. Hajj, R. W. Miksad, and E. J. Powers. "Subharmonic growth by parametric resonance." *Journal of Fluid Mechanics*, Vol. 236, pp. 385–413, 1992.

[13] M. R. Hajj, R. W. Miksad, and E. J. Powers. "Fundamental-subharmonic interaction: Effect of phase relation." *Journal of Fluid Mechanics*, Vol. 256, pp. 403–426, 1993.

[14] M. R. Hajj, R. W. Miksad, and E. J. Powers. "Perspective: Measurements and analyses of nonlinear wave interactions with higher-order spectral moments." *Journal of Fluids Engineering*, Vol. 119, pp. 3–13, 1997.

[15] M. R. Hajj, R. W. Miksad, R. S. Solis, and E. J. Powers. "An experimental investigation of the characteristics of an unsteady wake." *International Journal of Offshore and Polar Engineering*, Vol. 4, pp. 1–5, 1994.

[16] M. R. Hajj, A. H. Nayfeh, and P. Popovic. "Identification of nonlinear systems parameters using polyspectral measurements and analysis." ASME 15th Biennial Conference on Mechanical Vibration and Noise, Boston, MA, Sept. 17–21, 1995.

[17] R. Henry, C. Favé, S. Soreefan, and A. Robins. "Etudes d'interactions acoustiques nonlinéaires dans les jets confinés, par la fonction de bicohérence." *Journal de Physique*, Vol. 4, pp. C5 959–962, 1994.

[18] M. Jin. *Spectral and Bispectral Analysis on Nonlinear Phreatic Aquifer Systems: Theory and Applications*. PhD thesis, Pennsylvania State University, 1993.

[19] L. A. Jurman. *Interfacial Waves on Sheared, Thin Liquid Films*. PhD thesis, University of Notre Dame, 1990.

[20] Y. C. Kim and E. J. Powers. "Digital bispectral analysis and its applications to nonlinear wave interactions." *IEEE Trans. Plasma Sci.*, Vol. PS-7, pp. 120–131, 1979.

[21] S. F. Masri. "A hybrid parametric/nonparametric approach for the identification of nonlinear systems." *Probabilistic Engineering Mechanics*, Vol. 9, pp. 47–57, 1994.

[22] S. F. Masri and T. K. Caughey. "A nonparametric identification technique for nonlinear dynamic problems." *Journal of Applied Mechanics*, Vol. 46, pp. 433–447, 1979.

[23] R. W. Miksad, F. L. Jones, E. J. Powers, Y. C. Kim, and L. Khadra. "Experiments on the role of amplitude and phase modulations during transition to turbulence." *Journal of Fluid Mechanics*, Vol. 123, pp. 1–29, 1982.

[24] W. H. Miles and C. Pezeshki. "Bispectral analysis of a fluid elastic system: The cantilevered pipe." *Journal of Fluids and Structures*, Vol. 6, pp. 633–640, 1992.

[25] D. T. Mook, L. R. Marshall, and A. H. Nayfeh. "Subharmonic and superharmonic resonances in the pitch and roll modes of ship motions." *Journal of Hydronautics*, Vol. 8, pp. 32–40, 1974.

[26] A. H. Nayfeh. *Introduction to Perturbation Techniques.* Wiley-Interscience, New York, 1981.

[27] A. H. Nayfeh. "Parametric identification of nonlinear systems." *Computers and Structures*, Vol. 20, pp. 487–493, 1985.

[28] A. H. Nayfeh. "On the undesirable roll characteristics of ships in regular seas." *Journal of Ship Research*, Vol. 32, pp. 92–100, 1988.

[29] A. H. Nayfeh and D. T. Mook. *Nonlinear Oscillations.* Wiley-Interscience, New York, 1979.

[30] A. H. Nayfeh, D. T. Mook, and L. R. Marshall. "Nonlinear coupling of pitch and roll modes in ship motion." *Journal of Hydronautics*, Vol. 7, pp. 145–152, 1973.

[31] T. Ning and J. D. Bronzino. "Autoregressive and bispectral analysis techniques: EEG applications." *IEEE Engineering in Medicine and Biology Magazine*, Vol. 9, pp. 47–50, 1990.

[32] T. Ning and J. D. Bronzino. "Cross-bispectra of the rat EEG during REM sleep." in Annual International Conference of the IEEE Engineering Medicine and Biology Society, Vol. 13, pp. 447–448, 1991.

[33] I. G. Oh, A. H. Nayfeh, and D. T. Mook. "Theoretical and experimental study of the nonlinearly coupled heave, pitch, and roll motions of a ship in longitudinal waves." *Nonlinear Vibrations*, Vol. 54, pp. 105–125, 1993.

[34] S. S. Oueini and A. H. Nayfeh. "Single-mode control of a cantilever beam under principal parametric excitation." in preparation, 1998.

[35] C. Pezeshki, S. Elgar, and R. Krishna. "Bispectral analysis of possessing chaotic motion." *Journal of Sound and Vibration*, Vol. 137, pp. 357–368, 1990.

[36] C. Pezeshki, S. Elgar, R. Krishna, and T. D. Burton. "Auto and cross-bispectral analysis of a system of two coupled oscillators with quadratic nonlinearities possessing chaotic motion." *Journal of Applied Mechanics*, Vol. 59, pp. 657–663, 1992.

[37] P. Popovic, A. H. Nayfeh, K. Oh, and S. A. Nayfeh. "An experimental investigation of energy transfer from a high-frequency mode to a low-frequency mode in a flexible structure." *Journal of Vibration and Control*, Vol. 1, pp. 115–128, 1995.

[38] C. P. Ritz, E. J. Powers, R. W. Miksad, and R. S. Solis. "Nonlinear spectral dynamics of a transitioning flow." *Physics of Fluids*, Vol. 31, pp. 3577–3588, 1988.

[39] D. F. Scharpf. *An Experimental Investigation of the Sources of Propeller Noise Due to Turbulence Ingestion.* PhD thesis, University of Notre Dame, 1993.

[40] Scientific Applications International Corporation. *Large Amplitude Motions Program (LAMP)*, 1997.

[41] J. L. Shils. *The Bispectrum of the Human Electroencephalogram.* PhD thesis, University of Pennsylvania, 1995.

[42] R. O. Stearman, E. J. Powers, J. Schwartz, and R. Yurkovich. "Aeroelastic system identification of advanced technology aircraft through higher-order signal processing." *Proceedings of the 9th IMAC*, pp. 1607–1616, 1991.

[43] F. E. Udwadia and C.-P. Kuo. "Non-parametric identification of a class of non-linear close-coupled dynamic systems." *Earthquake Engineering and Structural Dynamics*, Vol. 9, pp. 385–409, 1981.

[44] R. G. Williams. *The Internal Tide off Southern California.* PhD thesis, University of California, San Diego, 1985.

Vita

Jimmy Fung was born in New York City, New York, on November 21, 1974. He was raised in Richmond, Virginia, where he attended the Douglas Southall Freeman High School. After completing his high-school studies, he enrolled at Virginia Tech in the fall of 1992 to pursue a Bachelor's Degree in Aerospace Engineering with a minor in Mathematics. He participated in a cooperative education program at NASA Langley Research Center prior to earning his Bachelor's Degree in June 1997. He enrolled in a dual Bachelor/Master program in December 1996 to pursue a Master's Degree in Engineering Mechanics.